Dissertation

User Cooperation in Wireless Time-Variant Channels

ausgeführt zum Zwecke der Erlangung des akademischen Grades eines Doktors der technischen Wissenschaften

eingereicht an der
Technischen Universität Wien
Fakultät für Elektrotechnik und Informationstechnik

von
Zhinan Xu

Wien, 14. October 2016

Supervisor
Priv.-Doz. Dr.techn. Thomas Zemen
Digital Safety and Security Department
AIT Austrian Institute of Technology, Vienna, Austria

Examiner
Prof. Marius Pesavento
Department of Electrical Engineering and Information Technology
Technische Universität Darmstadt, Germany

and

Prof. Christoph Mecklenbräuker
Institute of Telecommunications
Technische Universität Wien, Austria

Abstract

For wireless communications, the spectrum limitation and user mobility are two major challenges to promise reliable communications with high data rates and low latency. In order to improve spectral efficiency, future mobile systems employ full reuse of wireless spectrum, which makes interference management become a fundamental prerequisite to cope with the growing inter-cell interference. Future mobile standards, e.g. 5G, will support critical applications that require ultra reliability and low latency. Examples include traffic safety applications and autonomous driving. In this thesis, we propose and analyze interference management techniques for interference channels. We devise non-stationary vehicular channel modeling approaches and evaluate the cooperative communication performance.

In the first part of the thesis, interference alignment (IA) in K-user interference channels is studied. Different interference management schemes for K-user interference channels are introduced and compared. Since global channel state information (CSI) plays a central role to achieve IA as well as the optimal degrees of freedom (DoF), we propose a joint channel estimation, feedback and prediction framework for IA in time-variant channels. The proposed algorithm allows reduced-rank channel prediction. An upper bound for the rate loss caused by feedback quantization and channel prediction is derived. We develop a subspace dimension switching algorithm, which is able to find the subspace dimension associated with a higher rate. The scaling of the required number of bits is characterized in order to decouple the rate loss due to quantization from the transmit power.

To relief the global CSI burden, we study opportunistic interference alignment (OIA) algorithms, which exploit channel randomness and multiuser diversity by user selection. We tackle the problem of feedback reduction for OIA using threshold-based feedback schemes. We investigate different threshold choices, user scaling laws and the achievability of DoF for real-valued feedback and 1-bit feedback, respectively. For OIA with real-valued feedback, the threshold and the corresponding feedback load to achieve the optimal DoF are analyzed. For OIA with 1-bit feedback, we find an optimal choice of the 1-bit quantizer to achieve the DoF $d = 1$. For DoF with $d > 1$, an asymptotic threshold choice is provided by solving an upper bound for the rate loss.

In the second part of the thesis, we focus on channel modeling and performance analysis for vehicular communications. A geometry-based stochastic channel model (GSCM) for road intersections is developed. We use the proposed model to evaluate the communication performance in terms of frame error rate. The evaluation is performed at various transmitter/receiver locations and velocities with three different types of channel estimators. In order to overcome the low signal-to-noise ratio due to non-line-of-sight, we deploy a relay node at the intersection, which increases the transmission reliability significantly.

In order to reduce the complexity of the GSCM, a cluster-based vehicular channel model is proposed. The cluster-based model achieves a low computational complexity suitable for a real-time implementation. We apply a joint cluster identification-and-tracking algorithm to the measurement data in delay-Doppler plane. We divide the cluster locations in the delay-Doppler plane into different characteristic regions and characterize the time-variant cluster parameters in each region. For a low-complexity implementation, we draw the cluster parameters randomly using pre-computed distributions. The proposed model is validated with measurement data.

Acknowledgement

First of all, I would like to express my deep gratitude to my supervisor Thomas Zemen for offering me the opportunity to pursue my Ph.D study, and for sharing his profound scientific and technical knowledge. His supervision during five years of my Ph.D shaped my knowledge and skills.

I want to thank Professor Christoph Mecklenbruker and Professor Marius Pesavento for their interest in my work and for finding time from their busy schedules to be my examiners.

I would like to thank all my colleagues at FTW and AIT for creating an inspiring, conducive, and friendly atmosphere for research, especially to my former colleagues from Area-I. Particular thanks go to Mingming Gan, Sanda Drakulic and Markus Hofer for numerous fruitful on-and off-topic discussions, and for encouraging me to fight till the end.

My time in Vienna would not have been the same without my lovely friends here. In particular, I thank Hua, Boyu, Qi, Panda, Yutong, Xu and Lilian. I am grateful for their friendship and cherish the time we spent together here.

Finally, I would like to express my deepest appreciation to my parents for their love and support.

Contents

List of Figures

List of Tables

1 Introduction

In the past decades, wireless networks are experiencing a dramatic increase of mobile traffic [2]. Driven by the lifestyle change where people are more conncted and tend to have alway-accessible broadband connections, an increase of 12 times in total mobile traffic is expected between 2015 and 2021. The predicted mobile traffic growth is shown in Fig. 1.1 [1]. Therefore, innovative enabling technologies are needed in the next generation standards, in order to fulfill the growing requirement on the system performance.

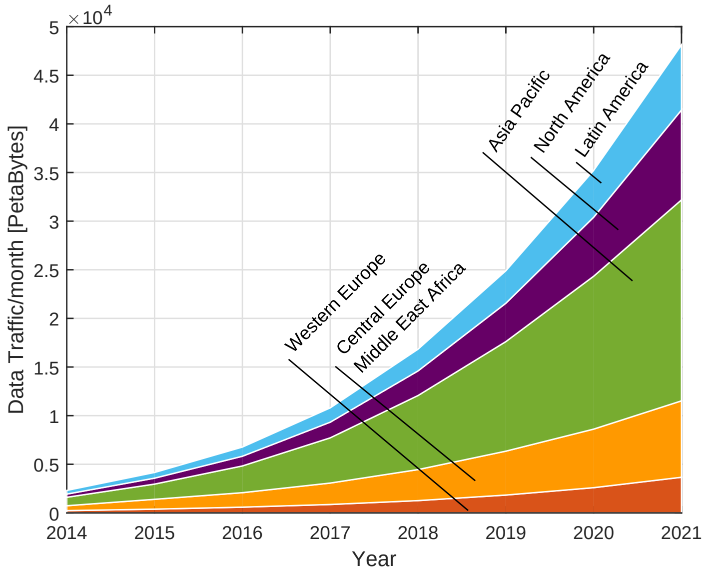

Figure 1.1: Wireless data traffic growth (Source: Ericsson traffic exploration tool, June 2016 [1])

The next generation standard for mobile communications, e.g. 5G, will provide enhancements in mobile broadband services, as well as enabling a broader spectrum of use cases for the internet of things (IoT). As shown in [2], mobile phones are currently the largest category of connected devices, but in 2018 they are expected to be overtaken by the IoT, including connected vehicles, machines, remote sensors and consumer electronics. The estimated number of connected devices of different category for 2015 and 2021 is shown in Fig. 1.2. Driven by new use cases, the number of IoT devices are expected to grow at a compounded annual growth rate of 23% from 2015 to 2021 according to Ericsson [2].

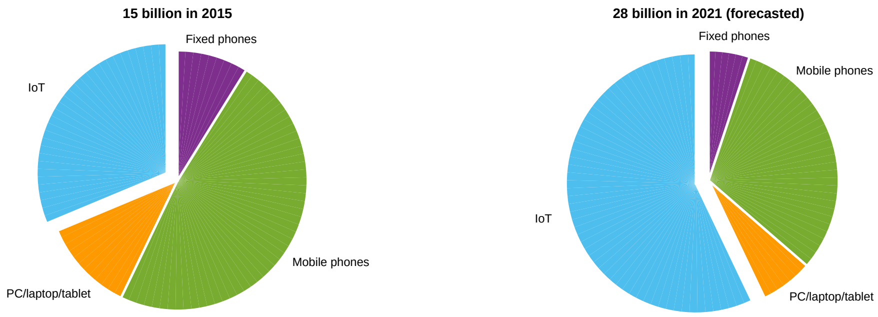

Figure 1.2: Growth in the number of connected devices (Source: Ericsson Mobility Report, June 2016 [2])

For IoT, a very important market targeting on critical applications requires ultra-reliable communications with very low latency. Examples are traffic safety, autonomous cars, industrial applications, health-care etc. Therefore, new technologies in 5G have to be developed in order to extend the range of possible applications for critical IoT deployments. In this thesis, we focus on enabling technologies improving network capacity and reliability of communications.

1.1 Scope of the Work

For wireless communications, electromagnetic waves propagate between transmitter and receiver. The inherent nature of wireless propagation poses challenges for the wireless system design. Two of the most important ones are the spectrum limitations and user mobility.

Due to the scarce spectrum resource and the performance limits of conventional orthogonal resource sharing, the densification of the network is considered as a key to improve spectral efficiency and user throughput. The standards for future generation cellular networks are based on overlaid heterogeneous network deployment with full frequency reuse of the spectral resource [4]. However, as the density and traffic load of the network increases, concurrent transmissions occurring simultaneously in the same frequency band lead to severe inter-cell interference. Thus, the receiver gets a superposition of the intended signal and many interference signals, resulting in error propagation if transmission is limited by interference. As a consequence, more sophisticated capabilities for efficient interference management algorithms are indispensable [4]. These interference management algorithms allow the transmitter to adapt transmission to the propagation conditions and to separate the signals of different users via beamforming. This also means that the transmitter requires some form of knowledge of the wireless channel conditions, known as channel state information (CSI). For frequency-division duplex (FDD) systems where the uplink and downlink channels are highly uncorrelated because of the use of different frequencies, the CSI has to be transfered via a low rate feedback channel.

We focus on distributed systems where the capability of joint signal processing is not available at the transmitter side. This implies that the user data is not shared among transmitters, saving the amount of data transfered via backhaul. We address the problem of CSI feedback for FDD systems. In an interference channel scenario, we study interference alignment (IA) which promises optimal sum rate capacity scaling with the number of users in the network in the high signal-to-noise ratio (SNR) regime. We tackle the problem of CSI acquisition and feedback for IA in time-variant channels. In interference broadcast channels, low-rate feedback about channel quality at different users allow for opportunistic selection of the best user leveraging multi-user diversity. We study a threshold-based approach to reduce the amount of feedback information and prove that 1-bit feedback per user is enough to achieve the optimal capacity scaling.

The cooperation decisions (e.g., interference alignment or user selection decisions) have to be made frequently due to the time variability of the channel and user mobility. Therefore, an understanding of the radio propagation channel is required to build up efficient cooperative algorithms. In general, computer simulation allows repeatable performance test instead of expensive field test. However, the simulation result is only trustworthy if all the components, including the channel model reflect the reality of the deployment. Therefore, we need a channel model that resembles the true propagation conditions.

In the second part of the thesis, we study vehicular channel modeling approaches reflecting the realities of the propagation environment. A very important characteristic of vehicular channels is that the statistical properties of the channel change over time and therefore the channel is non-stationary. For this reason, we use non-stationary geometry-based and cluster-based models for different safety critical scenarios. We evaluate the communication performance in terms of frame error rate (FER) for vehicular communications and demonstrate the enhancement by using relaying techniques.

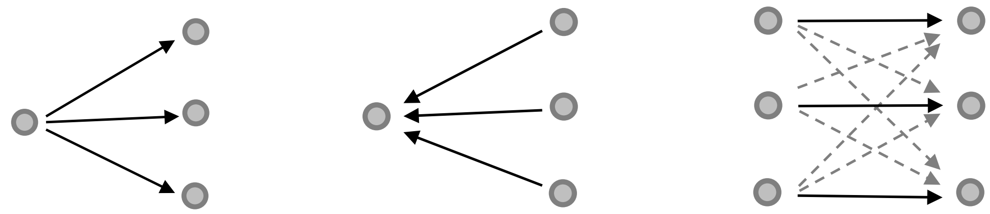

(a) Broadcast channel with K receivers. (b) Multiple access channel with K transmitters. (c) K-user interference channel.

Figure 1.3: Multiuser network setups.

1.2 State of the Art

In this section, we review the state of the art that is related to the scope of the thesis. In Section 1.2.1, we introduce multiuser channels and the corresponding results on capacity characterization. In Section 1.2.2, we discuss related work on the multiuser interference channels. The state of the art is briefly outlined, with an emphasis on IA technique. In Section 1.2.3, we look at vehicular radio channel characterization, non-stationarity and different channel modeling approaches.

1.2.1 Multiuser Channel

Wireless communication systems often have multiple transmitters and receivers sharing the same transmission medium. This leads to mutual interference. Therefore, the characterization of the capacity of multiuser systems is more difficult than single-user systems, where multiuser systems are considered interference-limited since the spectral efficiency of the system is restricted by interference signals. Referring to information-theoretical terminologies, multiuser channels are categorized into different models, e.g. broadcast channels, multiple access channels and interference channels, as shown in Fig. 1.3. In broadcast channels, one transmitter sends multiple independent streams to multiple receivers [5]. Therefore, the transmission from the transmitter to each receiver is considered as interference to all the other receivers. In multiple access channels, the situation is reversed, where multiple independent transmitters send multiple independent streams simultaneously to a common receiver [6]. Accordingly, the transmission from each transmitter to the common receiver interferes with the transmissions of other transmitters. In interference channels, each transmitter sends an independent stream to its intended receiver causing interference to other receivers [7–9].

There are some multi-user systems whose capacity regions are known. The multiple-input multiple-output (MIMO) multiple access channel is one of few multi-user systems for which the capacity is known when channel state information at the transmitter (CSIT) is available. The capacity region of MIMO multiple access channel is presented in [6] for joint decoding and independent decoding. As the dual channel of MIMO multiple access channel, the capacity region of MIMO broadcast channel is found [5] via dirty-paper coding [10].

Interference channel is also one of the fundamental channels studied in information theory. However, capacity characterization of interference channels has remained an open question for decades [7]. Information theorists put a lot of effort to pursue achievable rate regions, capacity inner-and outer-bounds of interference channels. For the two-user interference channel, the results are outlined in [7–9] and the references therein.

1.2.2 Interference Alignment

The exact capacity characterization of interference channels has been proven to be very challenging. An alternative metric named degrees of freedom (DoF) has been widely used as a tool to understand the fundamental limits of these networks with unknown capacity region [11]. DoF, also known as capacity pre-log factor, can be understood as the number of interference-free dimensions that can be employed in a network and reflects capacity scaling at high SNRs. Cadambe and Jafar proved in their landmark paper [11] that IA can provide each user in a K-user SISO interference channel with one half of the DoF, regardless of the number of users. Therefore, the total DoF of the network grows linearly with the number of users and becomes $K/2$. On the other hand, K independent point-to-point interference-free channels incur a total DoF of K at high SNRs. This implies that IA allows virtually interference-free communications by sacrificing half of the DoFs with respect to what can be achieved over isolated point-to-point links. Thus, the loss in number of DoF of each user, due to the distributed nature of the interference channel that prohibits joint signal processing at transmitter and receiver side, is independent of K and much smaller than previously believed [12].

For the sake of complexity reduction, opportunistic interference alignment (OIA) has been studied lately [13–18]. The key idea of OIA is to exploit the channel randomness and multiuser diversity by proper user selection. In [13–18], signal subspace dimensions are used to align the interference signals. Each transmitter opportunistically selects and serves the user whose interference channels are most aligned to each other. The degree of alignment is quantified by a metric. To facilitate a user selection algorithm, all potential users associated with the transmitter are required to calculate and feedback the metric value based on the local CSI. Perfect IA can be achieved asymptotically if the number of users scales fast enough with SNR. The corresponding user scaling law to obtain the optimal DoF is characterized for multiple access channels in [13,14] and for downlink interference channels in [16–18].

1.2.3 Channel Modeling for Cooperative Vehicular Communications

A channel model serves as the foundation for the design and test of different communication techniques. An accurate channel model, reflecting a realistic propagation environment, will deliver trustworthy results. In this section, we will introduce different channel modeling approaches and their suitability for vehicle-to-vehicle (V2V) channels.

A channel model is a mathematical description of the channel impulse responses. Parameters characterized from measurement campaigns are fed into channel models so that they create channel impulse responses for different environments. For vehicular communications, there are generally three modeling approaches in use [19]: i) ***Stored channel impulse responses*** are collected in measurement campaigns and used for system simulations. The advantage of this method is that the resulting impulse responses are realistic and repeatable (but with the same fading realization). However, it requires a large effort to perform the measurements and acquire the data. ii) ***Deterministic channel models*** calculate channel impulse responses by solving Maxwell equations (or some approximation thereof) for a specific site. The calculation is based on the physical propagation of electromagnetic waves containing the geometric and electromagnetic information in a specific site under consideration. It is important to precisely define the physical objects in the environment and their corresponding electromagnetic properties. The channel model produces accurate results at the expense of a large computational effort. iii) ***Stochastic channel models*** aim at modeling the probability density functions (PDFs) of the channel impulse responses. Opposed to the deterministic approach, the stochastic approach does not attempt to match the impulse response for each specific location, but rather to match the PDFs. In the following, we focus on reviewing stochastic channel models.

We can categorize stochastic channel models into two groups: narrowband models and wideband models. The narrowband stochastic approach models only the time-selectivity of the fading process by its Doppler spectrum. The wide-band stochastic approach models also the frequency-selectivity of the fading process. The most commonly used wideband stochastic channel model for vehicular communications is the tapped delay line model [20], where each tap is assumed to fade independently with given channel statistics, based on the wide sense stationary uncorrelated scattering (WSSUS) assumption [21]. Its low complexity makes it very attractive for high-level simulation systems such as the IEEE 802.11p standard [22]. However, the WSSUS assumption does not hold for vehicular channels due to the rapidly changing environment [23].

A very important line of work for vehicular channel modeling is the geometry-based stochastic channel model (GSCM), which combines the two aforementioned approaches. The basic idea of GSCMs is to place an ensemble of point scatterers according to a certain statistical distribution or at physically realistic positions. A simplified ray tracing is then performed to determine their respective signal contributions from different scatterers. The impulse response is the superposition of the contribution from different scatterers [16]. The GSCMs can provide an accurate representation of the properties of the V2V channels. The channel model generates CIRs for different environments by using the right parameter set, thus it is flexible. However, the computational complexity is relatively high due to the summation of a large number of complex exponentials. Noteworthy is that these channel models inherently include the non-stationarities of the fading process, since they include the objects movement.

The computational complexity of a GSCM is rather high for the purpose of a realtime implementation. The clustering of multipath components (MPCs) exhibiting similar properties can efficiently reduce the complexity [24, 25]. The relevant cluster parameters are characterized based on measurements. Most works on the characteristics of clusters are obtained for indoor channels where the MPCs are resolved in the angular and delay domains [25, 26]. For outdoor scenarios with user mobility, only a few publications exist. The work in [27] presents clustering results for an urban vehicle-to-infrastructure (V2I) scenario. Characterization of the number and extension of clusters is provided in [28] for a V2V scenario.

1.3 Outline and Contributions

The thesis is organized into the following parts and chapters:

Part I: Interference Alignment

Chapter 2: Introduction to Interference Alignment In this chapter, we introduce the basic idea of IA in K-user interference channels. We give the definition of

DoF for different channel configurations. We illustrate the fundamentals of IA with a focus on the achievable DoF and IA solutions through closed-form and iterative methods. We discuss the role of CSI and introduce CSI acquisition and feedback problem.

Chapter 3 : Interference Alignment in Time-variant Channels Imperfect CSI, due to channel estimation error, imperfect CSI feedback and time selectivity of the channel, lead to a performance loss. In this chapter, we devise a channel estimation, feedback and prediction framework for IA in time variant channels. The feedback algorithm enables reduced-rank channel prediction to compensate for the channel estimation error due to time selectivity of the fading process and feedback delay. An upper bound for the rate loss caused by feedback quantization and channel prediction is derived. Based on this bound, we develop a dimension switching algorithm for the reduced-rank predictor to find the best tradeoff between quantization- and prediction-error. Besides, we characterize the scaling of the required number of feedback bits in order to decouple the rate loss due to channel quantization from the transmit power.

Chapter 4: Opportunistic Interference Alignment This chapter introduces opportunistic interference alignment (OIA), which exploits channel randomness and multiuser diversity by user selection. For OIA the transmitter needs CSI, which is usually measured on the receiver side and sent to the transmitter side via a feedback channel. In this chapter, we investigate the problem of feedback reduction for OIA. This problem is addressed using threshold-based real-valued feedback and 1-bit feedback, respectively. The choices of threshold, user scaling law and the achievability of DoF are also analyzed. We compare OIA and IA with the same amount of feedback. We show that OIA has a much lower complexity and provides a better rate in the practical operation region of a cellular communication system.

Part II: Channel Modeling and Performance Analysis for Vehicular Communications

Chapter 5: Vehicular Channel Modeling using GSCM In this chapter, we aim to evaluate the communication performance between vehicles at road intersections. We implement a vehicular non-stationary GSCM for road intersections, which is an extension of an existing highway channel model. The model is verified by comparison with vehicular channel measurements. Using the proposed channel model, we present link level simulation results for IEEE 802.11p at varying transmitter/receiver locations using different channel estimation techniques. In order to overcome the low receive SNR due to non-line of sight (NLOS), we place a relay at road intersections to enhance the reliability of communication links.

Chapter 6: Vehicular Channel Modeling using a Cluster Based Approach In this chapter, we consider the cluster-based channel modeling approach for vehicular communications. We analyze the clustering of multi-path components in the delay-Doppler domain using the local scattering function of channel measurement data. The rapid change of the environment due to high velocities of the transmitter and receiver also results in fast changing cluster parameters. We present an automatic cluster identification and tracking algorithm in order to consistently characterize the evolution of cluster parameters. Based on vehicular channel measurements, the cluster lifetime, delay and Doppler spreads are characterized and presented.

In the second part of this chapter, we propose a cluster based vehicular channel model, which yields lower computational complexity compared to a GSCM. We divide the cluster locations in the delay-Doppler plane into different characteristic regions and characterize the time-variant cluster parameter in each region. For low complexity emulation the cluster parameters are randomly drawn from these pre-computed distributions. The proposed model is validated with measurement data using the cumulative distribution function of the root mean square delay spread and Doppler spread.

The content of this thesis is to a great extent also covered in the following publications:

[29] Z. Xu and T. Zemen, "Grassmannian delay-tolerant limited feedback for interference alignment," in *Asilomar Conference on Signals, Systems and Computers*, 2013, pp. 230-235.

[30] Z. Xu and T. Zemen, "Time-variant channel prediction for interference alignment with limited feedback," in *IEEE International Conference on Communications Workshops (ICC)*, 2014, pp. 653-658.

[31] Z. Xu, L. Bernadó, M. Gan, M. Hofer, T. Abbas, V. Shivaldova, K. Mahler, D. Smely, and T. Zemen, "Relaying for IEEE 802.11p at road intersection using a vehicular non-stationary channel model," in *IEEE 6th International Symposium on Wireless Vehicular Communications (WiVeC)*, 2014.

[32] Z. Xu, M. Gan, and T. Zemen, "Threshold-based selective feedback for opportunistic interference alignment," in *IEEE Wireless Communications and Networking Conference (WCNC)*, 2015, pp. 276-280.

[33] Z. Xu, M. Gan, and T. Zemen, "Opportunistic interference alignment with 1-bit feedback in 3-cell interference channels," in *IEEE 26th Annual International Symposium on Personal, Indoor, and Mobile Radio Communications (PIMRC)*, 2015, pp. 143-147.

[34] Z. Xu, M. Gan, C. F. Mecklenbräuker, and T. Zemen, "Cluster spreads for time-variant vehicular channels," in *9th European Conference on Antennas and Propagation (EuCAP)*, 2015.

[35] M. Gan, Z. Xu, C. F. Mecklenbruker, and T. Zemen, "Cluster lifetime characterization for vehicular communication channels," in *9th European Conference on Antennas and Propagation (EuCAP)*, 2015.

[36] Z. Xu, M. Gan, and T. Zemen, "Cluster-based non-stationary vehicular channel model," in *European Conference on Antennas and Propagation (EuCAP)*, 2016.

Part I

Interference Alignment

2 Introduction to Interference Alignment

This chapter introduces the background and the basics of interference alignment (IA) in K-user interference channels. First, we give an overview of different interference management schemes for K-user interference channels. Additionally, the definition of degrees of freedom (DoF) is introduced for different channel configurations. Afterwards, the basic concept of IA is illustrated with a focus on the achievable DoF and IA solutions through closed-form and iterative methods. Finally, limited feedback for single-input single-output (SISO) and multiple-input multiple-output (MIMO) IA is presented.

2.1 Interference Management in K-user Interference Channels

Interference generated by unintended transmitters is an inevitable nature for wireless communications. In multi-user systems, interference limits the reusability of spectral resources in space, which reduces the spectral efficiency of a communication system. As a result, interference management capabilities have to be embedded to achieve high data rates.

Traditional scheduling approaches such as orthogonal multiple access in time, frequency or by code are known to be robust against interference, while proven to be sub-optimal in terms of spectral efficiency. Since each user has access to only a fraction of the total available resources, and therefore the sum rate does not scale with the number of users K.

The processing power of wireless devices has increased rapidly in recent years which facilitates the implementation of complex interference management algorithms. The use of multi-carrier systems, e.g. orthogonal frequency division multiplexing (OFDM) system, has resulted in reliable and efficient transmissions in multi path environments. Also the capability of having multiple antennas at the devices has opened a new possibility to multi-user MIMO transmission techniques.

Taking advantage of the technological advancement brought by these approaches, a new technique named interference alignment (IA) has emerged, which promises higher spectral efficiency in interference channels. In Section 2.1.1, we introduce the concept of DoF, which is used as a metric to quantify the capacity scaling in interference channels. Then we compare the achievable DoF in different communication systems and show the advances of the IA technique.

2.1.1 Definition of DoF

The exact characterization of the capacity is not available in many multi-user channels, including the K-user interference channel for $K \geq 3$. Alternatively, the metric named DoF, as an approximation of capacity characterizations at high signal-to-noise ratio (SNR), is used. It is defined as

$$d = \lim_{\mathrm{SNR}\to\infty} \frac{C(\mathrm{SNR})}{\log_2(\mathrm{SNR})} \tag{2.1}$$

with C denoting the capacity. It has been shown in many cases that the number of DoF is tractable and becomes exact as the SNR goes to infinity. For many channels with unknown capacity regions, DoF regions are characterized instead. It serves as the first order approximation of the capacity, which captures the slope of the capacity with the logarithm of the SNR. The DoF are also known as the multiplexing gain or capacity pre-log factor.

Point-to-Point Communication System

Considering a point-to-point communication system with a single antenna, the input/output relationship reads $y = hx + n$, where h is the channel and $n \sim \mathcal{CN}(0, \sigma^2)$ denotes additive white Gaussian noise (AWGN). The SNR is defined as $\mathrm{SNR} = \frac{\mathbb{E}|x|^2}{\sigma^2}$ with $\mathbb{E}|x|^2$ denoting the transmit power. The capacity of this channel is $C(\mathrm{SNR}) = \log_2(1 + \mathrm{SNR}|h|^2)$. The DoF become

$$d = \lim_{\mathrm{SNR}\to\infty} \frac{\log_2(1 + \mathrm{SNR}|h|^2)}{\log_2(\mathrm{SNR})} = \lim_{\mathrm{SNR}\to\infty} \frac{\log_2(\mathrm{SNR}) + \log_2(|h|^2)}{\log_2(\mathrm{SNR})} = 1. \tag{2.2}$$

where the high SNR approximation $\log_2(1 + x) = \log_2(x)$ is used for $x > 0$. The approximation of the channel capacity at high SNR can be written as

$$C(\mathrm{SNR}) = \log_2(\mathrm{SNR}) + o\left(\log_2\left(\mathrm{SNR}\right)\right). \tag{2.3}$$

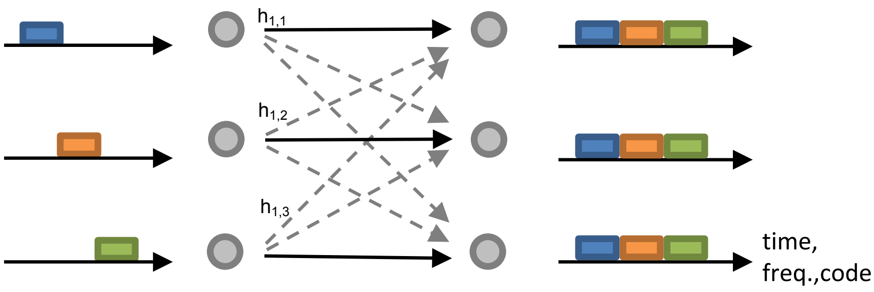

Figure 2.1: Representation of an orthogonal multiple access scheme for a 3-user interference channel.

Orthogonal Schemes in K-user Interference Channel

Considering a K-user interference channel depicted in Fig. 2.1, the signal received at receiver k is the sum of the signals from all transmitters which can be written as

$$y_k = \sum_{\ell=1}^{K} h_{k,\ell} x_\ell + n_k, \tag{2.4}$$

where $h_{k,\ell}$ is the channel gain from transmitter ℓ to receiver k and $n_k \sim \mathcal{CN}(0, \sigma^2)$ is the AWGN at receiver k. The SNR is defined as $\mathrm{SNR} = \frac{\mathbb{E}|x_\ell|^2}{\sigma^2}$ with $\mathbb{E}|x_\ell|^2$ denoting the transmit power. As commented before, orthogonal schemes allow each user to access a portion of the resources, e.g. users are allocated in different time slots via time division multiple access (TDMA) or frequency bands via frequency division multiple access (FDMA). The DoF in K-user interference channels can be calculated as

$$d = \lim_{\mathrm{SNR}\to\infty} \frac{\sum_{k=1}^{K} \frac{1}{K} \log_2(1 + K|h_{k,k}|^2 \mathrm{SNR})}{\log_2(\mathrm{SNR})} \tag{2.5}$$

$$= \lim_{\mathrm{SNR}\to\infty} \frac{\log_2(\mathrm{SNR}) + \sum_{k=1}^{K} \log_2(K|h_{k,k}|^2)}{\log_2(\mathrm{SNR})} = 1, \tag{2.6}$$

where the factor $1/K$ in (2.5) shows that the total available resources are equally shared among K users. As a result, orthogonal access schemes guarantee that each user gets a fraction of the total DoF and the sum of these fractions is equal to 1.

It is also conjectured in [12] that the maximum achievable DoF per user in a K-user interference channel is $1/K$, therefore the total DoF would not scale with K. From the receivers' point of view, the transmission is interference-free, but orthogonal access schemes are proven to be suboptimal in terms of spectral efficiency. An example of a 3-user interference channel using orthogonal multiple access is shown in Fig. 2.1. Each user transmits over 1/3 of the total dimension, while a 2/3 fraction of the dimension is spanned by the interference signals. In fact, if the dimensions of the interference subspace can be reduced, more interference-free subspace dimensions can be utilized for the transmission of the desired signal. This concept is called "interference alignment (IA)".

IA in K-user Interference Channels

The result presented by Cadambe and Jafar [11] demonstrates that regardless of the number of users, it is possible for each transmitter-receiver pair to have an interference-free communication for half the time or using half the bandwidth. Accordingly, in a K-user SISO interference channel, the capacity per user k as a function of SNR can be characterized as

$$C_k(\mathrm{SNR}) = \frac{1}{2}\log_2(\mathrm{SNR}) + o\left(\log_2\left(\mathrm{SNR}\right)\right). \tag{2.7}$$

The sum capacity of the K-user interference channel increases linearly with the number of users and becomes

$$C(\mathrm{SNR}) = \frac{K}{2}\log_2(\mathrm{SNR}) + o\left(\log_2\left(\mathrm{SNR}\right)\right). \tag{2.8}$$

Consequently, the total achievable DoF of the K-user interference channel are $K/2$. Fig. 2.2 shows a 3-user interference channel using IA, where each user can get a fraction $1/2$ of the total dimension, regardless of the number of users. The two interference signals are aligned into the other $1/2$ of the dimension. A simple example to achieve this is to assume that all direct channels have delay 1 and cross channels have delay 2.

IA can be achieved by exploiting the available signaling dimensions in time [37], frequency [38,39], space [40,41], or/and code [42]. In the following sections, we focus on two types of interference channels exploiting time/frequency and spatial dimensions, respectively: 1) the K-user SISO interference channel with time/frequency varying channel coefficients and 2) the K-user MIMO interference channel with constant channel coefficients.

2.2 IA for K-user SISO Interference Channels

Considering a K-user SISO interference channel where each user is equipped with a single antenna, IA can be achieved by linear precoding over N symbol extensions. The extended symbols can be transmitted over parallel channels in time domain (by precoding over time-varying channels) or in frequency domain (by precoding across

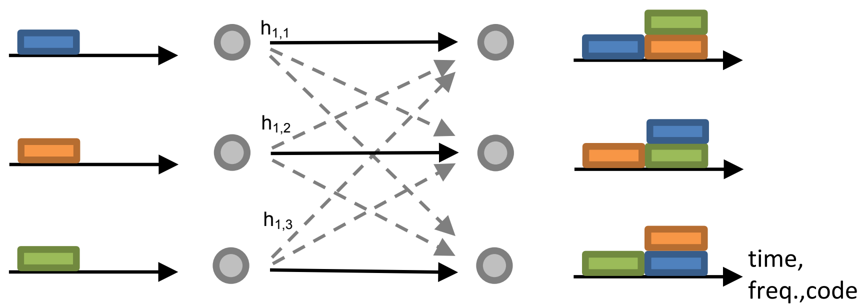

Figure 2.2: Representation of the IA concept for a 3-user interference channel.

multiple carriers for frequency-selective channels) with the assumption of varying channel coefficients [11]. The channel coefficients of the parallel channel between receiver k and transmitter ℓ is expressed as

$$\mathbf{H}_{k,\ell} = \begin{bmatrix} h_{k,\ell}^1 & 0 & \dots & 0 \\ 0 & h_{k,\ell}^2 & \dots & 0 \\ \vdots & \vdots & \ddots & \vdots \\ 0 & 0 & \dots & h_{k,\ell}^N \end{bmatrix} . \tag{2.9}$$

Note that the original channel is a scalar channel, therefore the expanded channel matrix $\mathbf{H}_{k,\ell}$ is a diagonal matrix, $\forall k, \ell \in \{1, \dots, K\}$. The transmitted symbol over all N channel accesses is

$$\mathbf{x}_k = \sum_{i=1}^{d_k} \mathbf{v}_k^i s_k^i \tag{2.10}$$

$$= \underbrace{\left[\mathbf{v}_k^1, \mathbf{v}_k^2, \cdots, \mathbf{v}_k^{d_k}\right]}_{\mathbf{V}_k} \underbrace{\begin{bmatrix} s_k^1 \\ s_k^2 \\ \vdots \\ s_k^{d_k} \end{bmatrix}}_{\mathbf{s}_k} . \tag{2.11}$$

with $s_k^i \in \mathbb{C}$ the transmitted symbol and the associated precoding vector $\mathbf{v}_k^i \in \mathbb{C}^{N \times 1}$. The received signal at receiver k can be written as

$$\mathbf{y}_k = \mathbf{H}_{k,k}\mathbf{x}_k + \sum_{k \neq \ell} \mathbf{H}_{k,\ell}\mathbf{x}_\ell + \mathbf{n}_k , \tag{2.12}$$

where $\mathbf{n}_k \sim \mathcal{CN}(0, \sigma^2 \mathbf{I}_N)$ is additive complex symmetric Gaussian noise.

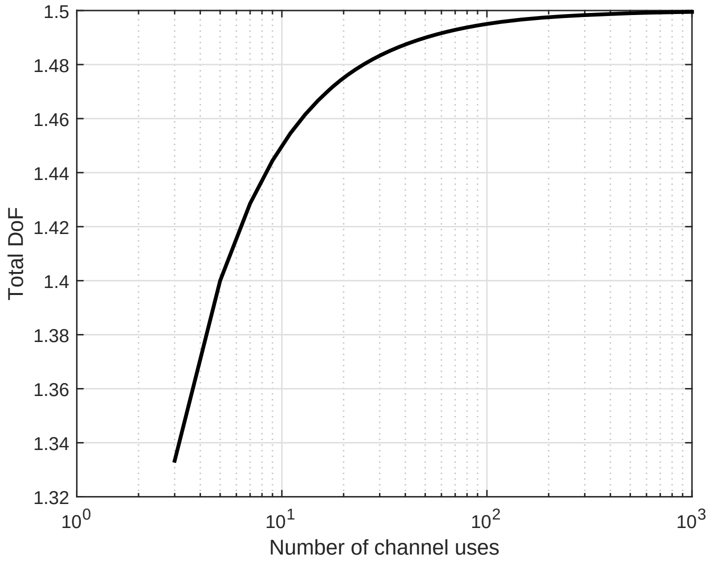

Figure 2.3: Achievable DOF of the IA scheme when $K = 3$.

2.2.1 Achievable DoF in K-user SISO Interference Channels

The minimum setup to achieve the IA solution includes $K = 3$ users precoding over $N = 3$ dimensional parallel channels. With this setting it is possible to obtain

$$(d_1, d_2, d_3) = \left(\frac{2}{3}, \frac{1}{3}, \frac{1}{3}\right) \tag{2.13}$$

and therefore total DoF $\sum_{k=1}^{3} d_k = 4/3$. This is still far away from the maximum DoF of $3/2$ for a 3-user SISO interference channel. Let us define $N = 2b + 1$, where b is a non-negative integer. There exist IA solution for any integer values of b [11]. The achievable DoF per symbol can be characterized as

$$(d_1, d_2, d_3) = \left(\frac{b+1}{2b+1}, \frac{b}{2b+1}, \frac{b}{2b+1}\right). \tag{2.14}$$

As a result, precoding over more channel accesses N is necessary to approach the DoF of the channel. When $b \to \infty$, a total DoF of $3/2$ can be achieved asymptotically. In Fig. 2.3, the total achievable DoF per symbol are shown for the original IA scheme [11] when $K = 3$ users.

The generalization to $K \geq 3$ is studied in [11, Appendix III]. In order to achieve an IA solution, the number of channel accesses must satisfy

$$N = (b+1)^{(K-2)(K-1)-1} + b^{(K-2)(K-1)-1} \tag{2.15}$$

to be able to transmit

$$d_k = \begin{cases} (b+1)^{(K-2)(K-1)-1}, & k = 1 \\ b^{(K-2)(K-1)-1}, & k \in \{2,3,\ldots,K\}. \end{cases} \tag{2.16}$$

data symbols. Again, if b is asymptotically large, the DoF per symbol of the K-user SISO interference channel become

$$\lim_{b\to\infty} \frac{\sum_{i=1}^{d_k}}{N} = \lim_{b\to\infty} \frac{(b+1)^{(K-2)(K-1)-1} + (K-1)b^{(K-2)(K-1)-1}}{(b+1)^{(K-2)(K-1)-1} + b^{(K-2)(K-1)-1}} = \frac{K}{2}. \tag{2.17}$$

For some specific numbers of symbol extensions, an improved IA solutions is proposed in [43], which achieves higher DoF with finite symbol extensions N compared to the original IA scheme [11].

2.2.2 IA Solution in 3-user SISO Interference Channels

In this section, we review the first closed-form IA solution for 3-user SISO interference channels proposed in [11]. The key idea of IA is to construct the precoding matrices in a way such that the interference from different transmitters are aligned into a subspace with less signal dimensions. Fig. 2.4 shows the alignment solution to achieve DoF $(d_1, d_2, d_3) = (2/3, 1/3, 1/3)$ over $N = 3$ symbol extensions. User 1 achieves 2 DoF by transmitting two independently streams along the precoding vectors $\mathbf{v}_1^1, \mathbf{v}_1^2$ while users 2 and 3 achieve 1 DoF by sending one stream along $\mathbf{v}_2$ and $\mathbf{v}_3$, respectively. At the receiver side, the interference signals $\mathbf{H}_{1,2}\mathbf{v}_2$ and $\mathbf{H}_{1,3}\mathbf{v}_3$ at receiver 1 are aligned in the same direction spanning a one dimensional subspace. The desired signal $\mathbf{H}_{1,1}\mathbf{V}_1$ spans a two dimensional subspace. At receivers 2 and 3, the interference signals $\mathbf{H}_{2,1}\mathbf{V}_1$, $\mathbf{H}_{2,3}\mathbf{v}_3$ and $\mathbf{H}_{3,1}\mathbf{V}_1$, $\mathbf{H}_{3,2}\mathbf{v}_2$ are aligned into two dimensional subspaces, leaving one interference-free dimension for the desired signal.

To achieve perfect IA, the following conditions must be satisfied

$$\mathbf{H}_{1,2}\mathbf{V}_2 = \mathbf{H}_{1,3}\mathbf{V}_3 \tag{2.18}$$

$$\mathbf{H}_{2,3}\mathbf{V}_3 \prec \mathbf{H}_{2,1}\mathbf{V}_1 \tag{2.19}$$

$$\mathbf{H}_{3,2}\mathbf{V}_2 \prec \mathbf{H}_{3,1}\mathbf{V}_1 \tag{2.20}$$

where $\mathbf{A} \prec \mathbf{B}$ denotes that the column space of $\mathbf{A}$ is a subset of the column space of $\mathbf{B}$. Transmitter 1 sends $b+1$ independent streams. To be able to obtain $b+1$ interference-free subspace dimensions from $2b+1$ total dimensions, the interference

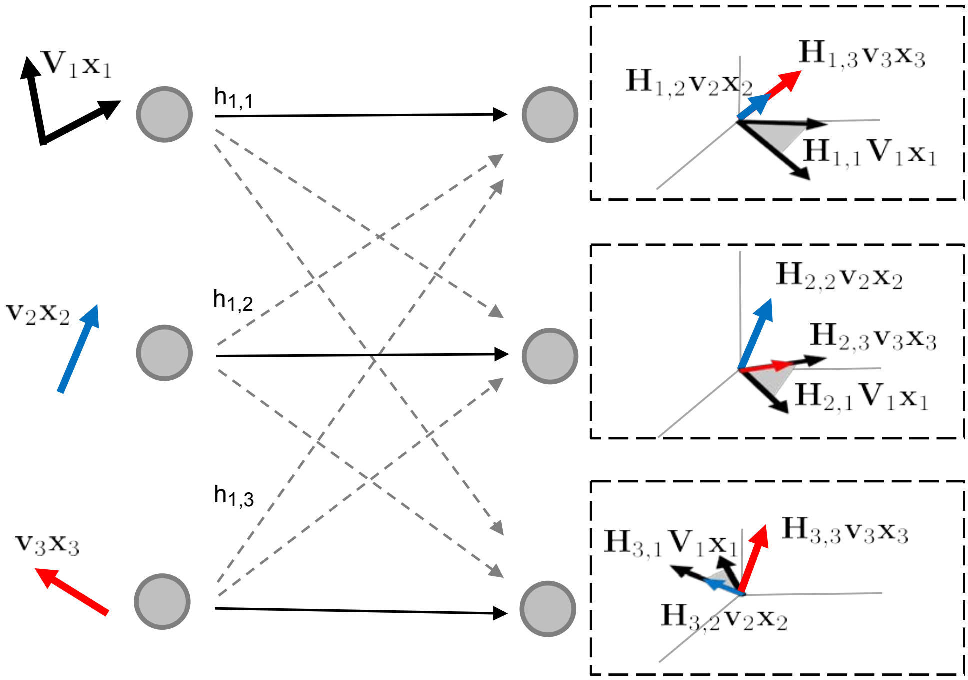

Figure 2.4: An example of IA for 3-user SISO interference channels with $N = 3$ and $(d_1, d_2, d_3) = (2/3, 1/3, 1/3)$.

signals from transmitter 2 and 3 must be aligned into a subspace with dimension smaller than b, i.e.

$$\operatorname{rank}\left([\mathbf{H}_{1,2}\mathbf{V}_2\ \mathbf{H}_{1,3}\mathbf{V}_3]\right) \leq b. \tag{2.21}$$

Therefore, transmitter 2 and 3 can send b independent streams, respectively. To be able to extract b interference-free dimensions, interference signals must span a subspace with a dimension not greater than $b + 1$ at receiver 2 and 3, i.e.

$$\operatorname{rank}\left([\mathbf{H}_{2,1}\mathbf{V}_1\ \mathbf{H}_{2,3}\mathbf{V}_3]\right) \leq b + 1 \tag{2.22}$$

$$\operatorname{rank}\left([\mathbf{H}_{3,1}\mathbf{V}_1\ \mathbf{H}_{3,2}\mathbf{V}_2]\right) \leq b + 1. \tag{2.23}$$

Cadambe and Jafar show that the above conditions are satisfied simultaneously, if the precoders and decoders are designed as follows

$$\mathbf{V}_1 = \left[\mathbf{1}_{N\times 1}, \mathbf{T}\mathbf{1}_{N\times 1}, \cdots, \mathbf{T}^b\mathbf{1}_{N\times 1}\right] \tag{2.24}$$

$$\mathbf{V}_2 = \mathbf{H}_{3,2}^{-1}\mathbf{H}_{3,1}\left[\mathbf{1}_{N\times 1}, \mathbf{T}\mathbf{1}_{N\times 1}, \cdots, \mathbf{T}^{b-1}\mathbf{1}_{N\times 1}\right] \tag{2.25}$$

$$\mathbf{V}_3 = \mathbf{H}_{2,3}^{-1}\mathbf{H}_{2,1}\left[\mathbf{T}\mathbf{1}_{N\times 1}, \mathbf{T}^2\mathbf{1}_{N\times 1}, \cdots, \mathbf{T}^b\mathbf{1}_{N\times 1}\right] \tag{2.26}$$

where

$$\mathbf{T} = \mathbf{H}_{1,2}\mathbf{H}_{2,1}^{-1}\mathbf{H}_{2,3}\mathbf{H}_{3,2}^{-1}\mathbf{H}_{3,1}\mathbf{H}_{1,3}^{-1}. \tag{2.27}$$

To guarantee that each receiver can decode its own message, it is necessary to verify the linear interdependency of the column vectors in the signal space and interference space. The interdependency is achieved in [11] using two facts: 1) Channel coefficients are drawn randomly, and 2) The precoders have Vandermonde structure, i.e. precoders with the terms of a geometric progression in each row.

Since the original work [11] focuses only on the DoF, [44] improves the sum rate performance by optimization of precoding vectors. The precoder design is obtained as a global solution of a constrained convex (concave) optimization problem.

2.3 IA for K-user MIMO Interference Channels

IA using symbol extension requires a large number of channel accesses (e.g. time slots and/or frequency subcarriers) in order to achieve the optimal DoF. In this section, we consider the interference channel with the transmitters and receivers equipped with N_T and N_R antennas, respectively. The channels $\mathbf{H}_{k,\ell} \in \mathbb{C}^{N_\mathrm{R}\times N_\mathrm{T}}$ from receiver k to tranmistter ℓ, $\forall k, \ell \in \{1, \dots, K\}$ have i.i.d. entries and remain constant over the duration of the transmission. The received signal at receiver k can be written as

$$\mathbf{y}_k = \mathbf{H}_{k,k}\mathbf{x}_k + \sum_{k\neq\ell}\mathbf{H}_{k,\ell}\mathbf{x}_\ell + \mathbf{n}_k\,, \tag{2.28}$$

where the additive complex symmetric white Gaussian noise $\mathbf{n}_k \sim \mathcal{CN}(0, \sigma^2\mathbf{I}_{N_\mathrm{R}})$ has zero mean and unit variance. The SNR is defined as $\frac{P}{\sigma^2}$, where P denotes the transmit power $\mathbb{E}\{\mathbf{x}_\ell^\mathrm{H}\mathbf{x}_\ell\}$. The linearly precoded transmitted symbol $\mathbf{x}_k$ can be written as

$$\mathbf{x}_k = \sum_{i=1}^{d_k}\mathbf{v}_k^i s_k^i = \mathbf{V}_k\mathbf{s}_k \tag{2.29}$$

where all d_k symbols $\mathbf{s}_k$ are spread over all N_T transmit antennas using the precoding matrix $\mathbf{V}_k = [\mathbf{v}_k^1, \dots, \mathbf{v}_k^{d_k}]$.

2.3.1 Achievable DoF in K-user MIMO Interference Channels

For a specific channel configuration, feasibility conditions indicate the existence of IA solutions. In [45], IA problems are classified as either proper or improper, depending on whether or not the number of equations exceeds the number of variables. It is

Algorithm 1 Iterative Interference Alignment

Input: Channel matrix $\mathbf{H}_{k,\ell}$, $k \neq \ell$, interference leakage threshold ε
Output: Precoders $\mathbf{V}_\ell$ and decoders $\mathbf{U}_k$, $\forall k, \ell \in 1, \ldots, K$
begin
Generate random $\mathbf{V}_\ell$ $\forall \ell \in \{1, \ldots, K\}$, such that $\mathbf{V}_\ell^{\mathrm{H}} \mathbf{V}_\ell = \mathbf{I}_d$.
repeat
for all $k \in \{1, \ldots, K\}$ **do**

$$\mathbf{R}_k = \sum_{\ell=1, \ell \neq k}^{K} \mathbf{H}_{k,\ell} \mathbf{V}_\ell \mathbf{V}_\ell^{\mathrm{H}} \mathbf{H}_{k,\ell}^{\mathrm{H}}, \quad \mathbf{U}_k = \left[\overrightarrow{\mathbf{u}}_{N_{\mathrm{R}}-d+1}(\mathbf{R}_k), \ldots, \overrightarrow{\mathbf{u}}_{N_{\mathrm{R}}}(\mathbf{R}_k) \right]$$

end for
for all $\ell \in \{1, \ldots, K\}$ **do**

$$\mathbf{R}_\ell = \sum_{k=1, k \neq \ell}^{K} \mathbf{H}_{k,\ell}^{\mathrm{H}} \mathbf{V}_\ell^{\mathrm{H}} \mathbf{V}_\ell \mathbf{H}_{k,\ell}, \quad \mathbf{V}_\ell = \left[\overrightarrow{\mathbf{u}}_{N_{\mathrm{T}}-d+1}(\mathbf{R}_\ell), \ldots, \overrightarrow{\mathbf{u}}_{N_{\mathrm{T}}}(\mathbf{R}_\ell) \right]$$

end for
until $\mathcal{I} \leq \varepsilon$
end

verified that IA is surely feasible if a system is proper [45, 46], i.e. the number of equations is not larger than the number of variables. The number of equations is $N_{\mathrm{e}} = (K+1)d$ and the number of variables equals $N_{\mathrm{v}} = N_{\mathrm{T}} + N_{\mathrm{R}}$. Therefore, the symmetric interference channel $(N_{\mathrm{R}} \times N_{\mathrm{T}}, d)^K$ is feasible if and only if [45, 46]

$$N_{\mathrm{T}} + N_{\mathrm{R}} - (K-1)d \geq 0. \tag{2.30}$$

2.3.2 IA Solution in 3-user MIMO Interference Channels

The design of precoders and decoders is essential to achieve the promised DoF of IA. For MIMO IA, a closed-form solution is first proposed in [11, 47] for 3-user interference channels with $N_{\mathrm{R}} = N_{\mathrm{T}} = M$, where DoF per user $d = M/2$ can be guaranteed. Other closed-form solutions are available for some specific channel configurations [45, 46].

Since the closed-form solution is still not feasible in general, iterative IA algorithms have been proposed as an alternative to achieve IA in MIMO interference channels [41, 47, 48]. The iterative algorithms mainly rely on channel reciprocity based on time-division duplex (TDD) operation, relaxing the need of global CSI. The iterative algorithms also provide a numerical mean to verify the feasibility of IA for given interference channel configurations. The algorithm that aims to minimize the interference leakage metric

$$\mathcal{I} = \sum_{k=1}^{K} \sum_{\ell=1,\ell\neq k}^{K} \|\mathbf{U}_k^{\mathrm{H}} \mathbf{H}_{k,\ell} \mathbf{V}_\ell\|_{\mathrm{F}}^2 \tag{2.31}$$

is proposed in [41]. The algorithm proceeds by alternatively optimizing $\mathbf{U}_k$ and $\mathbf{V}_\ell$ as shown in Algorithm 1. In particular, every recevier i calculates the interference covariance matrix and selects the subspace which contains the smallest interference power. The d eigenvectors corresponding to this subspace are used as $\mathbf{U}_k$. In the reciprocal channel, the roles of transmitters and receivers are interchanged and $\mathbf{U}_k$ is served as precoding matrix. The calculation of the interference subspace containing the least interference and selection of the eigenvectors is performed in the reciprocal channel. The matrix $\mathbf{V}_\ell$ is obtained as the eigenvectors associate to the d smallest eigenvalues. The process of updating $\mathbf{U}_k$ and $\mathbf{V}_\ell$ will continue until all K interference covariance matrices become rank-deficient, implying that the interference signals from different transmitters are aligned into the same subspace. In practice, this is done by comparing the interference leakage $\mathcal{I}$ with a pre-defined threshold ε. The alignment solution to achieve DoF $(d_1, d_2, d_3) = (1/2, 1/2, 1/2)$ with $N_{\mathrm{R}} = N_{\mathrm{T}} = 2$ is pictured in Fig. 2.5. Every transmitter sends one stream by precoding using a two dimensional vector. With IA, two interference signals at each receiver are aligned in one dimension. In the two dimensional receive signal space, one dimension is left for the intended stream.

While the IA algorithm performs well at high SNR, it is not optimal at medium and low SNRs. This is due to the reason that this algorithm aims at perfect IA and does not take into account the power of the desired signal during the iterative process. The Max-SINR alogorithm in [41] tries to improve the low SNR performance by maximizing the per-stream SINR at each iteration. By relaxing the need of perfect IA, the Max-SINR algorithm achieves a higher rate at low SNRs compared to IA. Other algorithms that have relaxed alignment requirement and employ other metrics are covered in [47, 48]. For instance, the objective in [48] is to maximize the network sum rate. In [47], a modified metric taking into account uncoordinated interference is used for a joint MMSE filter design.

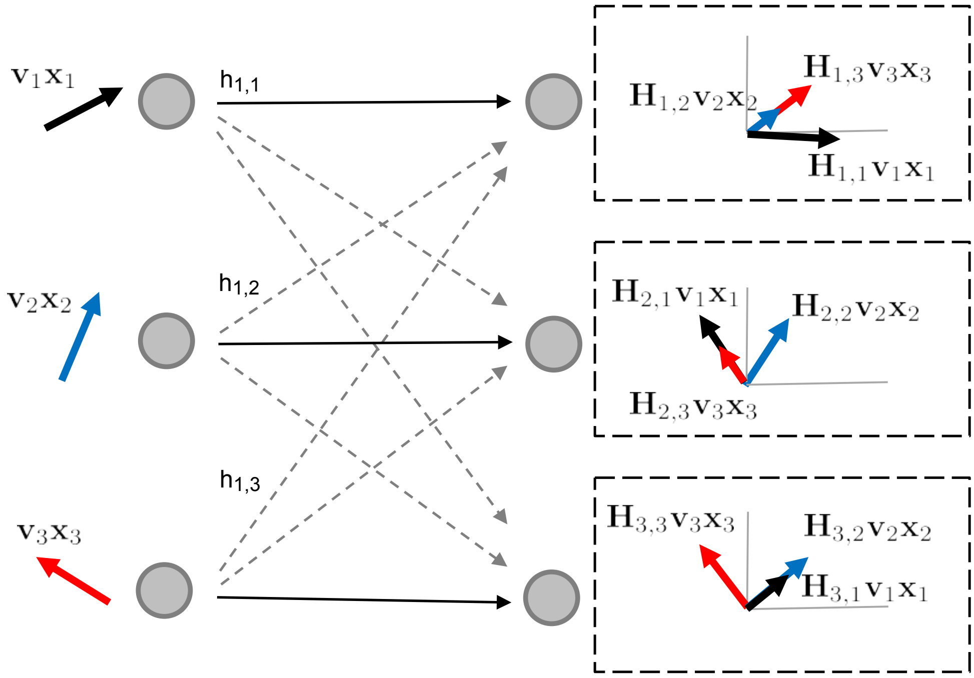

Figure 2.5: An example of IA for 3-user MIMO interference channels with $N_\mathrm{R} = N_\mathrm{T} = 2$ and $(d_1, d_2, d_3) = (1/2, 1/2, 1/2)$.

2.4 CSI Feedback for Interference Alignment

For single-user MIMO systems with channel state information (CSI) at the receiver, the capacity of the channel scales with the minimum of the number of transmit/receive antennas [49]. In multiuser systems, adapting the transmission among multiple transmitters can efficiently minimize the effect of interference. As a result, CSI has gained much more significance [50]. For instance, calculating IA precoders requires accurate knowledge of the interference generated by each transmitter. CSI imperfection degrades IA performance. Assuming the imperfect channel matrix is the summation of the true channel matrix and an independent error matrix, the impact of imperfect CSI on IA has been investigated in [51–54]. The work of [51] derives both upper and lower bounds on the achievable rates assuming noisy CSI. The error performance of IA is studied in [52] and adaptive schemes are proposed to introduce robustness against CSI imperfection. The performance loss of IA under CSI mismatch for interference channels is studied in [53] showing that full DoF are achievable if the variance of the CSI measurement error is proportional to the inverse of the SNR. Similar results are found in [54] for interference broadcast channels.

In TDD systems, the reciprocity of downlink and uplink channels can be used to acquire CSI. In frequency-division duplex (FDD) systems, CSI needs to be estimated and fed back to the transmitter via a feedback link. For interference channels, the channel knowledge at transmitters can be exploited to reduce the interference signal dimensions and thus achieve the optimal DoF promised by IA. An existing method to provide high quality feedback with low feedback rate is limited feedback [50], i.e. CSI quantization. In [38], channel coefficients are quantized using a Grassmannian codebook for frequency-selective SISO interference channels. The work in [55–57] extends the result to MIMO interference channels. Both [38] and [55] show that the full DoF are achievable as long as the feedback rate scales with the transmit power.

In this section, we provide an overview of the most notable work on limited feedback for SISO IA and MIMO IA, respectively.

2.4.1 Limited feedback for SISO Interference Alignment

SISO IA with symbol extensions does not distinguish between time and frequency dimensions [11, 38]. The original scheme was presented for time-selective channels, however, it would require non-causal feedback. In the following, vector quantization of the channel coefficients in frequency-selective channels is considered [38].

The S-tap time-variant sampled impulse response between transmitter ℓ and receiver k is denoted by $\mathbf{w}_{k,\ell} = [w_{k,\ell}[1], \ldots, w_{k,\ell}[S]]^{\mathrm{T}}$, $\forall k, \ell \in \{1, \ldots, K\}$, where each channel tap $w_{k,\ell}[S]$ is drawn independently. The channel frequency response between transmitter ℓ and receiver k can be represented as

$$\mathbf{h}_{k,\ell} = \mathbf{D}_{N\times S}\mathbf{w}_{k,\ell}, \tag{2.32}$$

where $\mathbf{D}_{N\times S}$ is the $N\times S$ submatrix of the $N\times N$ DFT matrix $\mathbf{D}_N$. The DFT matrix $\mathbf{D}_N$ is defined as $[\mathbf{D}_N]_{i,j} = \frac{1}{\sqrt{N}}e^{-j2\pi(i-1)(j-1)/N}$, $\forall i, j \in \{1, \ldots, N\}$. The diagonal matrix containing the channel frequency response is defined as $\mathbf{H}_{k,\ell} = \mathrm{diag}\left(\mathbf{h}_{k,\ell}\right)$.

To calculate IA precoders, the vector $\mathbf{w}_{k,\ell}$ must be fed back to the transmitter side. As shown in [38], $\mathbf{w}_{k,\ell}$ can be quantized on the Grassmannian manifold using a codebook $\mathcal{C}$ with $2^{N_{\text{bits}}}$ codewords and N_{bits} is the number of feedback bits. Each codeword $\mathbf{c}_j \in \mathcal{C}$ is an unit norm vector i.e. $\|\mathbf{c}_j\|^2 = 1,\ \forall j \in \{1, \ldots, 2^{N_{\text{bits}}}\}$.

Let us define the chordal distance $d_{\mathrm{c}}(\mathbf{x}_1, \mathbf{x}_2) = \sqrt{(1 - |\mathbf{x}_1^{\mathrm{H}}\mathbf{x}_2|^2)}$ between two unit norm vectors $\mathbf{x}_1$ and $\mathbf{x}_2$. The receiver k calculates the chordal distance d_{c} between $\mathbf{w}_{k,\ell}$ and every codeword in the codebook $\mathcal{C}$ and feeds back the index of the codeword which minimizes the chordal distance. Based on the feedback indices from the receiver, the transmitters can obtain the quantized version of channel vectors

$\mathbf{w}_{k,\ell}, \forall k \neq \ell$. Then, IA solutions can be calculated according to the quantized channel vectors. In particular, the quantized vector $\hat{\mathbf{w}}_{k,\ell}$ is chosen according to

$$\hat{\mathbf{w}}_{k,\ell} = \underset{\mathbf{c}_j \in \mathcal{C}}{\arg\min} \quad d_{\mathrm{c}}\left(\frac{\mathbf{w}_{k,\ell}}{\|\mathbf{w}_{k,\ell}\|}, \mathbf{c}_j\right). \tag{2.33}$$

2.4.2 Limited feedback for MIMO Interference Alignment

In this section, we review the IA limited feedback scheme proposed in [55]. According to [55], receiver k forms and feeds back an aggregated channel matrix $\mathcal{H}_k \in \mathbb{C}^{N_{\mathrm{R}}N_{\mathrm{T}}\times(K-1)}$ as

$$\mathcal{H}_k = \left[\bar{\mathbf{h}}_{k,1}, \ldots, \bar{\mathbf{h}}_{k,k-1}, \bar{\mathbf{h}}_{k,k+1}, \ldots, \bar{\mathbf{h}}_{k,K}\right]. \tag{2.34}$$

The unit-norm vectors $\bar{\mathbf{h}}_{k,\ell} \in \mathbb{C}^{N_{\mathrm{R}}N_{\mathrm{T}}\times 1}$ are obtained by vectorizing the elements of matrices $\mathbf{H}_{k,\ell}$, i.e.

$$\bar{\mathbf{h}}_{k,\ell} = \frac{\mathrm{vec}\left(\mathbf{H}_{k,\ell}\right)}{\|\mathrm{vec}\left(\mathbf{H}_{k,\ell}\right)\|}. \tag{2.35}$$

The vector $\bar{\mathbf{h}}_{k,k}$ corresponding to $\mathbf{H}_{k,k}$ is eliminated from the aggregated matrix $\mathcal{H}_k$. Using the concept of composite Grassmannian manifold, the matrix $\mathcal{H}_k$ can be quantized using a codebook $\mathcal{C}$ with $2^{N_{\mathrm{bits}}}$ codewords and N_{bits} is the number of feedback bits. Each codeword $\mathbf{C}_j = [\mathbf{c}_j^{[1]}, \ldots, \mathbf{c}_j^{[K-1]}] \in \mathcal{C}$ is a $N_{\mathrm{R}}N_{\mathrm{T}} \times (K-1)$ matrix with $\|\mathbf{c}_j^{[\ell]}\| = 1$. The squared distance between $\mathbf{C}_j$ and $\mathcal{H}_k$ is defined as

$$d_{\mathrm{s}}\left(\mathcal{H}_k, \mathbf{C}_j\right) = \sum_{l=1}^{K-1} d_{\mathrm{c}}^2\left([\mathcal{H}_k]_{:,\ell}, \mathbf{c}_j^{[\ell]}\right), \tag{2.36}$$

which is a commonly used distance measure on the composite Grassmannian manifold. The quantized channel $\hat{\mathcal{H}}_k$ is selected as

$$\hat{\mathcal{H}}_k = \underset{\mathbf{C}_j \in \mathcal{C}}{\arg\min} \quad d_{\mathrm{s}}\left(\mathcal{H}_k, \mathbf{C}_j\right). \tag{2.37}$$

Further advancement on limited feedback for MIMO IA has been made in [56,57]. In [56], an iterative algorithm is proposed to reduce the quantization error. The work in [57] removes redundant information in the quantization procedure by exploiting the structure of IA equations and therefore yields a better sum rate performance.

3 Interference Alignment in Time-variant Channels

As discussed in Chapter 2, interference alignment (IA) is able to achieve optimal degrees of freedom (DoF) in interference channels. However, the implementation of IA faces a lot of difficulties in wireless systems. The necessity of channel state information (CSI) at the transmitter is one of the major challenges. Moreover, the accuracy of the CSI should improve as the SNR increases in order to achieve the DoF gain promised by IA [53]. Many existing works assume perfect CSI. However, this is not true in practical systems due to the channel estimation error and the limited capacity of the feedback link. In this chapter, we aim to devise a channel estimation, feedback and prediction framework for IA in time variant channels.

3.1 Background

Imperfect CSI degrades IA performance. The impact of imperfect CSI on the sum rate of IA is analyzed in [51–54] (see Section 2.4). For frequency-division duplex (FDD) systems, CSI needs to be estimated and fed back to the transmitter. Limited feedback via quantization is a promising approach to transfer CSI to the transmitter side. Several approaches address the problem of limited feedback for IA [38,55,56,58, 59] assuming perfect channel estimation. In [38], channel coefficients are quantized using a Grassmannian codebook for frequency-selective single-input single-output (SISO) channels. The work in [55] extends the results to multiple-input multiple-output (MIMO) channels. Both [38] and [55] show that the full DoF are achievable as long as the feedback rate is high enough (which scales with the transmit power). This result aligns with the one that is found for MIMO broadcast channels in [60]. The work in [56] addresses the problem of improving the sum rate under limited feedback by involving additional iterative computation of pre-quantization filters at the receivers. To further reduce the feedback overhead, [58] considers differential limited feedback on the Grassmannian manifold by exploiting temporal correlation of the time-selective fading channels. In the context of opportunistic transmission for IA, Chapter 4 shows that multi-user diversity can be exploited based on 1-bit feedback from each user, while preserving the full DoF. Instead of quantizing the CSI, [61] considers analog feedback and shows that the DoF of IA can be preserved as long as the forward and reverse link SNRs scale together.

However, for a practical system, the imperfection of CSI is caused by various aspects:

(a) For time-variant channels, CSI is acquired with the aid of pilot symbols. The channel varies over time due to the mobility of the users. If the channel changes after the transmission of the pilot symbols, the receiver cannot detect the channel variation, which leads to a reduction in sum rate due to the use of outdated channel estimates.

(b) For FDD, CSI is fed back through limited capacity feedback channels. The error due to quantized feedback degrades the IA performance.

(c) The feedback information arrives at the transmitter with a delay which causes a further performance degradation.

A related body of research tackling the above mentioned problems exists for single-cell multiuser MIMO systems [62, 63]. For interference channels, [64] studies (a) and (b) for MIMO IA using a minimum mean square error (MMSE) estimator. The studies in [62–64] consider block fading channels. The work of [65] extends [64] considering time-selective continuous fading in the payload part, while assuming constant fading for the training part.

In this chapter, we jointly consider (a)-(c) for IA in wideband SISO systems with symbol extension over frequency [11], i.e. precoding across orthogonal frequency dimensions. Although we present our results for SISO interference channels, the complete strategy can be generalized to MIMO interference channels using a method similar to [55] by vectorization of channel matrices.

In Section 3.3, we tackle the problems (a) and (c) by reduced-rank channel prediction using discrete prolate spheroidal (DPS) sequences [66]. Thanks to the energy concentration of the sequences in the Doppler domain, we are able to describe the channel evolution by only a few subspace coefficients. In Section 3.4, we address problem (b) and show that the subspace coefficients can be quantized and fed back using vector quantization, which greatly reduces the redundancy of the codebook by exploiting the rotation invariance. In addition, we highlight the importance to feed back the subspace coefficients in delay domain, resulting in a reduction of noise. With the subspace coefficients, the transmitter is able to perform channel prediction to combat the time selectivity of the channel. The subspace vector to be quantized has correlated entries in some cases. We characterize the second order statistics of the subspace vector, which is used for whitening the vector to match the statistics of the quantization codebook. In Section 3.5, an upper bound of the rate loss due to the channel prediction- and quantization-error is derived, which is used to facilitate an adaptive subspace dimension switching algorithm. We show that there exists a tradeoff between quantization error and prediction error at a given feedback rate. The subspace dimension switching algorithm is efficient to capture the tradeoff and find the subspace dimension associated with a higher rate. Besides, we characterize the scaling of the required number of feedback bits to decouple the rate loss due to quantization from the transmit power.

3.2 K-user Time- and Frequency-Selective SISO Interference Channel

Let us consider a K user time- and frequency-selective SISO interference channel, which consists of K transmitter and receiver pairs. We denote by $h_{k,\ell}(t,\tau)$ the time-variant impulse response between transmitter ℓ and receiver k, where t is time and τ is delay. Orthogonal frequency division multiplexing (OFDM) is used to convert the time- and frequency- selective channel into N parallel time-selective and frequency-flat channels. The sampled impulse response is defined as $h_{k,\ell}[m,s] = h_{k,\ell}(mT_\mathrm{s}, sT_\mathrm{c})$, where $1/T_\mathrm{c}$ is the bandwidth and $T_\mathrm{s} = (N+G)T_\mathrm{c}$ denotes the OFDM symbol duration with a cyclic prefix length G. The S-tap time-variant sampled impulse response between transmitter ℓ and receiver k is denoted by $\mathbf{h}_{k,\ell}[m] = [h_{k,\ell}[m,1], \ldots, h_{k,\ell}[m,S]]^\mathrm{T}$, $\forall k,\ell \in \{1,\ldots,K\}$. Every element of the channel impulse response vector $\mathbf{h}_{k,\ell}[m]$ is independent identically distributed (i.i.d.) with a power delay profile (PDP) $\mathbb{E}\{\mathbf{h}_{k,\ell}[m]\mathbf{h}_{k,\ell}[m]^\mathrm{H}\} = \mathrm{diag}(\left[p_{k,\ell}^1, \ldots, p_{k,\ell}^S\right])$. We assume $\sum_{s=1}^S p_{k,\ell}^s = N$.

The variation of a wireless channel for the duration of the transmission of a data packet is caused by user mobility and multipath propagation. We define the normalized Doppler frequency of the time-selective fading process $\{h_{k,\ell}[m,s]\}$ as

$$\nu_\mathrm{D} = f_\mathrm{D} T_\mathrm{s} \tag{3.1}$$

where f_D denotes the Doppler frequency in Hertz (Hz). The temporal covariance function over consecutive OFDM symbols becomes

$$R_{\mathbf{h}_{k,\ell}}[m] = \mathbb{E}\{\mathbf{h}_{k,\ell}[l]^\mathrm{H}\mathbf{h}_{k,\ell}[l+m]\}. \tag{3.2}$$

The temporal covariance matrix is defined as $[\mathbf{R}_{\mathbf{h}_{k,\ell}}]_{i,m} = R_{\mathbf{h}_{k,\ell}}[i-m]$ for $i,m \in [0,\ldots,M-1]$.

Using OFDM, The observed frequency selective channel can be converted into N narrowband frequency-flat channels as

$$\mathbf{w}_{k,\ell}[m] = \mathbf{D}_{N\times S}\mathbf{h}_{k,\ell}[m] \tag{3.3}$$

where $\mathbf{D}_{N\times S}$ is the $N \times S$ submatrix of the $N \times N$ DFT matrix $\mathbf{D}_N$. The DFT matrix $\mathbf{D}_N$ is defined as $[\mathbf{D}_N]_{i,j} = \frac{1}{\sqrt{N}} e^{-j2\pi(i-1)(j-1)/N}$, $\forall i, j \in \{1, \ldots, N\}$. The diagonal matrix containing the channel frequency response can be written as $\mathbf{W}_{k,\ell}[m] = \operatorname{diag}(\mathbf{w}_{k,\ell}[m])$.

We consider two different communication phases: (i) the CSI acquisition via pilots and (ii) the transmission of payload. In the CSI acquisition phase, the pilot symbols from different transmitters are orthogonalized in time. During the transmission of payload, all transmitters will send simultaneously. However, for a given transmitter, its signal is only intended to be received by a single user for a given signaling interval. The signal received is the superposition of the signals transmitted by all transmitters. The received signal at receiver k in these two phases can thus be modeled by

$$\mathbf{y}_k[m] = \begin{cases} \mathbf{W}_{k,k}[m]\mathbf{x}_k[m] + \mathbf{n}_k[m]\,, & m \in \mathcal{P}_k \\ \mathbf{W}_{k,k}[m]\mathbf{x}_k[m] + & \\ \qquad \sum_{k\neq\ell} \mathbf{W}_{k,\ell}\,[m]\,\mathbf{x}_\ell[m] + \mathbf{n}_k[m]\,, & \text{elsewhere} \end{cases}$$

where $\mathcal{P}_k$ denotes the pilot position indices of user k. The vector $\mathbf{x}_k[m] \in \mathbb{C}^{N\times 1}$ denotes the transmitted symbol for user k with power constraint $\mathbb{E}\{\mathbf{x}_k[m]^{\mathrm{H}}\mathbf{x}_k[m]\} = PN$, where P is the transmit power per subcarrier. Additive complex symmetric Gaussian noise at receiver k is denoted by $\mathbf{n}_k[m] \sim \mathcal{CN}(0, \mathbf{I}_N)$. The SNR is defined as $\mathrm{SNR} = P$.

In this work we consider a user velocity and carrier frequency such that the Doppler bandwidth of the fading process f_D is much smaller than the subcarrier spacing $f_{\mathrm{sc}} = \frac{1}{T_{\mathrm{c}}N}$. Hence, we assume that the inter-carrier interference can be neglected for the processing at the receiver side, see the discussion in [67, Section II].

3.2.1 SISO Interference Alignment with Perfect CSI

IA can achieve optimal DoF when infinite channel extensions exist [11]. Using IA over N orthogonal subcarriers, each transmitter k sends a linear combination of $d_k < N$ symbols $s_k^i[m]$, along the linear precoding vectors $\mathbf{v}_k^i \in \mathbb{C}^{N\times 1}$, yielding

$$\mathbf{x}_k[m] = \sum_{i=1}^{d_k} \mathbf{v}_k^i[m] s_k^i[m]\,, \tag{3.4}$$

where $s_k^i[m] \in \mathbb{C}$ denotes the transmitted symbol and $\mathbb{E}\{|s_k^i[m]|^2\} = PN/d_k$. The precoding vector $\mathbf{v}_k^i[m]$ fulfills $\|\mathbf{v}_k^i[m]\|^2 = 1$. Defining the decoding vector $\mathbf{u}_k^i[m] \in \mathbb{C}^{N\times 1}$ subject to $\|\mathbf{u}_k^i[m]\|^2 = 1$, the received signal at receiver k for symbol i can be expressed as

$$\begin{aligned}
\mathbf{u}_k^i[m]^{\mathrm{H}}\mathbf{y}_k[m] = &\underbrace{\mathbf{u}_k^i[m]^{\mathrm{H}}\mathbf{W}_{k,k}[m]\mathbf{v}_k^i[m]s_k^i[m]}_{\text{desired signal}} + \\
&\underbrace{\mathbf{u}_k^i[m]^{\mathrm{H}}\sum_{j\neq i}\mathbf{W}_{k,k}[m]\mathbf{v}_k^j[m]s_k^j[m]}_{\text{inter-stream interference}} + \\
&\underbrace{\mathbf{u}_k^i[m]^{\mathrm{H}}\sum_{\ell\neq k}\sum_{j=1}^{d_\ell}\mathbf{W}_{k,\ell}\left[m\right]\mathbf{v}_\ell^j[m]s_\ell^j[m]}_{\text{inter-user interference}} + \mathbf{u}_k^i[m]^{\mathrm{H}}\mathbf{n}_k[m]
\end{aligned} \tag{3.5}$$

for $i \in \{1,\ldots,d_k\}$ and $k \in \{1,\ldots,K\}$. Considering i.i.d Gaussian input of $s_k^i[m]$, the achievable sum rate is given by

$$R_{\mathrm{sum}}[m] = \sum_{k,i}\frac{1}{N}\log_2\left(1 + \frac{\frac{NP}{d_k}\left|\mathbf{u}_k^i[m]^{\mathrm{H}}\mathbf{W}_{k,k}[m]\mathbf{v}_k^i[m]\right|^2}{\mathcal{I}_{k,i}^1[m] + \mathcal{I}_{k,i}^2[m] + 1}\right). \tag{3.6}$$

where

$$\mathcal{I}_{k,i}^1[m] = \sum_{j\neq i}\frac{NP}{d_k}\left|\mathbf{u}_k^i[m]^{\mathrm{H}}\mathbf{W}_{k,k}[m]\mathbf{v}_k^j[m]\right|^2, \text{ and} \tag{3.7}$$

$$\mathcal{I}_{k,i}^2[m] = \sum_{\ell\neq k}\sum_{j=1}^{d_\ell}\frac{NP}{d_\ell}\left|\mathbf{u}_k^i[m]^{\mathrm{H}}\mathbf{W}_{k,\ell}[m]\mathbf{v}_\ell^j[m]\right|^2, \tag{3.8}$$

denote inter-stream interference and inter-user interference, respectively.

The precoding and decoding vectors can be designed according to [11]. Each transmitter computes the precoding vectors $\mathbf{v}_k^i[m]$ such that the interference signals from the undesired $K-1$ transmitters are aligned at all receivers leaving the interference free subspace for the intended signal. With perfect CSI, the following IA conditions should be satisfied

$$\mathbf{u}_k^i[m]^{\mathrm{H}}\mathbf{W}_{k,k}[m]\mathbf{v}_k^j[m] = 0, \quad \forall k,\ \forall i \neq j \tag{3.9}$$

$$\mathbf{u}_k^i[m]^{\mathrm{H}}\mathbf{W}_{k,\ell}[m]\mathbf{v}_\ell^j[m] = 0, \quad \forall k \neq \ell,\ \forall i,\ j \tag{3.10}$$

$$\left|\mathbf{u}_k^i[m]^{\mathrm{H}}\mathbf{W}_{k,k}[m]\mathbf{v}_k^i[m]\right| \geq c > 0, \quad \forall k,\ i \tag{3.11}$$

where c is a constant. Accordingly, the interference terms can be perfectly canceled satisfying $\mathcal{I}_{k,i}^1[m] = \mathcal{I}_{k,i}^2[m] = 0$.

3.3 Reduced-Rank Channel Estimation and Prediction

In this section, we introduce the idea of channel prediction. First, a well-known MMSE solution is given. In subsection 3.3.1, we present the reduced-rank predictor and its relation to the MMSE solution. To simplify notations, we drop the indices of transmitters and receivers and focus on the prediction problem for a specific subcarrier. Let us denote by $w[m,n]$, $n[m,n]$ $y[m,n]$ and $x[m,n]$ the n-th element of the vector $\mathbf{w}[m]$ $\mathbf{n}[m]$ $\mathbf{y}[m]$ and $\mathbf{x}[m]$, respectively. The channel samples of the n-th subcarrier over time can be written as

$$\mathbf{g}^n = [w[0,n], \ldots, w[M-1,n]]^{\mathrm{T}}, \tag{3.12}$$

where M is the length of a single data block.

A number of N_{P} pilot symbols $x[m,n] \in \{\sqrt{P}, -\sqrt{P}\}, \forall m \in \mathcal{P}$ known at the receivers allow us to acquire channel knowledge. With the pilot symbols, we obtain the noisy channel observations at $m \in \mathcal{P}$ according to $w'[m,n] = \frac{1}{P} y[m,n]x[m,n] = w[m,n] + \frac{1}{\sqrt{P}} n'[m,n]$, where $n'[m,n] = \frac{1}{\sqrt{P}} n[m,n]x[m,n]$ has the same statistical properties as $n[m,n]$. The noisy observation vector of the n-th subcarrier over time

$$\mathbf{g}'^n = \Big[w'\left[0,n\right], \ldots, w'\left[M-1,n\right] \Big]^{\mathrm{T}} \tag{3.13}$$

is used for channel prediction. Defining the $M \times 1$ vector $\mathbf{r_h}[m] = [R_\mathbf{h}[m], R_\mathbf{h}[m-1], \ldots, R_\mathbf{h}[m-M+1]]$, the estimator minimizing the MSE can be derived as [68]

$$\tilde{w}_{\mathrm{MMSE}}[m,n] = \mathbf{r}_\mathbf{h}^{(\mathcal{P})}[m]^{\mathrm{H}} (\mathbf{R}_\mathbf{h}^{(\mathcal{P})} + \frac{1}{P} \mathbf{I}_{N_{\mathrm{P}}})^{-1} \mathbf{g}'^{n(\mathcal{P})} \tag{3.14}$$

where the covariance matrix $\mathbf{R}_\mathbf{h}^{(\mathcal{P})} \in \mathbb{C}^{N_{\mathrm{P}} \times N_{\mathrm{P}}}$ of the channel at pilot positions is obtained as a sub-matrix of $\mathbf{R_h} \in$ by extracting K-spaced rows and/or columns, i.e. $[\mathbf{R}_{\mathbf{h}_{k,\ell}}^{(\mathcal{P})}]_{i,m} = [\mathbf{R}_{\mathbf{h}_{k,\ell}}]_{K(i-1)+i, K(m-1)+m}$. The vectors $\mathbf{g}'^{n(\mathcal{P})}$ contains the respective elements for $m \in \mathcal{P}$ in the same order as in (3.12). The $N_{\mathrm{P}} \times 1$ vector $\mathbf{r}_\mathbf{h}^{(\mathcal{P})}[m]$ contains the respective elements of $R_\mathbf{h}[m - m_{\mathrm{P}}]$ for $m_{\mathrm{P}} \in \mathcal{P}$ in the same order as $\mathbf{r_h}[m]$.

3.3.1 Reduced-Rank Channel Predictor

The channel $\mathbf{g}^n$ can be approximated by a reduced rank representation [66, 69], which expands $\mathbf{g}^n$ by D orthonormal basis functions $\mathbf{u}_p = [u_p[0], \ldots, u_p[M-1]]^{\mathrm{T}}$, $p \in \{0, \ldots, D-1\}$

$$\mathbf{g}^n \approx \mathbf{U}\boldsymbol{\phi}^n = \sum_{p=0}^{D-1} \phi_p^n \mathbf{u}_p \,, \tag{3.15}$$

where $\mathbf{U} = [\mathbf{u}_0, \ldots, \mathbf{u}_{D-1}]$ collects D basis vectors of a temporal covariance matrix $\mathbf{R_h}$ and $\boldsymbol{\phi}^n = [\phi_0^n, \ldots, \phi_{D-1}^n]$ contains the subspace coefficients for the channel $\mathbf{g}^n$.

Let us define $\mathbf{f}[m] = [u_0[m], \ldots, u_{D-1}[m]]^{\mathrm{T}}$, which collects the values of the basis functions at time m. The estimate of $\boldsymbol{\phi}^n$ can be calculated according to

$$\tilde{\boldsymbol{\phi}}^n = \mathbf{G}^{-1} \sum_{m \in \mathcal{P}} w'[m,n]\mathbf{f}[m]^*, \tag{3.16}$$

$$= \mathbf{G}^{-1}\mathbf{U}^{(\mathcal{P})^{\mathrm{H}}}\mathbf{g}'^{n(\mathcal{P})} \tag{3.17}$$

where $\mathbf{G} = \sum_{m\in\mathcal{P}} \mathbf{f}[m]\mathbf{f}[m]^{\mathrm{H}} = \mathbf{U}^{(\mathcal{P})^{\mathrm{H}}}\mathbf{U}^{(\mathcal{P})}$ and $\mathbf{U}^{(\mathcal{P})} = [\mathbf{u}_0^{(\mathcal{P})}, \ldots, \mathbf{u}_{D-1}^{(\mathcal{P})}]$. The vector $\mathbf{u}_p^{(\mathcal{P})}$ contains the respective elements for $m \in \mathcal{P}$ in the same order as in (3.12). Thus, the estimated (predicted) n-th subchannel at time instant $m \in \mathbb{Z}$ is given by

$$\tilde{w}[m,n] = \sum_{p=0}^{D-1} \tilde{\phi}_p^n u_p[m] = \mathbf{f}[m]^{\mathrm{T}}\tilde{\boldsymbol{\phi}}^n. \tag{3.18}$$

3.3.2 The Choice of Subspace Dimension - An Upper Bound

In wireless communication systems, detailed second-order statistics are difficult to obtain due to the short time-interval over which the channel can be assumed to be stationary [70]. For this reason, we assume incomplete second-order statistics in this work, where only the support $\mathcal{W} = (-\nu_{\mathrm{D}}, \nu_{\mathrm{D}})$ of the Doppler spectrum is known to the transmitters and receivers with $\nu_{\mathrm{D}} \ll 1/2$. For the case of unknown support, please refer to adaptive channel estimation using hypotheses test [71, 72]. The shape of the Doppler spectrum is assumed to be flat with support $\mathcal{W}$, which is given by

$$S_{\text{flat}}(\nu, \mathcal{W}) = \begin{cases} \frac{1}{|\mathcal{W}|}, & \nu \in \mathcal{W} \\ 0, & \text{otherwise.} \end{cases} \tag{3.19}$$

The covariance function of such a fading process becomes

$$R_{\text{flat}}[m, \mathcal{W}] = \frac{\sin(2\pi m \nu_{\mathrm{D}})}{\pi m |\mathcal{W}|}. \tag{3.20}$$

The corresponding covariance matrix is $[\mathbf{R}_{\text{flat}}[\mathcal{W}]]_{l,m} = R_{\text{flat}}[l-m, \mathcal{W}]$ for $l, m \in [0, \ldots, M-1]$. The eigenvector of the covariance matrix $R_{\text{flat}}[m, \mathcal{W}]$ are also known as DPS sequences [73, 74], which are utilized as the basis functions $\mathbf{u}_p[\mathcal{W}]$ in this paper. The band-limiting region of the DPS sequences $\mathbf{u}_p[\mathcal{W}]$ is chosen according to the support $\mathcal{W}$ of the Doppler spectrum of the time-selective fading process. To ease the notation, we drop $\mathcal{W}$ in the rest of the paper. Given $\mathbf{u}_p$, [66, Section III.D] shows that the DPS sequences can be extended over $\mathbb{Z}$ in the minimum-energy band-limited sense, enabling channel prediction in (3.18). The energy of the DPS sequences is most concentrated in the interval of block length M. This energy concentration is defined as

$$\kappa_p = \frac{\sum_{m=0}^{M-1} |u_p[m]|^2}{\sum_{m=-\infty}^{\infty} |u_p[m]|^2}. \tag{3.21}$$

The values κ_p are clustered near 1 for $p \leq \lceil 2\nu_\mathrm{D} M \rceil$ and decay rapidly for $p > \lceil 2\nu_\mathrm{D} M \rceil$. The optimal subspace dimension that minimizes the mean square error (MSE) for a given noise level is found to be [66]

$$\mathcal{D}_\mathrm{ub} = \underset{D\in\{1,\ldots,M\}}{\arg\min} \left(\frac{1}{|\mathcal{W}|\, M} \sum_{p=D}^{M-1} \kappa_p + \frac{D}{MP} \right). \tag{3.22}$$

Later in Section 3.5 we will see that $\mathcal{D}_\mathrm{ub}$ is the upper bound of the subspace dimension when quantized feedback is used.

Remark 1. The reduced-rank channel prediction is a close approximate of the MMSE predictor, especially at high SNR. At high SNR ($P \to \infty$), the MMSE predictor converges to a maximum-likelihood (ML) predictor i.e., $\tilde{w}_\mathrm{ML}[m,n] = \mathbf{r}_\mathbf{h}^{(\mathcal{P})}[m]^\mathrm{H} \mathbf{R}_\mathbf{h}^{-1(\mathcal{P})} \mathbf{g}'^{n(\mathcal{P})}$. For the reduced-rank predictor, more basis functions tend to be taken as $P \to \infty$ according to (3.22). Therefore, it also converges to a ML predictor due to the relationship shown in [66, Eq.38].

3.4 Training and Feedback for IA

In this section, we consider a limited feedback scheme for the subspace coefficients $\tilde{\boldsymbol{\phi}}^n$ estimated at the receiver side. Fig. 3.1 shows the working principle of the feedback system. The subspace coefficients are estimated using the pilot symbols. Each receiver estimates the channels to all K transmitters separately. To this end, the pilot symbols from different transmitters are orthogonalized in time. The number of pilot symbols M_p for each transmitter satisfies $M = KM_\mathrm{p}$. The pilot placement for the k-th transmitter is defined as

$$\mathcal{P}_k = \big\{k + (i-1)K, \text{ where } i \in \{1,\ldots,M_\mathrm{p}\}\big\}. \tag{3.23}$$

Error-free dedicated broadcast channels with delay T_D are assumed from each receiver to all the other nodes, i.e. all the transmitters and all other receivers. During

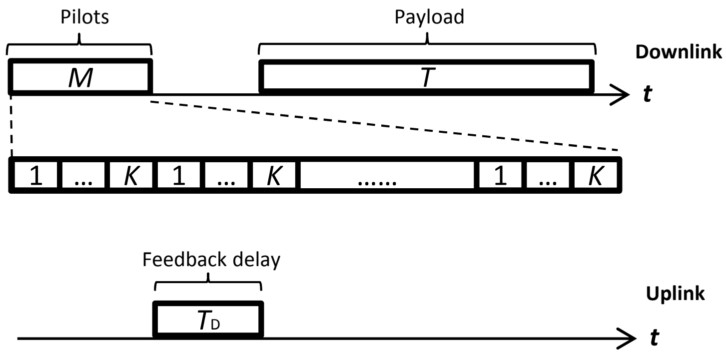

Figure 3.1: Signaling model, where M denotes the length of the pilot sequence and T the payload length.

the feedback phase, each receiver broadcasts the estimated subspace coefficients using N_d bits. Upon reception of the quantized feedback, the transmitters and receivers can calculate the IA precoders and decoders, respectively.

3.4.1 Noise Reduction

Assuming a wide-sense-stationary fading process, the N narrowband channels from the same transmitter receiver pair have the same Doppler bandwidth, thus all N fading processes share the same set of basis functions. Due to the fact that $N \geq S$, the impulse response $\mathbf{h}[m]$ contains less coefficients than the frequency response $\mathbf{w}[m]$. Thus, $\mathbf{h}[m]$ is better suited for CSI feedback.

In noise-free channels, the channel estimate in the delay domain has only S non-zero entries. For a noisy channel, all the entries of the delay domain estimate are non-zero. However, among all N taps of the channel, only S entries contain power contributed from the channel. The rest $N-S$ taps have no channel power at all except for noise impairment. Hence, the elimination of these channel taps can improve the SNR. To establish a tractable analysis, we assume that the number of delay taps S is known at the receiver side. For practical wireless channels, the number of taps can be estimated via most significant tap detection [75, 76].

Due to the linearity of the Fourier transform, the IDFT to the channel frequency responses can be also applied to the subspace coefficients. Therefore, the delay domain coefficients can be written as [77]

$$[\tilde{\boldsymbol{\gamma}}^1, \ldots, \tilde{\boldsymbol{\gamma}}^S]^\mathrm{T} = \mathbf{D}^\mathrm{H}_{N\times S}[\tilde{\boldsymbol{\phi}}^1, \ldots, \tilde{\boldsymbol{\phi}}^N]^\mathrm{T}. \tag{3.24}$$

Only $\{\tilde{\gamma}^1, \ldots, \tilde{\gamma}^S\}$ are relevant for the actual channel realizations and must be fed back to the transmitters.

3.4.2 Reformulation of Subspace Representation for the SISO Interference Channels

With the basis coefficients $\{\tilde{\gamma}^1, \ldots, \tilde{\gamma}^S\}$ obtained from (3.24), the predicted channel impulse response can be calculated as

$$\begin{aligned}\tilde{\mathbf{h}}[m] &= [\tilde{\boldsymbol{\gamma}}^1, \ldots, \tilde{\boldsymbol{\gamma}}^S]^{\mathrm{T}} \mathbf{f}[m] \\ &= \mathbf{F}[m]\tilde{\boldsymbol{\eta}}\end{aligned} \tag{3.25}$$

where $\mathbf{F} \in \mathbb{C}^{S \times DS}$ and $\tilde{\boldsymbol{\eta}} \in \mathbb{C}^{DS \times 1}$ are defined as follows:

$$\mathbf{F}[m] = \mathrm{Bdiag}\left(\mathbf{f}[m]^{\mathrm{T}}, \ldots, \mathbf{f}[m]^{\mathrm{T}}\right) \tag{3.26}$$

and

$$\tilde{\boldsymbol{\eta}} = \begin{bmatrix} \tilde{\boldsymbol{\gamma}}^1 \\ \vdots \\ \tilde{\boldsymbol{\gamma}}^S \end{bmatrix}. \tag{3.27}$$

Note that the vector $\tilde{\boldsymbol{\eta}}$ is not unique since the achievable rate for IA is invariant to a norm change and phase rotation of $\tilde{\boldsymbol{\eta}}$ (this will be shown in Section 3.5). Therefore, it is equivalent to know $\tilde{\boldsymbol{\eta}}$ or $\alpha\tilde{\boldsymbol{\eta}}$ at the transmitter side, where $\alpha \in \mathbb{C}$. Thus, the CSI feedback problem becomes feeding back a point on the Grassmannian manifold $\mathcal{G}_{DS,1}$, which can be realized by vector quantization.

3.4.3 Vector Quantization and Feedback

After the subspace coefficient vector $\tilde{\boldsymbol{\eta}} \in \mathbb{C}^{DS \times 1}$ is obtained at the receiver side, the receiver quantizes the vector according to its codebook and broadcasts the index to the transmitter side through a feedback channel using N_{d} bits.

If the vector $\tilde{\boldsymbol{\eta}}$ has correlated entries, the design of the optimal codebook is difficult. In the special case with i.i.d entries, the optimal codebook for quantization can be generated numerically using the Grassmannian line-packing approach [78,79]. However, it is still challenging to find the optimal codewords which achieve the quantization bound promised by [80], except for some specific cases. To overcome this, random vector quantization (RVQ) codebooks are proposed. The codewords of $\mathcal{C}_{\mathrm{rnd}}$ are independent unit-norm vectors from the isotropic distribution on the complex unit sphere [60,81]. RVQ is commonly used to analyze the effects of quantization because it is mathematically tractable and asymptotically optimal with a distortion on the order of $2^{-\frac{N_\mathrm{d}}{DS-1}}$. Basic concepts of the Grassmannian manifold are summarized in Appendix 3.7.1.

When the vector to be quantized has correlated entires, a better codebook can be designed by skewing the RVQ codebook to match the correlation structure [82, 83]. The skewed codebook yields performance gain compared to the RVQ codebook. However, the exact characterization of the quantization error has remained an open question. A recent study in [84] tries to derive the SNR loss for single user MIMO beamforming system using skewed codebooks, but it still remains in terms of expectations of eigenvalues.

To overcome the difficulty in obtaining analytical results, we utilize a RVQ codebook, which will facilitate our analytical performance analysis in Section 3.5. Considering a factorization of the covariance matrix $\mathbf{R}_{\tilde{\boldsymbol{\eta}}} = \boldsymbol{\Lambda}\boldsymbol{\Lambda}^\mathrm{H}$, the vector $\tilde{\boldsymbol{\eta}}$ can be whiten as

$$\breve{\boldsymbol{\eta}} = \boldsymbol{\Lambda}^{-1}\tilde{\boldsymbol{\eta}}. \tag{3.28}$$

The covariance matrix $\mathbf{R}_{\tilde{\boldsymbol{\eta}}} = \mathrm{Bdiag}(\boldsymbol{\lambda}^1, \ldots, \boldsymbol{\lambda}^S)$ contains the covariance matrix of the subspace coefficients for each tap s, i.e.

$$\begin{aligned}
\boldsymbol{\lambda}^s &= \mathbb{E}\{\tilde{\boldsymbol{\gamma}}^s\tilde{\boldsymbol{\gamma}}^{s\mathrm{H}}\} && (3.29)\\
&= \mathbb{E}\{[\tilde{\boldsymbol{\phi}}^1, \ldots, \tilde{\boldsymbol{\phi}}^N]\mathbf{d}_s^*\mathbf{d}_s^\mathrm{T}[\tilde{\boldsymbol{\phi}}^1, \ldots, \tilde{\boldsymbol{\phi}}^N]^\mathrm{H}\} && (3.30)\\
&= \mathbf{G}^{-1}\mathbf{U}^{(\mathcal{P})^\mathrm{H}}\mathbb{E}\{[\mathbf{g}'^1, \ldots, \mathbf{g}'^N]\mathbf{d}_s^*\mathbf{d}_s^\mathrm{T}[\mathbf{g}'^1, \ldots, \mathbf{g}'^N]^\mathrm{H}\}\mathbf{U}^{(\mathcal{P})}\mathbf{G}^{-1} && (3.31)\\
&= \mathbf{G}^{-1}\mathbf{U}^{(\mathcal{P})^\mathrm{H}}\left(p^s\mathbf{R}_\mathbf{h}^{(\mathcal{P})} + \frac{1}{P}\mathbf{I}_{\frac{M}{K}}\right)\mathbf{U}^{(\mathcal{P})}\mathbf{G}^{-1}. && (3.32)
\end{aligned}$$

where $\mathbf{d}_s$ is the s-th column of the DFT matrix $\mathbf{D}_{N\times S}$. The equations (3.30), (3.31) and (3.32) are due to (3.24), (3.17) and (3.3), respectively.

We do not assume exact knowledge of the PDP in our work, instead a flat PDP assumption

$$\mathbb{E}\{\mathbf{h}[m]\mathbf{h}[m]^\mathrm{H}\} = \mathrm{diag}\big([p^1, \ldots, p^S]\big) = \frac{N}{S}\mathbf{I}_S \tag{3.33}$$

is used. In case the assumed PDP matches the PDP of the true channel, the vector $\breve{\boldsymbol{\eta}}$ will be isotropically distributed with uncorrelated entries.

The corresponding RVQ codebook $\mathcal{C}_\mathrm{rnd}$ contains 2^{N_d} unit-norm vectors, i.e. $\mathcal{C}_\mathrm{rnd} = \{\hat{\boldsymbol{\eta}}_1, \ldots, \hat{\boldsymbol{\eta}}_{2^{N_\mathrm{d}}}\}$. Using codebook $\mathcal{C}_\mathrm{rnd}$, the quantized version of $\tilde{\boldsymbol{\eta}}$ can be obtained as

$$\hat{\boldsymbol{\eta}} = \underset{\hat{\boldsymbol{\eta}}_i\in\mathcal{C}_\mathrm{rnd}}{\arg\max}|\hat{\boldsymbol{\eta}}_i^\mathrm{H}\breve{\boldsymbol{\eta}}|. \tag{3.34}$$

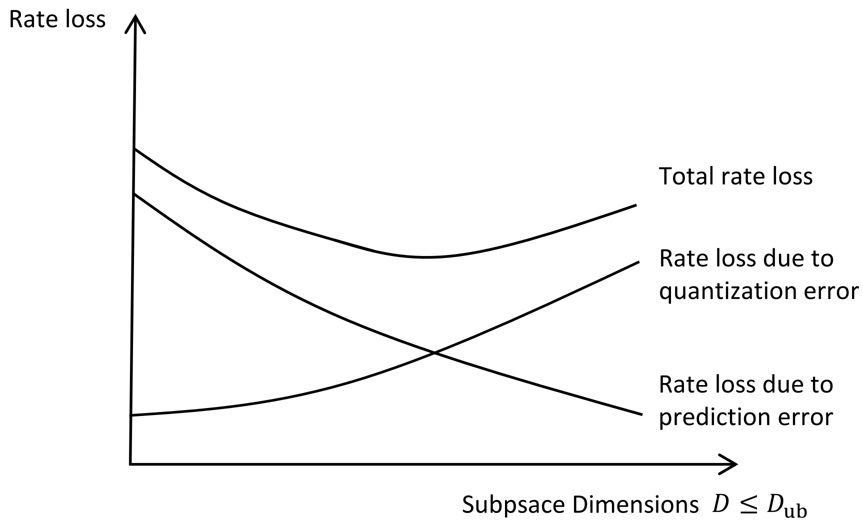

Figure 3.2: Rate loss due to prediction error and quantization error as a function of the subspace dimension D.

After receiving the feedback information, the transmitters can reconstruct the quantized vector by adding the correlation $\mathbf{\Lambda}\hat{\boldsymbol{\eta}}$.

3.5 Rate Loss Analysis

In this section, we analyze the rate loss of our proposed scheme. We decouple the channel prediction- and quantization-error and derive an upper bound of the rate loss. We show that a smaller subspace dimension is favorable for quantization due to less coefficients. On the other hand, more subspace coefficients will reduce the prediction error for the case of $\mathcal{D}_{\mathrm{ub}} > 1$. Therefore, there exists a tradeoff between quantization error and prediction error when selecting the subspace dimension at a given feedback rate. On a coarse level, the tradeoff is illustrated in Fig. 3.2 in terms of sum rate loss. We develop a subspace dimension switching algorithm to find the best tradeoff such that the rate loss upper bound is minimized. We also characterize the scaling of the required number of feedback bits in order to decouple the rate loss due to imperfect quantization from the transmit power.

3.5.1 Leakage Interference Due to Imperfect CSI

Imperfect CSI results in residual interference, thus, IA conditions (3.9) and (3.10) can not be satisfied. Upon reception of the quantized subspace vector $\hat{\boldsymbol{\eta}}$, the quantized channel $\hat{\mathbf{h}}[m]$ can be constructed in the same way as (3.25). The precoding vector $\hat{\mathbf{v}}_k^i[m]$ and decoding vector $\hat{\mathbf{u}}_k^i[m]$ are calculated using $\hat{\mathbf{w}}_{k,\ell}[m] = \mathbf{D}_{N\times S}\hat{\mathbf{h}}_{k,\ell}[m]$ as the true channel, which results in

$$\hat{\mathbf{u}}_k^i[m]^{\mathrm{H}}\hat{\mathbf{W}}_{k,k}[m]\hat{\mathbf{v}}_k^j[m] = 0, \quad \forall k,\ \forall i \neq j \tag{3.35}$$

$$\hat{\mathbf{u}}_k^i[m]^{\mathrm{H}}\hat{\mathbf{W}}_{k,\ell}[m]\hat{\mathbf{v}}_\ell^j[m] = 0, \quad \forall k \neq \ell,\ \forall i,\ j \tag{3.36}$$

$$\left|\hat{\mathbf{u}}_k^i[m]^{\mathrm{H}}\hat{\mathbf{W}}_{k,k}[m]\hat{\mathbf{v}}_k^i[m]\right| \geq c > 0, \quad \forall k,\ i\,. \tag{3.37}$$

We modify the upper bound for the average loss in sum rate [61] for a time-variant channel as

$$\Delta R < \frac{1}{NT}\sum_{k,i}\sum_{m\in\mathcal{T}} \log_2\left(1 + \mathbb{E}\left[\mathcal{I}_{k,i}^1[m] + \mathcal{I}_{k,i}^2[m]\right]\right). \tag{3.38}$$

We define $\hat{\mathbf{b}}_{k,\ell}^{i,j}[m] = \hat{\mathbf{u}}_k^i[m]^* \circ \hat{\mathbf{v}}_\ell^j[m]$ as the Hadamard product of the decoding vector $\hat{\mathbf{u}}_k^i[m]$ and precoding vector $\hat{\mathbf{v}}_\ell^j[m]$. The leakage interference in (3.7) and (3.8) can be rewritten as

$$\mathcal{I}_{k,i}^1[m] = \sum_{i\neq j}\frac{NP}{d_k}\left|\mathbf{w}_{k,k}[m]^{\mathrm{T}}\hat{\mathbf{b}}_{k,k}^{i,j}[m]\right|^2, \text{ and} \tag{3.39}$$

$$\mathcal{I}_{k,i}^2[m] = \sum_{k\neq\ell}\sum_{j=1}^{d_\ell}\frac{NP}{d_\ell}\left|\mathbf{w}_{k,\ell}[m]^{\mathrm{T}}\hat{\mathbf{b}}_{k,\ell}^{i,j}[m]\right|^2. \tag{3.40}$$

We define the predicted channel frequency response as

$$\tilde{\mathbf{w}}_{k,\ell}[m] = [\tilde{w}_{k,\ell}^1[m], \ldots, \tilde{w}_{k,\ell}^n[m]]^{\mathrm{T}} \tag{3.41}$$

and the prediction error as $\tilde{\mathbf{z}}_{k,\ell}[m] = \mathbf{w}_{k,\ell}[m] - \tilde{\mathbf{w}}_{k,\ell}[m]$. The average power leakage of the inter-stream interference in (3.39) can be upper bounded by

$$\begin{aligned}
\mathbb{E}\left[\mathcal{I}_{k,i}^{1}[m]\right] &= \sum_{i\neq j}\frac{NP}{d_k}\mathbb{E}\left[\left|\mathbf{w}_{k,k}[m]^{\mathrm{T}}\hat{\mathbf{b}}_{k,k}^{i,j}[m]\right|^2\right] && (3.42)\\
&= \sum_{i\neq j}\frac{NP}{d_k}\mathbb{E}\left[\left|\left(\tilde{\mathbf{w}}_{k,k}[m]^{\mathrm{T}}+\tilde{\mathbf{z}}_{k,k}[m]^{\mathrm{T}}\right)\hat{\mathbf{b}}_{k,k}^{i,j}[m]\right|^2\right] && (3.43)\\
&= \sum_{i\neq j}\frac{NP}{d_k}\Bigg(\mathbb{E}\Bigg[\left|\tilde{\mathbf{w}}_{k,k}[m]^{\mathrm{T}}\hat{\mathbf{b}}_{k,k}^{i,j}[m]\right|^2+\left|\tilde{\mathbf{z}}_{k,k}[m]^{\mathrm{T}}\hat{\mathbf{b}}_{k,k}^{i,j}[m]\right|^2\\
&\quad+2\mathrm{Re}\left(\tilde{\mathbf{w}}_{k,k}[m]^{\mathrm{T}}\hat{\mathbf{b}}_{k,k}^{i,j}[m]\hat{\mathbf{b}}_{k,k}^{i,j}[m]^{\mathrm{H}}\tilde{\mathbf{z}}_{k,k}[m]^{*}\right)\Bigg]\Bigg) && (3.44)\\
&\approx \sum_{i\neq j}\Bigg(\underbrace{\frac{NP}{d_k}\mathbb{E}\left[\left|\tilde{\mathbf{z}}_{k,k}[m]^{\mathrm{T}}\hat{\mathbf{b}}_{k,k}^{i,j}[m]\right|^2\right]}_{\tilde{I}_{k,k}^{i,j}[m]}+\underbrace{\frac{NP}{d_k}\mathbb{E}\left[\left|\tilde{\mathbf{w}}_{k,k}[m]^{\mathrm{T}}\hat{\mathbf{b}}_{k,k}^{i,j}[m]\right|^2\right]}_{\hat{I}_{k,k}^{i,j}[m]}\Bigg) && (3.45)
\end{aligned}$$

where (3.45) is obtained by ignoring the term $\mathbb{E}\left[\mathrm{Re}\left(\tilde{\mathbf{w}}_{k,\ell}[m]^{\mathrm{H}}\hat{\mathbf{b}}_{k,\ell}^{i,j}[m]\hat{\mathbf{b}}_{k,\ell}^{i,j}[m]^{\mathrm{H}}\tilde{\mathbf{z}}_{k,\ell}[m]\right)\right]$. An equality holds from (3.44) to (3.45) with the MMSE predictor (3.32), where $\tilde{\mathbf{z}}_{k,\ell}[m]$ is zero-mean Gaussian and independent of $\tilde{\mathbf{w}}_{k,\ell}[m]$. However, for our reduced-rank predictor, we notice that an exact characterization of this term $\mathbb{E}\left[\mathrm{Re}\left(\tilde{\mathbf{w}}_{k,\ell}[m]^{\mathrm{H}}\hat{\mathbf{b}}_{k,\ell}^{i,j}[m]\hat{\mathbf{b}}_{k,\ell}^{i,j}[m]^{\mathrm{H}}\tilde{\mathbf{z}}_{k,\ell}[m]\right)\right]$ is mathematically intractable. As discussed in Remark 1, the reduced-rank predictor is closely related to the MMSE predictor. We also found via simulation that this term is rather small. Similar to (3.45), the inter-user interference term in (3.40) can be upper bounded by

$$\mathbb{E}\left[\mathcal{I}_{k,i}^{2}[m]\right] \approx \sum_{k\neq\ell}\sum_{j=1}^{d_\ell}\Bigg(\underbrace{\frac{NP}{d_\ell}\mathbb{E}\left[\left|\tilde{\mathbf{z}}_{k,\ell}[m]^{\mathrm{T}}\hat{\mathbf{b}}_{k,\ell}^{i,j}[m]\right|^2\right]}_{\tilde{I}_{k,\ell}^{i,j}[m]}+\underbrace{\frac{NP}{d_\ell}\mathbb{E}\left[\left|\tilde{\mathbf{w}}_{k,\ell}[m]^{\mathrm{T}}\hat{\mathbf{b}}_{k,\ell}^{i,j}[m]\right|^2\right]}_{\hat{I}_{k,\ell}^{i,j}[m]}\Bigg). \tag{3.46}$$

In the following Sections 3.5.2 and 3.5.3, we will show that the first and second terms in (3.45) and (3.46) are caused by the channel prediction error and the quantization error, respectively.

3.5.2 Leakage Interference Due to Channel Prediction Error

Defining $[\hat{\mathbf{q}}_{k,k}^{i,j}[m]^{\mathrm{T}},\mathbf{q}_{k,k}^{i,j}[m]^{\mathrm{T}}]^{\mathrm{T}}=\mathbf{D}_N^{\mathrm{H}}\hat{\mathbf{b}}_{k,k}^{i,j}[m]^{*}$, where $\hat{\mathbf{q}}_{k,k}^{i,j}[m]\in\mathbb{C}^{S\times 1}$ and $\mathbf{q}_{k,k}^{i,j}[m]\in\mathbb{C}^{(N-S)\times 1}$, and $[\tilde{\mathbf{e}}_{xk,k}[m]^{\mathrm{T}},\mathbf{0}_{1\times(N-S)}]^{\mathrm{T}}=\mathbf{D}_N^{\mathrm{H}}\tilde{\mathbf{z}}_{k,k}[m]$, the first term of the inter-stream interference $\tilde{I}^{i,j}_{k,k}[m]$ in (3.45) can be written as

$$\begin{aligned}
\tilde{I}^{i,j}_{k,k}[m] =& \frac{NP}{d_k}\mathbb{E}\left[\left|\tilde{\mathbf{z}}_{k,k}[m]^{\mathrm{T}}\hat{\mathbf{b}}^{i,j}_{k,k}[m]\right|^2\right] \\
=& \frac{NP}{d_k}\mathbb{E}\left[\left|\tilde{\mathbf{e}}_{k,k}[m]^{\mathrm{H}}\hat{\mathbf{q}}^{i,j}_{k,k}[m]\right|^2\right] && (3.47) \\
\approx& \frac{NP}{d_k}\mathbb{E}\left[\hat{\mathbf{q}}^{i,j}_{k,k}[m]^{\mathrm{H}}\mathbb{E}\left[\tilde{\mathbf{e}}_{k,k}[m]\tilde{\mathbf{e}}_{k,k}[m]^{\mathrm{H}}\right]\hat{\mathbf{q}}^{i,j}_{k,k}[m]\right] && (3.48) \\
=& \frac{N^2P}{Sd_k}\mathbb{E}\left\|\hat{\mathbf{q}}^{i,j}_{k,k}[m]\right\|^2 \cdot \mathrm{MSE}\left[m, D, \frac{NP}{S}\right] && (3.49) \\
=& \tilde{J}^{i,j}_{k,k}[m]
\end{aligned}$$

where (3.47) is due to Parseval's theorem. In order for tractable results, we arrive at (3.48) by assuming the independence of $\hat{\mathbf{q}}^{i,j}_{k,\ell}[m]$ and $\tilde{\mathbf{e}}_{k,\ell}[m]$, which is the case for the MMSE predictor ($\hat{\mathbf{q}}^{i,j}_{k,\ell}[m]$ is a function of $\hat{\mathbf{h}}_{k,\ell}[m]$ and therefore $\tilde{\mathbf{h}}_{k,\ell}[m]$. The prediction error $\tilde{\mathbf{e}}_{k,\ell}[m]$ is independent of $\tilde{\mathbf{h}}_{k,\ell}[m]$). For our reduced-rank predictor, it still provides a good approximation due to the close relation between a reduced-rank predictor and the MMSE predictor (see discussion in Remark 1). Equation (3.49) follows from $\mathbb{E}\left[\tilde{\mathbf{e}}_{k,k}[m]\tilde{\mathbf{e}}_{k,k}[m]^{\mathrm{H}}\right] = \frac{\mathbb{E}\|\tilde{\mathbf{e}}_{k,k}[m]\|^2}{S}\mathbf{I}_S$, where $\|\tilde{\mathbf{e}}_{k,k}[m]\|^2 = \|\tilde{\mathbf{z}}_{k,k}[m]\|^2$. The MSE per subchannel $\mathbb{E}\left[|\tilde{z}_{k,k}[m,n]|^2\right]$, $\forall n \in \{1, \ldots, N\}$, is the sum of a square bias and a variance term [66] $\mathrm{MSE}[m, D, \mathrm{SNR}] = \mathrm{bias}^2[m, D] + \mathrm{var}[m, D, \mathrm{SNR}]$ where the variance can be approximated by

$$\mathrm{var}[m, D, \mathrm{SNR}] = \frac{\mathbf{f}[m]^{\mathrm{T}}\mathbf{G}^{-1}\mathbf{f}[m]}{\mathrm{SNR}}. \tag{3.50}$$

The square bias term is calculated as [66]

$$\mathrm{bias}^2[m, D] = \int_{-\frac{1}{2}}^{\frac{1}{2}} \left|1 - \mathbf{f}[m]^{\mathrm{T}}\mathbf{G}^{-1}\sum_{\ell\in\mathcal{P}}\mathbf{f}[\ell]e^{-j2\pi\nu(m-\ell)}\right|^2 S_h(\nu)\mathrm{d}\nu \tag{3.51}$$

where $S_h(\nu)$ denotes the actual power spectral density of the fading process. Due to the removal of the noise terms in (3.24), the noise variance is reduced by a factor of N/S, therefore resulting in an SNR of $\frac{NP}{S}$ in equation (3.49).

A similar result can be obtained for the first term of the inter-user interference in (3.46), i.e.

$$\tilde{I}^{i,j}_{k,\ell}[m] \approx \tilde{J}^{i,j}_{k,\ell}[m] = \frac{N^2P}{Sd_\ell}\mathbb{E}\left\|\hat{\mathbf{q}}^{i,j}_{k,\ell}[m]\right\|^2 \mathrm{MSE}\left[m, D, \frac{NP}{S}\right]. \tag{3.52}$$

3.5.3 Leakage Interference Due to Channel Quantization Error

To obtain tractable expressions, we restrict the subsequent analysis to a flat PDP, such that the vector to be quantized $\breve{\boldsymbol{\eta}}_{k,k}$ is isotropically distributed with uncorrelated entires. The interference leakage caused by the quantization error $\hat{I}^{i,j}_{k,k}[m]$ in (3.45) can be rewritten as

$$\begin{aligned}\hat{I}^{i,j}_{k,k}[m] =& \frac{NP}{d_k}\mathbb{E}\left[\left|\tilde{\mathbf{w}}_{k,k}[m]^{\mathrm{T}}\hat{\mathbf{b}}^{i,j}_{k,k}[m]\right|^2\right] \\ =& \frac{NP}{d_k}\mathbb{E}\left[\left|\tilde{\mathbf{h}}_{k,k}[m]^{\mathrm{H}}\hat{\mathbf{q}}^{i,j}_{k,k}[m]\right|^2\right] \qquad (3.53)\\ =& \frac{NP}{d_k}\mathbb{E}\left[\left|\hat{\mathbf{q}}^{i,j}_{k,k}[m]^{\mathrm{H}}\mathbf{F}_{k,k}[m]\boldsymbol{\Lambda}_{k,k}\breve{\boldsymbol{\eta}}_{k,k}\right|^2\right]. \qquad (3.54)\end{aligned}$$

Since $\hat{\boldsymbol{\eta}}_{k,k}$ is the quantized version of $\breve{\boldsymbol{\eta}}_{k,k}$ and $\left\|\hat{\boldsymbol{\eta}}_{k,k}\right\| = 1$, from Parseval's theorem we have $\hat{\mathbf{q}}^{i,j}_{k,k}[m]^{\mathrm{H}}\mathbf{F}_{k,k}[m]\boldsymbol{\Lambda}_{k,k}\hat{\boldsymbol{\eta}}_{k,k} = 0$. We can define an orthonormal basis in $\mathbb{C}^{DS}$ as

$$\left\{\hat{\boldsymbol{\eta}}_{k,k}, \frac{\boldsymbol{\Lambda}_{k,k}\mathbf{F}_{k,k}[m]^{\mathrm{H}}\hat{\mathbf{q}}^{i,j}_{k,k}[m]}{\left\|\boldsymbol{\Lambda}_{k,k}\mathbf{F}_{k,k}[m]^{\mathrm{H}}\hat{\mathbf{a}}^{i,j}_{k,k}[m]\right\|}, \mathbf{a}_1, \mathbf{a}_2, \ldots, \mathbf{a}_{DS-2}\right\}, \qquad (3.55)$$

where $[\mathbf{a}_1, \mathbf{a}_2, \ldots, \mathbf{a}_{DS-2}]$ is an orthonormal basis of $\mathrm{null}\left(\left[\hat{\boldsymbol{\eta}}_{k,k}, \frac{\boldsymbol{\Lambda}_{k,k}\mathbf{F}_{k,k}[m]^{\mathrm{H}}\hat{\mathbf{q}}^{i,j}_{k,k}[m]}{\left\|\boldsymbol{\Lambda}_{k,k}\mathbf{F}_{k,k}[m]^{\mathrm{H}}\hat{\mathbf{q}}^{i,j}_{k,k}[m]\right\|}\right]^{\mathrm{H}}\right)$. We can decompose $\breve{\boldsymbol{\eta}}_{k,k}$ into the above orthonormal basis, i.e.

$$\left\|\breve{\boldsymbol{\eta}}_{k,k}\right\|^2 = \left|\hat{\boldsymbol{\eta}}^{\mathrm{H}}_{k,k}\breve{\boldsymbol{\eta}}_{k,k}\right|^2 + \left|\frac{\hat{\mathbf{q}}^{i,j}_{k,k}[m]^{\mathrm{H}}\mathbf{F}_{k,k}[m]\boldsymbol{\Lambda}_{k,k}}{\left\|\hat{\mathbf{q}}^{i,j}_{k,k}[m]^{\mathrm{H}}\mathbf{F}_{k,k}[m]\boldsymbol{\Lambda}_{k,k}\right\|}\breve{\boldsymbol{\eta}}_{k,k}\right|^2 + \sum_{m=1}^{DS-2}\left|\mathbf{a}^{\mathrm{H}}_m\breve{\boldsymbol{\eta}}_{k,k}\right|^2.$$

Inserting (3.56) into (3.54) yields

$$\begin{aligned}&\frac{NP}{d_k}\mathbb{E}\left[\left|\hat{\mathbf{q}}^{i,j}_{k,k}[m]^{\mathrm{H}}\mathbf{F}_{k,k}[m]\boldsymbol{\Lambda}_{k,k}\breve{\boldsymbol{\eta}}_{k,k}\right|^2\right] \qquad (3.56)\\ &= \frac{NP}{d_k}\mathbb{E}\left[\left\|\hat{\mathbf{q}}^{i,j}_{k,k}[m]^{\mathrm{H}}\mathbf{F}_{k,k}[m]\boldsymbol{\Lambda}_{k,k}\right\|^2\left(\left\|\breve{\boldsymbol{\eta}}_{k,k}\right\|^2 - |\hat{\boldsymbol{\eta}}^{\mathrm{H}}_{k,k}\breve{\boldsymbol{\eta}}_{k,k}|^2 - \sum_{m=1}^{DS-2}\left|\mathbf{d}^{\mathrm{H}}_m\breve{\boldsymbol{\eta}}_{k,k}\right|^2\right)\right] \qquad (3.57)\\ &= \frac{NP}{d_k(DS-1)}\mathbb{E}\left\|\hat{\mathbf{q}}^{i,j}_{k,k}[m]^{\mathrm{H}}\mathbf{F}_{k,k}[m]\boldsymbol{\Lambda}_{k,k}\right\|^2\mathbb{E}\left[\left\|\breve{\boldsymbol{\eta}}_{k,k}\right\|^2 - |\hat{\boldsymbol{\eta}}^{\mathrm{H}}_{k,k}\breve{\boldsymbol{\eta}}_{k,k}|^2\right] \qquad (3.58)\\ &= \frac{NP}{d_k(DS-1)}\mathbb{E}\left\|\hat{\mathbf{q}}^{i,j}_{k,k}[m]^{\mathrm{H}}\mathbf{F}_{k,k}[m]\boldsymbol{\Lambda}_{k,k}\right\|^2\mathbb{E}\left\|\breve{\boldsymbol{\eta}}_{k,k}\right\|^2\mathbb{E}\left[d^2_{\mathrm{c}}\left(\frac{\breve{\boldsymbol{\eta}}_{k,k}}{\left\|\breve{\boldsymbol{\eta}}_{k,k}\right\|}, \hat{\boldsymbol{\eta}}_{k,k}\right)\right] \qquad (3.59)\end{aligned}$$

where $d_{\mathrm{c}}(\mathbf{x}_1, \mathbf{x}_2) = \sqrt{(1 - |\mathbf{x}_1^{\mathrm{H}}\mathbf{x}_2|^2)}$ is the chordal distance between two unit norm vectors $\mathbf{x}_1$ and $\mathbf{x}_2$. Equation (3.58) follows from the fact that the quantization error is isotropic in the nullspace of $\hat{\boldsymbol{\eta}}_{k,k}$ and therefore the average power of $\breve{\boldsymbol{\eta}}_{k,k}$ in each dimension of $\left\{\frac{\boldsymbol{\Lambda}_{k,k}\mathbf{F}_{k,k}[m]^{\mathrm{H}}\hat{\mathbf{q}}_{k,k}^{i,j}[m]}{\left\|\boldsymbol{\Lambda}_{k,k}\mathbf{F}_{k,k}[m]^{\mathrm{H}}\hat{\mathbf{q}}_{k,k}^{i,j}[m]\right\|}, \mathbf{d}_1, \mathbf{d}_2, \ldots, \mathbf{d}_{DS-2}\right\}$ is equal. Equation (3.59) follows from the independence of the norm and the angle of $\breve{\boldsymbol{\eta}}_{k,k}$.

Equation (3.59) shows that the leakage interference can be bounded by the chordal distance between the true and the quantized subspace coefficients. The term $Q(N_{\mathrm{d}}) = \mathbb{E}\left[d_{\mathrm{c}}^2\left(\frac{\breve{\boldsymbol{\eta}}_{k,\ell}}{\|\breve{\boldsymbol{\eta}}_{k,\ell}\|}, \hat{\boldsymbol{\eta}}_{k,\ell}\right)\right]$ in (3.59) is the expectation of the quantization error. As shown in [80], for quantizing a vector arbitrarily distributed on the Grassmannian manifold $\mathcal{G}_{DS,1}$ using RVQ, the second moment of the chordal distance using N_{d} quantization bits can be bounded as

$$Q(N_{\mathrm{d}}) \leq \frac{\Gamma(\frac{1}{DS-1})}{DS-1}(c2^{N_{\mathrm{d}}})^{-\frac{1}{DS-1}}, \tag{3.60}$$

where $\Gamma(\cdot)$ denotes the Gamma function.

Furthermore, we have

$$\begin{aligned}\left\|\hat{\mathbf{q}}_{k,k}^{i,j}[m]^{\mathrm{H}}\mathbf{F}_{k,k}[m]\boldsymbol{\Lambda}_{k,k}\right\|^2 &= \sum_{s=1}^{S}\left\|\hat{\mathbf{q}}_{k,k}^{i,j}[m,s]\boldsymbol{\lambda}_{k,k}\mathbf{f}_{k,k}[m]\right\|^2 \\ &= \left\|\hat{\mathbf{q}}_{k,k}^{i,j}[m]\right\|^2\|\boldsymbol{\lambda}_{k,k}\mathbf{f}_{k,k}[m]\|^2\end{aligned} \tag{3.61}$$

and

$$\mathbb{E}\|\tilde{\boldsymbol{\eta}}_{k,k}\|^2 = DS, \tag{3.62}$$

according to Appendix 3.7.2. Plugging the above results into (3.59), the inter-stream interference leakage caused by quantization error $\hat{I}_{k,k}^{i,j}[m]$ can be finally bounded by

$$\begin{aligned}\hat{I}_{k,k}^{i,j}[m] \leq& \hat{J}_{k,k}^{i,j}[m] \\ =& \frac{NPDS}{d_k(DS-1)}\mathbb{E}\left\|\hat{\mathbf{q}}_{k,k}^{i,j}[m]\right\|^2\|\boldsymbol{\lambda}_{k,k}\mathbf{f}_{k,k}[m]\|^2 Q(N_{\mathrm{d}}).\end{aligned} \tag{3.63}$$

Accordingly, the inter-user interference can be bounded as

$$\begin{aligned}\hat{I}_{k,\ell}^{i,j}[m] \leq& \hat{J}_{k,\ell}^{i,j}[m] \\ =& \frac{NPDS}{d_\ell(DS-1)}\mathbb{E}\left\|\hat{\mathbf{q}}_{k,\ell}^{i,j}[m]\right\|^2\|\boldsymbol{\lambda}_{k,\ell}\mathbf{f}_{k,\ell}[m]\|^2 Q(N_{\mathrm{d}}).\end{aligned} \tag{3.64}$$

The only stochastic part in the equation is $\left\|\hat{\mathbf{q}}_{k,\ell}^{i,j}[m]\right\|^2$, whose value relies on the applied IA algorithm.

$$\Delta R_{\mathrm{ub}} < \frac{1}{NT}\sum_{k}\sum_{m\in\mathcal{T}} d_k \log_2\left(1+NP\left(K-\frac{1}{d_k}\right)\mathrm{MSE}\left[m,D\right]\right)+ \\ \frac{1}{NT}\sum_{k}\sum_{m\in\mathcal{T}} d_k \log_2\left(1+NP\left(K-\frac{1}{d_k}\right)\left(DN-\frac{\zeta(N-S)}{P}\right)\rho[m]Q(N_{\mathrm{d}})\right) \tag{3.67}$$

Theorem 1. When the proposed prediction and limited feedback strategy is used for IA CSI feedback, the average rate loss due to channel prediction and quantization can be upper bound by

$$\Delta R \lesssim \Delta R_{\mathrm{ub}} = \frac{1}{NT}\sum_{k}\sum_{m\in\mathcal{T}} d_k \log_2\Bigg(1+NP\left(K-\frac{1}{d_k}\right)\cdot \\ \left(\frac{N}{S}\mathrm{MSE}\left[m,D,\frac{NP}{S}\right]+\frac{DS\zeta[m]Q(N_{\mathrm{d}})}{DS-1}\right)\Bigg), \tag{3.65}$$

where $\zeta[m] = \|\boldsymbol{\lambda}_{k,\ell}\mathbf{f}_{k,\ell}[m]\|^2$.

Proof. Equation (3.65) is obtained by inserting (3.49), (3.52), (3.63) and (3.64) into (3.38) and using the fact $\left\|\hat{\mathbf{q}}_{k,\ell}^{i,j}[m]\right\|^2 < 1, \forall(i,k,j,\ell)$. This can be shown as $\left\|\hat{\mathbf{q}}_{k,\ell}^{i,j}[m]\right\|^2 \leq \left\|\hat{\mathbf{b}}_{k,\ell}^{i,j}[m]\right\|^2 = \sum_{n=1}^{N}\left|\hat{u}_k^k[m,n]\right|^2\left|\hat{v}_\ell^\ell[m,n]\right|^2 < \sum_{n=1}^{N}\left|\hat{u}_k^k[m,n]\right|^2\sum_{n=1}^{N}\left|\hat{v}_\ell^\ell[m,n]\right|^2 = 1$. □

Remark 2. We notice that the rate loss upper bound (3.65) derived using the method [61] is known to be loose especially when CSI quality is poor, mainly due to the use of Jensen's inequality. Besides, we use the fact $\left\|\hat{\mathbf{q}}_{k,\ell}^{i,j}[m]\right\|^2 < 1$, which further loosens the bound. However, the term $\left\|\hat{\mathbf{q}}_{k,\ell}^{i,j}[m]\right\|^2$ exists in both the prediction and quantization errors, thus using this inequality is not critical for the purpose of deriving a subspace switching algorithm in Section 3.5.4, especially at high SNRs.

Theorem 2. The sum rate loss due to the quantization error can be bounded by a finite value when $P \longrightarrow \infty$, if the number of feedback bits per receiver grows as

$$N_{\mathrm{d}} = (DS-1)\log_2 P. \tag{3.66}$$

Proof. The mean rate loss can be decomposed into the following two terms in (3.67) due to $\log(1+A+B) < \log(1+A)+\log(1+B)$ if $A, B > 0$. The first term and second term of (3.67) are caused by estimation (prediction) error and quantization error, respectively. If the number of feedback bits per channel is $N_\mathrm{d} = (DS - 1)\log_2 P$, the interference power due to quantization error $\hat{J}^{i,j}_{k,k}[m]$ and $\hat{J}^{i,j}_{k,\ell}[m]$ can be upper bounded by a finite value independent of P. Accordingly, the rate loss due to quantization error is also upper bounded. □

3.5.4 Adaptive Subspace Dimension Switching Algorithm

When the subspace coefficients are unquantized, the optimal subspace dimension that minimizes the prediction error is given by (3.22). However, for $\mathcal{D}_\mathrm{ub} > 1$, a subspace dimension higher than one is favorable for channel prediction, while resulting in a higher quantization error. Hence, a limited feedback system exhibits a tradeoff between the quality of channel prediction and quantization. The selection of the subspace dimension to find the best tradeoff becomes more relevant and thus, a selection metric is needed for this purpose. The rate loss upper bound developed in (3.65) is suitable. We propose an *adaptive subspace dimension switching* algorithm, which finds the subspace dimension minimizing (3.65), i.e.

$$\mathcal{D} = \underset{D\in\{1,\ldots,\mathcal{D}_\mathrm{ub}\}}{\arg\min}\ \Delta R_\mathrm{ub}. \tag{3.68}$$

3.6 Simulations

In this section, the sum rate of the proposed scheme is evaluated through Monte-Carlo (MC) simulations. For the IA design in this section, we use the closed-form IA algorithm [11] over $N = 5$ channel extensions with an additional precoding subspace optimization [85], since it has been shown that the original closed-from IA solution [11] yields low rate if no further optimization is performed [44, 85]. We consider a $K = 3$ user interference channel, where each channel has S delay taps and a flat PDP $\mathbb{E}\{\mathbf{h}_{k,\ell}[m]\mathbf{h}_{k,\ell}[m]^\mathrm{H}\} = \frac{N}{S}\mathbf{I}_S$. Each delay tap $h_{k,\ell}[m,s]$ is temporally correlated according to Clarke's model [86] with $R_{\mathbf{h}_{k,\ell}}[m] = J_0(2\pi\nu_\mathrm{D} m)$, where J_0 is the 0-th order Bessel function of the first kind. The OFDM symbol rate $1/T_s = 1.4\times 10^4$Hz is chosen according to the 3GPP LTE standard [87]. The carrier frequency $f_c = 2.5$GHz. In order to enable the performance analysis with exponentially large codebooks, we replace the RVQ process by the statistical model of the quantization error using random perturbations [88, Section VI.B], which has been shown to be a good approximation of the quantization error using RVQ.

3.6.1 Validation of The Rate Analysis

First, we examine the effect of imperfect channel prediction and quantization. Fig. 3.3 shows the power of leakage interference (for a specific (k, ℓ) and (i, j)) versus the evolution of time for $\nu_{\mathrm{D}} = 0.001$ (6.05 km/h). The leakage powers due to prediction error and quantization error are shown respectively for MC simulations of $\tilde{I}^{i,j}_{k,\ell}[m]$ and $\hat{I}^{i,j}_{k,\ell}[m]$, and for the analytical upper bound $\tilde{J}^{i,j}_{k,\ell}[m]$ and $\hat{J}^{i,j}_{k,\ell}[m]$. Note that there still exists a stochastic part $\mathbb{E}\left\|\hat{\mathbf{q}}^{i,j}_{k,\ell}[m]\right\|^2$ in $\hat{J}^{i,j}_{k,\ell}[m]$ and $\tilde{J}^{i,j}_{k,\ell}[m]$. However, as explained in Remark 2, using the upper bound $\left\|\hat{\mathbf{q}}^{i,j}_{k,\ell}[m]\right\|^2 < 1$ has only a minor impact on the subspace switching algorithm, and thus the deterministic part of $\hat{J}^{i,j}_{k,\ell}[m]$ and $\tilde{J}^{i,j}_{k,\ell}[m]$ are more relevant. Therefore, we take an empirical value of $\mathbb{E}\left\|\hat{\mathbf{q}}^{i,j}_{k,\ell}[m]\right\|^2$ from the simulation in order to make the comparison with the true leakage power. We can observe that the leakage due to the prediction error increases over time due to increased MSE. The leakage due to the quantization error is almost a constant throughout the frame. In addition, the results corresponding to MC simulation and the analytical upper bound are quite close. The sum of both leakage terms is slightly higher than the true interference leakage power due to the ignorance of the last term in (3.44). Note that the interference leakage with non-flat PDPs (not shown) is similar to the one with flat PDP and matches well with the analytical bound as well.

3.6.2 Choice of Subspace Dimension

Fig. 3.4 shows contour lines of the subspace dimension obtained according to (3.68) as a function of SNR and the number of feedback bits. It can be seen that a higher subspace dimension is suggested when both SNR and the number of feedback bits are high. This is because higher SNR allows for high subspace dimension for channel prediction due to the relatively small variance of a reduced-rank predictor. This will also result in more subspace coefficients, which in turn require more bits for feedback to maintain a low quantization error. In case of a low feedback rate, a lower subspace dimension is still favorable in order for a low quantization error, and therefore the best tradeoff between prediction and quantization.

Fig. 3.5 illustrates the sum rate using the same setup as in Fig. 3.4, with subspace dimension $D \in \{1, 2, 3\}$, respectively. It can be seen that the dimension suggested in Fig. 3.4 matches well with the dimension that achieves a higher rate.

Fig. 3.6 shows the sum rate versus the number of feedback bits at an SNR=30dB and the normalized Doppler frequency $\nu_D = 0.004$ (24.2km/h). The lower bound of

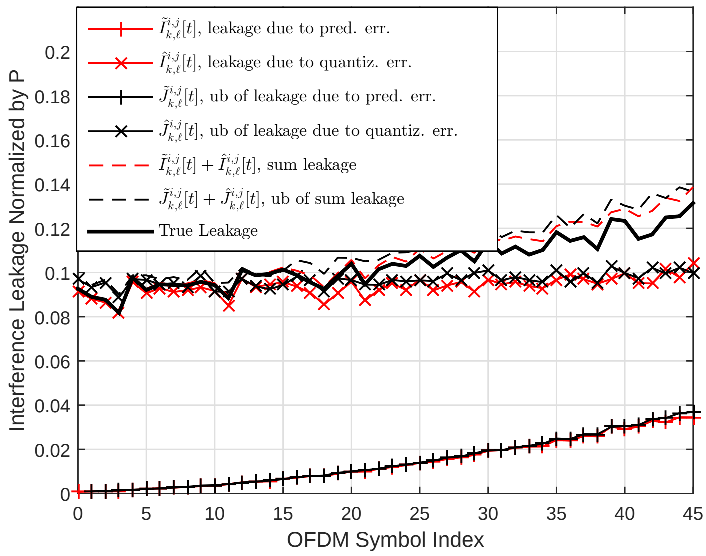

Figure 3.3: Evolution of Interference leakage with time at SNR=25dB and normalized Doppler frequency $\nu_{\mathrm{D}} = 0.001$. The length of the pilot sequence $M = 15$. The length of the payload $T = 45$. The number of channel taps $S = 3$. The number of symbol extensions $N = 5$. The number of feedback bits $N_{\mathrm{d}} = 15$.

the average achievable rate is defined as

$$R_{\mathrm{lb}} = \mathbb{E}\left[R_{\mathrm{sum}}^{\mathrm{perfect}}\right] - \Delta R_{\mathrm{ub}}. \tag{3.69}$$

Due to the fact that the average sum rate given perfect CSI is a constant, we can use this lower bound to examine the effectiveness of the subspace switching algorithm (3.68). For such a setting, (3.22) suggests that the optimal subspace dimension $\mathcal{D}_{\mathrm{ub}}$ is 2 for unquantized feedback. However, as discussed earlier, higher subspace dimension will lead to a larger quantization error. To find the best subspace dimension, we present the achieved rate and the corresponding lower bound at both $D = \{1, 2\}$. It can be observed that the achieved sum rate increases with the number of feedback bits. For $D = 1$, it achieves an initial higher rate due to smaller quantization error. The achieved rate becomes a constant with the increase of N_d due to the dominance of the prediction error. When more than 15 bits are used, the two dimensional subspace outperforms the one dimensional subspace due to the better capability of channel prediction. The tradeoff between the quality of channel prediction and quantization is well captured by the lower bounds, which exhibit almost the same switching point as that obtained by MC simulation. Thus, the adaptive subspace dimension switching algorithm (3.68), denoted by adpt.SDS, is efficient to find the

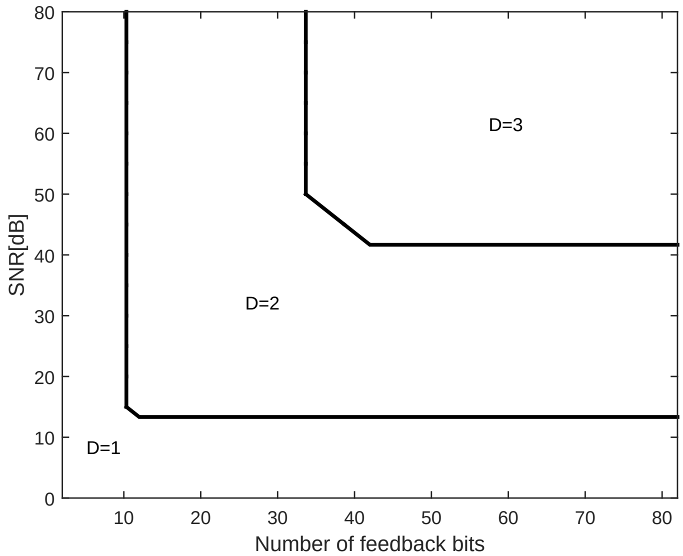

Figure 3.4: Subspace dimension obtained according to (3.68), as a function of SNR and the number of feedback bits at normalized Doppler frequency $\nu_{\mathrm{D}} = 0.004$. The length of the pilot sequence $M = 15$. The length of the payload $T = 45$. The number of channel taps $S = 2$. The number of symbol extensions $N = 5$.

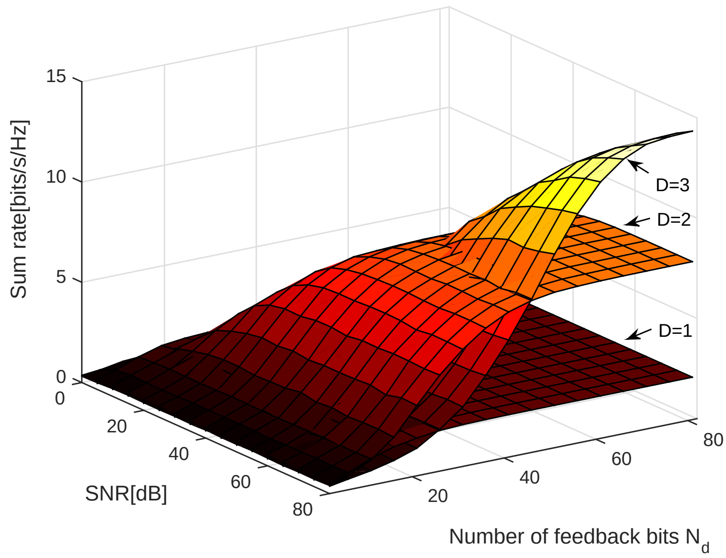

Figure 3.5: Sum rate with subspace dimension $D \in \{1, 2, 3\}$, as a function of SNR and the number of feedback bits at normalized Doppler frequency $\nu_{\mathrm{D}} = 0.004$. The length of the pilot sequence $M = 15$. The length of the payload $T = 45$. The number of channel taps $S = 2$. The number of symbol extensions $N = 5$.

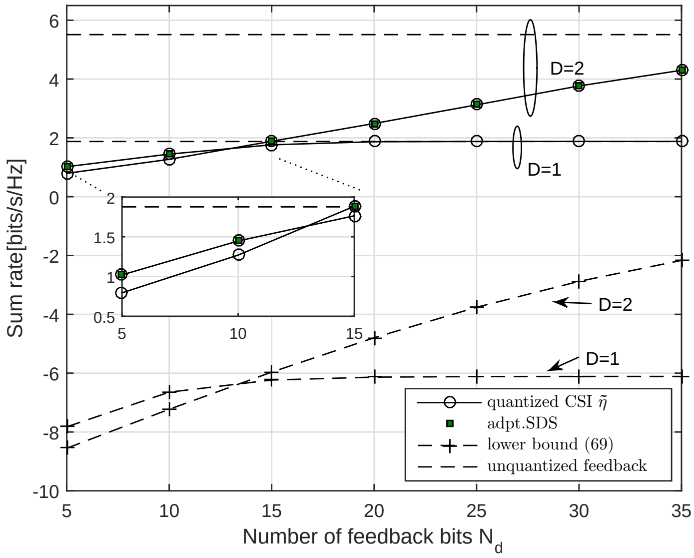

Figure 3.6: Sum rate versus the number of feedback bits at SNR=30dB and the normalized Doppler frequency $\nu_{\mathrm{D}} = 0.004$. The length of the pilot sequence $M = 15$. The length of the payload $T = 45$. The number of channel taps $S = 3$. The number of symbol extensions $N = 5$.

subspace dimension associated with a higher rate.

Fig. 3.7 shows the sum rate degradation as the increase of the normalized Doppler frequency with a feedback delay $T_{\mathrm{D}} = 7$ (0.5 ms) $\forall k, \ell$. The performance is also compared to the traditional non-predictive strategy (denoted as "quantized CIR"), which feeds back the channel impulse response (CIR) and assumes the channel is constant over the frame length. The estimate of the impulse response is obtained using the solution presented in Section 3.3 and then averaged over all pilot positions. At low Doppler frequency, a lower subspace dimension is selected. For $D = 1$, the rates achieved by non-predictive and proposed algorithms are similar. This is due to the first dimensional DPS sequence is almost a constant, therefore incapable to predict the channel. As the Doppler frequency increases, the DPS sequences of dimension $D = 2$ outperform when the rate increase due to better channel prediction is higher than the rate decrease due to increased quantization error. It also can be seen that the intersection point of the sum rate lower bound for $D \in \{1, 2\}$ is almost the same as the one for the MC simulation. Therefore, by evaluating the rate loss upper bound, the adpt.SDS algorithm (3.68) is able to select the subspace dimension with a higher rate.

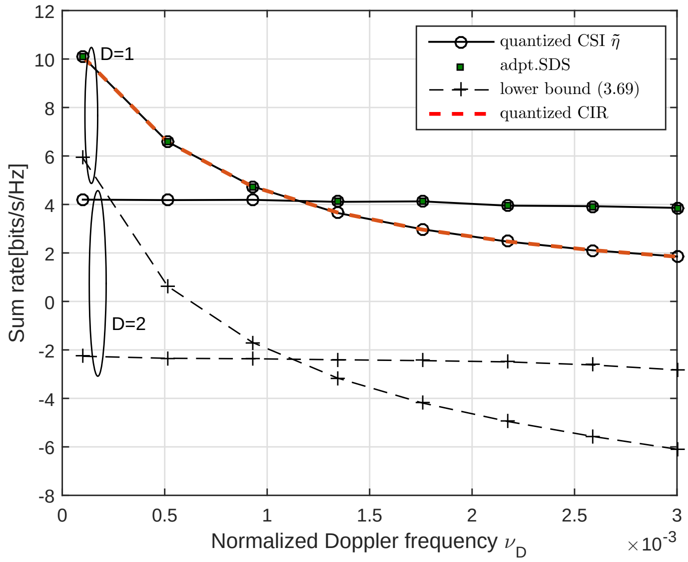

Figure 3.7: Sum rate degradation versus the increase of the normalized Doppler frequency. A 0.5 ms feedback delay $T_\mathrm{D} = 7$ is considered $\forall k, \ell$. The length of the pilot sequence $M = 15$. The length of the payload $T = 45$. The number of channel taps $S = 3$. The number of symbol extensions $N = 5$.

3.6.3 Numerical Results on Sum Rate

Fig. 3.8 illustrates the sum rate at normalized Doppler frequency $\nu_\mathrm{D} = 0.004$ (24.2km/h) with feedback delay $T_\mathrm{D} = 7$ (0.5 ms) $\forall k, \ell$. The prediction algorithm with adapt.SDS has a subspace dimension $D = 1$ at low SNRs, which results in a similar performance to "quantized CIR". For $N_\mathrm{d} = 30$, the optimal subspace dimension D switches to 2 at SNR $= 15$ dB. For $N_\mathrm{d} = 15$, the switch takes place later at SNR $= 20$ dB. As a result, better channel prediction is achieved at higher SNR, especially for a large number of feedback bits. The adaptive subspace dimension switching algorithm is able to efficiently find the dimension associated with a higher rate, which guarantees the superiority of the proposed feedback scheme over the non-predictive strategy.

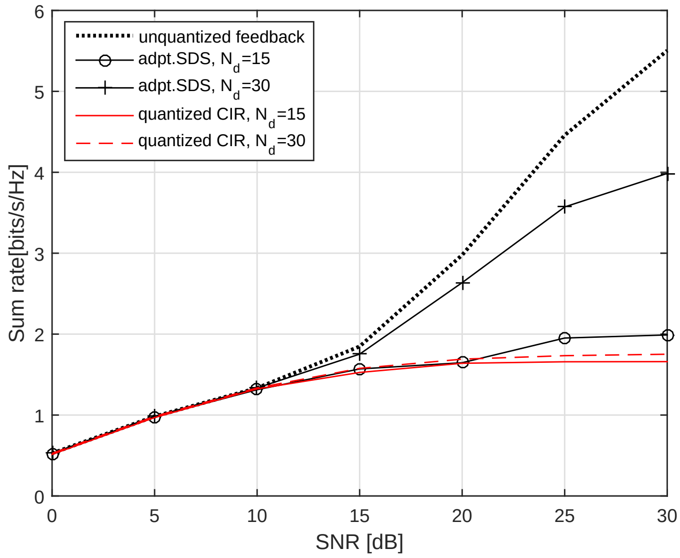

Figure 3.8: Sum rate versus SNR at normalized Doppler frequency $\nu_{\mathrm{D}} = 0.004$. A 0.5 ms feedback delay $T_{\mathrm{D}} = 7$ is considered $\forall k, \ell$. The length of the pilot sequence $M = 15$. The length of the payload $T = 30$. The number of channel taps $S = 3$. The number of symbol extensions $N = 5$.

3.7 Appendix

3.7.1 Grassmannian Manifold Basics

In this chapter, the proposed quantization and limited feedback algorithm exploits the invariance properties of the cost function to minimize the required amount of feedback exchange between receivers and transmitters. In particular, the considered quantization variables represent the channel subspace information, which can be efficiently represented on the Grassmannian manifold to adapt the transmission over a certain subspace of the channel matrix. The Grassmannian Manifold concept has been introduced in several fields of wireless communications, including capacity evaluations in single user MIMO systems [89], codebook design for single- and multi-user MIMO with limited feedback [60, 78], IA [38], metric design for opportunistic transmission in interference broadcast channel [18], etc. Therefore, in this section a short overview to the Grassmannian manifold is provided.

Definition of the Grassmannian Manifold

The Grassmannian manifold $\mathcal{G}_{m,n}(\mathbb{K})$ with $n \leq m$ is the set of all n-dimensional subspaces in the m-dimensional vector space $\mathbb{K}^m$, for example with $\mathbb{K} = \mathbb{C}$. In this dissertation, the vector space $\mathbb{K}$ underlying the considered Grassmannian is the Euclidean space of complex numbers $\mathbb{C}$. For notational brevity, it is written as $\mathcal{G}_{m,n} = \mathcal{G}_{m,n}(\mathbb{C})$.

A point $A \in \mathcal{G}_{m,n}$ on the Grassmannian manifold can be represented by any matrix $\mathbf{A} \in \mathbb{C}^{m\times n}$ whose columns span the subspace defined by $\mathbf{A}$, i.e., $A = \mathrm{span}(\mathbf{A})$. To unify this representation, orthonormal bases (truncated unitary matrices) are employed throughput this thesis to identify points on the Grassmannian

$$A \in \mathcal{G}_{m,n} \leftrightarrow \mathbf{A}^{\mathrm{H}}\mathbf{A} = \mathbf{I}_n. \tag{3.70}$$

Distance Measure on the Grassmannian Manifold

It is essential to determine the distance between points for quantizing a source on the Grassmannian manifold. In MIMO wireless communications with limited feedback, several distances between two subspaces represented by orthonormal bases $A, B \in \mathcal{G}_{m,n}$ are defined, e.g. the chordal distance, the projection two-norm and the Fubini-Study distance [90]. They are related to different design criteria for codebook based precoder designs. In this thesis, the chordal distance is employed, which is defined as

$$d_{\mathrm{c}}(\mathbf{A},\mathbf{B}) = \sqrt{n - \mathrm{tr}(\mathbf{A}^{\mathrm{H}}\mathbf{B}\mathbf{B}^{\mathrm{H}}\mathbf{A})}. \tag{3.71}$$

3.7.2 Proof of (3.62)

The delay domain subspace vector $\tilde{\boldsymbol{\eta}}_{k,k}$ can be written as

$$\begin{aligned}
&\mathbb{E}\|\tilde{\boldsymbol{\eta}}_{k,k}\|^2 \\
&= \sum_{s=1}^{S} \mathbb{E}\|\boldsymbol{\lambda}_{k,k}^{-\frac{1}{2}}\tilde{\boldsymbol{\gamma}}_{k,k}^{s}\|^2 && (3.72)\\
&= \sum_{s=1}^{S} \mathbb{E}\left[\mathrm{tr}\left(\boldsymbol{\lambda}_{k,k}^{-\frac{1}{2}}\tilde{\boldsymbol{\gamma}}_{k,k}^{s}\tilde{\boldsymbol{\gamma}}_{k,k}^{s\mathrm{H}}\boldsymbol{\lambda}_{k,k}^{-\frac{1}{2}}\right)\right] && (3.73)\\
&= \mathrm{tr}\left(\boldsymbol{\lambda}_{k,k}^{-\frac{1}{2}}\sum_{s=1}^{S}\mathbb{E}\{\tilde{\boldsymbol{\gamma}}_{k,k}^{s}\tilde{\boldsymbol{\gamma}}_{k,k}^{s\mathrm{H}}\}\boldsymbol{\lambda}_{k,k}^{-\frac{1}{2}}\right) && (3.74)\\
&= DS && (3.75)
\end{aligned}$$

where

$$\mathbb{E}\{\tilde{\boldsymbol{\gamma}}_{k,k}^{s}\tilde{\boldsymbol{\gamma}}_{k,k}^{s\mathrm{H}}\} = \mathbf{G}^{-1}\mathbf{U}^{(\mathcal{P})^{\mathrm{H}}}\left(p_{k,k}^{s}\mathbf{R}_{\mathbf{h}_{k,k}}^{(\mathcal{P})} + \frac{1}{P}\mathbf{I}_{\frac{M}{K}}\right)\mathbf{U}^{(\mathcal{P})}\mathbf{G}^{-1} \tag{3.76}$$

and (3.75) is obtained using the fact $\sum_{s=1}^{S} p_{k,\ell}^{s} = N$.

4 Opportunistic Interference Alignment

Interference alignment (IA) requires global channel state information (CSI) at transmitters to realize the degrees of freedom (DoF) gain. To relief the global CSI burden, a lot of efforts have been put on developing iterative IA algorithms based on the reciprocity between uplink and downlink channels [41, 47] in time-division duplex (TDD) systems, limited feedback [30,38,55] and analog feedback [61] algorithms in frequency-division duplex (FDD) systems.

As an alternative to IA, opportunistic interference alignment (OIA) has been proposed [13–18], which exploits channel randomness and multiuser diversity by user selection. Contrary to IA, global channel knowledge at each transmitter is not required, instead each receiver just needs to feed back a scalar indicating the degree of alignment. In this Chapter, we investigate threshold-based feedback schemes, which further reduce the amount of feedback for OIA. The choices of threshold, user scaling law and the achievability of DoF are investigated.

4.1 Background

To relief the global CSI constraint, OIA has been studied lately [13–18]. The key idea of OIA is to exploit the channel randomness and multiuser diversity by proper user selection. In [13–18], signal subspace dimensions are used to align the interference signals. Each transmitter opportunistically selects and serves the user whose interference channels are most aligned to each other. The degree of alignment is quantified by a metric. To facilitate a user selection algorithm, all potential users associated with the transmitter are required to calculate and feedback the metric value based on the local CSI. Perfect IA can be achieved asymptotically if the number of users scales fast enough with signal-to-noise ratio (SNR). The corresponding user scaling law to obtain the optimal DoF is characterized for multiple access channels in [13,14] and for downlink interference channels in [16–18].

The work in [16] decouples a multiple-input multiple-output (MIMO) interference channel into multiple single-input multiple-output (SIMO) interference channels and guarantees each selected user with one spatial stream. Since each stream is associated with one metric value, therefore multiple metric values have to be fed back from each user. The work of [17] reduces the number of users to achieve the optimal DoF at the expense of increased feedback information from each user. In [17], each user has to feed back a metric value and a channel vector to cancel intra-cell interference. To enable multiple spatial streams for each selected user, the authors of [18] investigate the required user scaling in 3-cell MIMO interference channels and show that the optimal DoF d is achieved if the number of users N is scaled as $N \propto \mathrm{SNR}^{d^2}$. Therefore, at higher SNR, a larger number of users is required to achieve the optimal DoF. Clearly, the level of required total CSI feedback also increases proportionally to the number of users. However, in practical systems, the feedback is costly and the bandwidth of the feedback channel is limited. As a result, the feedback rate should be kept as small as possible.

For opportunistic transmission in point-to-point systems, the problem of feedback reduction is tackled in [91–93] by selective feedback. The solution is to let the users threshold their receive SNRs and notify the transmitter only if their SNR exceeds a predetermined threshold. The work in [91,92] reduces the number of real-valued variables that must be fed back to the transmitter in single-input single-output (SISO) and MIMO multiuser channels respectively. But [91, 92] do not directly address the question of feedback rate since transmission of real-valued variables requires infinite rate. The work in [93] investigates the performance of opportunistic multiuser systems using limited feedback and proves that 1-bit feedback per user can capture a double-logarithmic capacity growth with the number of users. Note that [91–93] consider interference-free point-to-point transmissions.

Unlike point-to-point systems where the imperfect CSI causes only an SNR offset in the capacity, the accuracy of the CSI in interference channels affects *the slope of the rate curve*, i.e., the DoF. Thus, for OIA, a relation to the DoF using selective feedback is critical. Can we reduce the amount of feedback and still preserve the optimal DoF? In this chapter, we consider this problem for 3-user interference broadcast channels.

In Section 4.4, we address this problem using real-valued feedback. We show that the amount of feedback can be dramatically reduced by more than one order of magnitude while still preserving the essential DoF promised by conventional OIA with perfect real-valued feedback.

In Section 4.5, the achievability of the optimal DoF with limited feedback is investigated. We prove that only 1-bit feedback per user is sufficient to achieve the full DoF (without requiring more users than real-valued feedback) if the one-bit quantizer is chosen judiciously. We provide an optimal choice of the 1-bit quantizer to achieve the DoF of 1, which captures most of the capacity provided by a system with real-valued feedback. To achieve a DoF $d > 1$, an asymptotic threshold choice is given by solving an upper bound for the rate loss. The DoF achievable threshold is not unique. We generalize the design of the threshold choices and provide the mathematical expression.

In Section 4.6, we compare OIA and IA with the same amount of feedback and present the comparison in terms of complexity and achievable rate. We show that OIA has a simpler quantizer and provides a higher sum rate in the practical operation region of a cellular communication system.

4.2 3-User Interference Broadcast Channels

Let us consider the system model for the 3-user MIMO interference broadcast channel, as shown in Fig. 4.1. It consists of 3 transmitters with N_{T} antennas, each serving N users with N_{R} antennas. The channel matrix from transmitter ℓ to receiver n in cell k is denoted by $\mathbf{H}_{k,\ell}^{n} \in \mathbb{C}^{N_{\mathrm{R}} \times N_{\mathrm{T}}}$, $\forall k, \ell \in \{1,2,3\}$ and $n \in \{1,\ldots,N\}$. Every element of $\mathbf{H}_{k,\ell}^{n}$ is assumed as an independent identically distributed (i.i.d.) symmetric complex Gaussian random variable with zero mean and unit variance.

For a given transmitter, its signal is only intended to be received and decoded by a single user for a given signaling interval. The signal received at receiver $n \in \{1,\ldots,N\}$ in cell k at a given time instant is the superposition of the signals transmitted by all three transmitters, which can be written as

$$\mathbf{y}_{k}^{n} = \mathbf{H}_{k,k}^{n}\mathbf{s}_{k} + \sum_{\ell=1,\ell\neq k}^{3} \mathbf{H}_{k,\ell}^{n}\mathbf{s}_{\ell} + \mathbf{n}_{k}^{n}, \tag{4.1}$$

where vector $\mathbf{s}_{\ell} \in \mathbb{C}^{d\times 1}$ denotes d transmitted symbols from transmitter ℓ with power constraint $\mathbb{E}\{\mathbf{s}_{\ell}\mathbf{s}_{\ell}^{\mathrm{H}}\} = \frac{P}{d}\mathbf{I}_{d}$. The additive complex symmetric Gaussian noise $\mathbf{n}_{k}^{n} \sim \mathcal{CN}(0, \mathbf{I}_{N_{\mathrm{R}}})$ has zero mean and unit variance. Thus, the SNR becomes SNR $=$ P. In this paper, we confine ourselves to the case of $N_{\mathrm{R}} = 2d$ and $N_{\mathrm{T}} = d$. This is interesting because it is the minimum setup to achieve the full DoF d at each receiver. In case the number of receive antennas $N_{\mathrm{R}} > 2d$, $N_{\mathrm{R}} - 2d$ DoF can be obtained with probability one even without interference management because uncoordinated interference signals will span a subspace with a maximum of $2d$ dimensions in the space $\mathbb{C}^{N_{\mathrm{R}}}$. On the other hand if $N_{\mathrm{R}} < 2d$, the full DoF d is not achievable because the interference signals will span at least a d dimensional subspace even when they are perfectly aligned. The model in (4.1) is statistically equivalent to the case when $N_{\mathrm{T}} \geq d$ and a linear precoding matrix $\mathbf{V}_{\ell} \in \mathbb{C}^{N_{\mathrm{T}}\times d}$ is applied to each transmitter as $\mathbf{y}_{k}^{n} = \mathbf{H}_{k,k}^{n}\mathbf{V}_{k}\mathbf{s}_{k} + \sum_{\ell=1,\ell\neq k}^{3} \mathbf{H}_{k,\ell}^{n}\mathbf{V}_{\ell}\mathbf{s}_{\ell} + \mathbf{n}_{k}^{n}$.

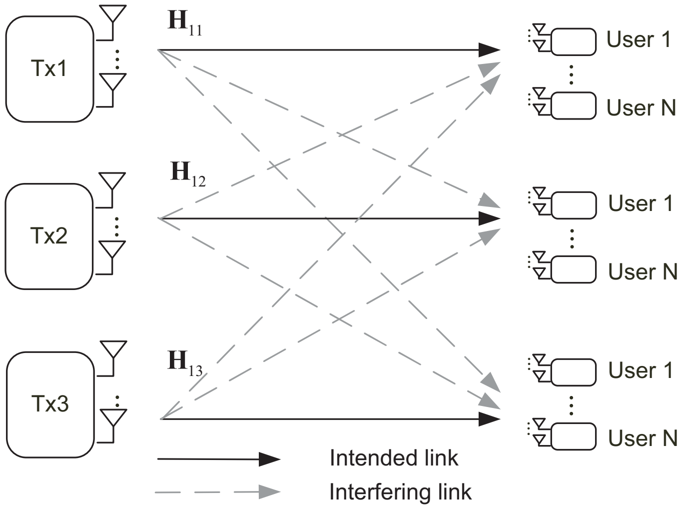

Figure 4.1: Three-user interference broadcast channel with N candidates in each cell

Defining $\mathbf{U}_k^n \in \mathbb{C}^{N_\mathrm{R} \times d}$ as the postfiltering matrix at receiver n in cell k, the received signal of user n in cell k becomes

$$\mathbf{U}_k^{n\mathrm{H}} \mathbf{y}_k^n = \mathbf{U}_k^{n\mathrm{H}} \mathbf{H}_{k,k}^n \mathbf{s}_k + \sum_{\ell=1,\ell\neq k}^{3} \mathbf{U}_k^{n\mathrm{H}} \mathbf{H}_{k,\ell}^n \mathbf{s}_\ell + \bar{\mathbf{n}}_k^n \tag{4.2}$$

where $\bar{\mathbf{n}}_k^n = \mathbf{U}_k^{n\mathrm{H}} \mathbf{n}_k^n$ denotes the effective spatially white noise vector. The achievable instantaneous rate for user n in cell k becomes

$$R_k^n = \log_2 \det\left(\mathbf{I}_d + \frac{P}{d} \mathbf{U}_k^{n\mathrm{H}} \mathbf{H}_{k,k}^n {\mathbf{H}_{k,k}^n}^{\mathrm{H}} \mathbf{U}_k^n \left(\frac{P}{d} \sum_{\ell=1,\ell\neq k}^{3} \mathbf{U}_k^{k\mathrm{H}} \mathbf{H}_{k,\ell}^n {\mathbf{H}_{k,\ell}^n}^{\mathrm{H}} \mathbf{U}_k^n + \mathbf{I}_d\right)^{-1}\right) \tag{4.3}$$

$$= \underbrace{\log_2 \det\left(\mathbf{I}_d + \sum_{\ell=1}^{3} \frac{P}{d} \mathbf{U}_k^{n\mathrm{H}} \mathbf{H}_{k,k}^n {\mathbf{H}_{k,k}^n}^{\mathrm{H}} \mathbf{U}_k^n\right)}_{{R_{\mathrm{gain}}}_k^n} - \underbrace{\log_2 \det\left(\mathbf{I}_d + \sum_{\ell=1,\ell\neq k}^{3} \frac{P}{d} \mathbf{U}_k^{n\mathrm{H}} \mathbf{H}_{k,\ell}^n {\mathbf{H}_{k,\ell}^n}^{\mathrm{H}} \mathbf{U}_k^n\right)}_{{R_{\mathrm{loss}}}_k^n} \tag{4.4}$$

where in (4.4) we decompose the achievable rate into a rate gain term ${R_{\mathrm{gain}}}_k^n$ and a rate loss term ${R_{\mathrm{loss}}}_k^n$. Therefore, the DoF achieved for user n in cell k can be written as

$$\mathrm{DoF}_k^n = \lim_{P\to\infty} \frac{\mathbb{E}[R_k^n]}{\log_2 P} \tag{4.5}$$

$$= d - \underbrace{\lim_{P\to\infty} \frac{\mathbb{E}[R_{\mathrm{loss}}{}_k^n]}{\log_2 P}}_{\mathrm{DoF}_{\mathrm{loss}}{}_k^n} \tag{4.6}$$

where (4.6) is obtained due to $\lim_{P\to\infty} \frac{\mathbb{E}[R_{\mathrm{gain}}{}_k^n]}{\log_2 P} = d$. Therefore, in the rest of the paper, we will focus on the rate loss and DoF loss terms in order to analyze the achieved DoF.

4.2.1 Conventional OIA

Without requiring global channel knowledge, OIA is able to achieve the same DoF as IA with only local CSI feedback within a cell. In this section, we describe the selection criteria and the design of the postfilter for the conventional OIA algorithm. The key idea of OIA [18] is to exploit the channel randomness and the multi-user diversity, using the following procedure:

- Each transmitter sends out a reference signal.
- Each user equipment measures the channel quality using a specific metric.
- Every user feeds back the value of the metric to its own transmitter.
- The transmitter selects a user in its own cell for communication according to the feedback values.

We denote the index of the selected user in cell k by n^*. The transmitters aim at choosing a user, who observes most aligned interference signals from the other transmitters. The degree of alignment is quantified by a subspace distance measure, named chordal distance. It is defined as

$$d_{\mathrm{c}}(\mathbf{A}, \mathbf{B}) = \sqrt{d - \mathrm{tr}(\mathbf{A}^{\mathrm{H}}\mathbf{B}\mathbf{B}^{\mathrm{H}}\mathbf{A})} \tag{4.7}$$

$$= 1/\sqrt{2}\left\|\mathbf{A}\mathbf{A}^{\mathrm{H}} - \mathbf{B}\mathbf{B}^{\mathrm{H}}\right\|_{\mathrm{F}} \tag{4.8}$$

where $\mathbf{A}, \mathbf{B} \in \mathbb{C}^{N_{\mathrm{R}}\times d}$ are the orthonormal bases of two subspaces and ${d_{\mathrm{c}}}^2(\mathbf{A}, \mathbf{B}) \leq d$. For OIA, each user finds an orthonormal basis $\mathbf{Q}$ of the column space spanned by the two interference channels respectively, i.e., $\mathbf{Q}_{k,p}^n \in \mathrm{span}(\mathbf{H}_{k,p}^n)$ and $\mathbf{Q}_{k,q}^n \in \mathrm{span}(\mathbf{H}_{k,q}^n)$ where $p = (k+1 \mod 3)$ and $q = (k+2 \mod 3)$. Then the users calculate the distance between two interference subspaces using the obtained orthonormal basis, yielding

$$\mathcal{D}_k^n = d_{\mathrm{c}}^2(\mathbf{Q}_{k,p}^n, \mathbf{Q}_{k,q}^n), \tag{4.9}$$

where $\mathcal{D}_k^n$ is the distance measured at user n in cell k. For conventional OIA, all users feed back the distance measure to their own transmitter and the user selected by transmitter k is given by

$$n^* = \arg\min_n \ \mathcal{D}_k^n. \tag{4.10}$$

Therefore, the metric value of the selected user becomes $\mathcal{D}_k^{n^*}$. Defining the received interference covariance matrix of the selected user n^* as

$$\mathbf{R}_k^{n^*} = \mathbf{H}_{k,p}^{n^*}\mathbf{H}_{k,p}^{n^*\,\mathrm{H}} + \mathbf{H}_{k,q}^{n^*}\mathbf{H}_{k,q}^{n^*\,\mathrm{H}}, \tag{4.11}$$

the decoder applied at the selected user becomes

$$\mathbf{U}_k^{n^*} = [\vec{\mathbf{u}}_{d+1}(\mathbf{R}_k^{n^*}), \cdots, \vec{\mathbf{u}}_{N_{\mathrm{R}}}(\mathbf{R}_k^{n^*})] \tag{4.12}$$

where $\vec{\mathbf{u}}_a(\mathbf{R})$ represent the singular vector corresponding to the a-th largest singular value of $\mathbf{R}$.

4.2.2 Achievable DoF of Conventional OIA

As shown in [80], for quantizing a source $\mathbf{A}$ arbitrarily distributed on the Grassmannian manifold $\mathcal{G}_{N_{\mathrm{R}},d}(\mathbb{C})$ by using a random codebook $\mathcal{C}_{\mathrm{rnd}}$ with N codewords, the second moment of the chordal distance can be bounded as

$$Q(N) = \mathbb{E}\left[\min_{\mathbf{C}_n \in \mathcal{C}_{\mathrm{rnd}}} d_{\mathrm{c}}^2(\mathbf{A}, \mathbf{C}_n)\right] \tag{4.13}$$

$$\leq \frac{\Gamma(\frac{1}{d(N_{\mathrm{R}}-d)})}{d(N_{\mathrm{R}}-d)}(N c_{N_{\mathrm{R}},d})^{-\frac{1}{d(N_{\mathrm{R}}-d)}} \tag{4.14}$$

where $\Gamma(\cdot)$ denotes the Gamma function and the random codebook $\mathcal{C}_{\mathrm{rnd}} \subset \mathcal{G}_{N_{\mathrm{R}},d}(\mathbb{C})$. The constant $c_{N_{\mathrm{R}},d}$ is the ball volume on the Grassmannian manifold $\mathcal{G}_{N_{\mathrm{R}},d}(\mathbb{C})$, i.e.

$$c_{N_{\mathrm{R}},d} = \frac{1}{\Gamma(d(N_{\mathrm{R}}-d)+1)} \prod_{i=1}^{d} \frac{\Gamma(N_{\mathrm{R}}-i+1)}{\Gamma(d-i+1)}. \tag{4.15}$$

The problem of selecting the best user out of N users is equivalent to quantizing an arbitrary subspace with N random subspaces on the Grassmannian manifold $\mathcal{G}_{N_{\mathrm{R}},d}(\mathbb{C})$ [18, Lemma 4]. Therefore, we have $\mathbb{E}\left[\mathcal{D}_k^n\right] = Q(1)$ and $\mathbb{E}\left[\mathcal{D}_k^{n^*}\right] = Q(N)$.

We briefly revisit the results obtained in [18], which will be used for comparison with our 1-bit feedback OIA. A finite number of users N results in residual interference. When the cell k has N users, the average rate loss at the selected user n^* can be bounded as

$$\begin{aligned}\mathbb{E}[R_{\mathrm{loss}}{}_k^{n^*}] \leq & d \cdot \log_2\left(1 + \frac{P}{d} \cdot \mathbb{E}[\mathcal{D}_k^{n^*}]\right) && (4.16)\\ = & d \cdot \log_2\left(1 + \frac{P}{d} \cdot Q(N)\right), && (4.17)\end{aligned}$$

where (4.16) is obtained due to [18, Lemma 6].

The achievable DoF of transmitter k using OIA can be expressed by $d - \lim_{P\to\infty} \frac{\mathbb{E}[R_{\mathrm{loss}}{}_k^{n^*}]}{\log_2 P}$. In order to achieve the DoF of d', the number of users per cell has to be scaled as [18, Theorem 2]

$$N \propto P^{dd'}. \tag{4.18}$$

4.3 Metric Distribution

This section provides general definitions for the distribution of the underlying metric. These definitions will be used for the designs of the thresholds in Sections 4.4 and 4.5.

We first denote the cumulative density function (CDF) of $\mathcal{D}_k^n$ by $F_{\mathcal{D}}(x)$, which is defined as

$$\begin{aligned}F_{\mathcal{D}}(x) &= \Pr(\mathcal{D}_k^n \leq x) && (4.19)\\ &= \Pr(d_{\mathrm{c}}^2(\mathbf{A}, \mathbf{C}_n) \leq x) && (4.20)\\ &\approx \begin{cases} 0, & x < 0 \\ c_{N_{\mathrm{R}},d} \cdot x^{d(N_{\mathrm{R}}-d)}, & 0 \leq x \leq \hat{x} \\ 1, & x > \hat{x} \end{cases} && (4.21)\end{aligned}$$

where $\hat{x}$ satisfies $c_{N_{\mathrm{R}},d} \cdot \hat{x}^{d(N_{\mathrm{R}}-d)} = 1$ and $\hat{x} \leq d$. If $d = 1$, the CDF of (4.21) becomes exact. If $d > 1$, the CDF in (4.21) is exact when $0 \leq x \leq 1$. When $1 < x < d$, the CDF provided by (4.21) deviates from the true CDF [80]. However, we are mainly interested in small $x < 1$ for the purpose of feedback reduction by thresholding.

The scheduling outage probability corresponds to the event where all N users

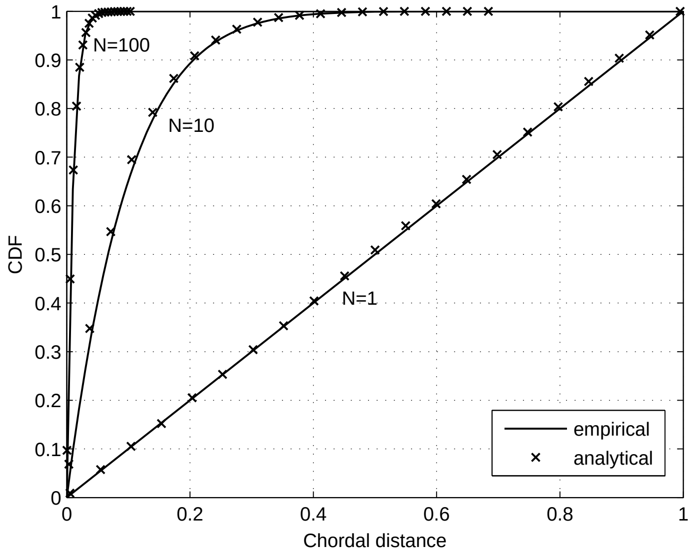

Figure 4.2: The CDF of $\mathcal{D}_k^{n^*}$ with varying number of users N in each cell. The number of receive antennas $N_{\mathrm{R}} = 2$. The number of transmitted symbols $d = 1$.

exceed x, which is denoted by

$$P_{\text{out}} = \Pr(\min_{n} \ \mathcal{D}_k^n \geq x) \tag{4.22}$$

$$= \Pr(\min_{\mathbf{C}_n \in \mathcal{C}_{\text{rnd}}} d_{\text{c}}^2(\mathbf{A}, \mathbf{C}_n) \ \geq x) \tag{4.23}$$

$$= \left(1 - F_{\mathcal{D}}\left(x_{\text{th}}\right)\right)^N . \tag{4.24}$$

4.4 Real-valued Feedback Reduction by Thresholding

For OIA, the user selected for transmission is the one with the smallest chordal distance measure. For a reasonable number of users N, it can rarely happen that a user with a "bad" channel will be selected by the transmitter. Therefore, the feedback channel bandwidth provisioned for such a user is wasted. In fact, only the users experiencing good enough conditions have a good chance to be selected and should feedback their channel quality. To this end, we propose a threshold-based feedback strategy where only a subset of users, whose chordal distance measure is smaller than a predetermined threshold, send feedback to the transmitter. Importantly, users decide locally whether they should attempt to access the channel and send feedback to the transmitter or not. Hence, only a fraction of the users are required to send feedback and the required bandwidth of the feedback channel can be reduced substantially.

For the selected user, the CDF of $\mathcal{D}_k^{n^*}$, defined as $F_{\mathcal{D}}^N(x)$, corresponds to the complement of the event where all N users exceeds x, which can be written as

$$F_{\mathcal{D}}^N(x) = \Pr(\min_n \ \mathcal{D}_k^n < x) \tag{4.25}$$

$$= 1 - \left(1 - F_{\mathcal{D}}\left(x_{\text{th}}\right)\right)^N . \tag{4.26}$$

Fig. 4.2 shows the CDF of $\mathcal{D}_k^{n^*}$ with $N_{\text{R}} = 2$ receive antennas and $d = 1$ transmitted symbols. The analytical and empirical results are presented with different number of users $N \in \{1, 10, 100\}$. It can be observed that the analytical results obtained from (4.26) agree perfectly with empirical results. When $N = 1$, $F_{\mathcal{D}}^N(x)$ $=F_{\mathcal{D}}(x)$ is the CDF of chordal distance before user selection. The chordal distance measure of the best user $\mathcal{D}_k^{n^*}$ becomes smaller with the increasing N. Intuitively speaking, with a relatively large N, the chordal distance measure of the best user is very small and has a more concentrated distribution, as shown in Fig. 4.2. This observation gives rise to our proposed selective feedback scheme for OIA. For instance, When $N = 10$, a threshold of 0.4 guarantees with nearly probability one that the best user would fall below the threshold and sends feedback to the transmitter. Therefore, only 40% of the users will feed back a value to the transmitter (since $F_{\mathcal{D}}(x) = x$ for $0 \leq x \leq 1$ when $N_{\text{R}} = 2$ and $d = 1$). On the other hand, a scheduling outage occurs if no user sends feedback to the transmitter. In such an event, a random user will be selected.

4.4.1 Selective Feedback by Thresholding

OIA is able to achieve the optimal DoF, if the number of users in each cell scales with P^{d^2}. For threshold-based OIA, it is unknown how to set a threshold such that the DoF is still achievable. In this section, we characterize the threshold as a function of the transmit power for different MIMO configurations. We define the probability density functions (PDFs) of $\mathcal{D}_k^n$ and $\mathcal{D}_k^{n^*}$ as $f_{\mathcal{D}}(x)$ and $f_{\mathcal{D}}^N(x)$ respectively, where $\int_{-\infty}^x f_{\mathcal{D}}(x)\mathrm{d}x = F_{\mathcal{D}}(x)$ and $\int_{-\infty}^x f_{\mathcal{D}}^N(x)\mathrm{d}x = F_{\mathcal{D}}^N(x)$. In order to distinguish from the previous conventional OIA, we employ $n^\dagger$ as the index of the selected user with threshold-based selective feedback. Denoting the feedback threshold by x_{th}, the expected metric value of the selected user $n^\dagger$ can be expressed as

$$\mathbb{E}[\mathcal{D}_k^{n^\dagger}] = F_{\mathcal{D}}^N(x_{\mathrm{th}}) \frac{\int_0^{x_{\mathrm{th}}} f_{\mathcal{D}}^N(x) x \mathrm{d}x}{F_{\mathcal{D}}^N(x_{\mathrm{th}})} + \left(1 - F_{\mathcal{D}}^N(x_{\mathrm{th}})\right) \frac{\int_{x_{\mathrm{th}}}^d f_{\mathcal{D}}(x) x \mathrm{d}x}{1 - F_{\mathcal{D}}(x_{\mathrm{th}})} \tag{4.27}$$

$$\leq \int_0^d f_{\mathcal{D}}^N(x) x \mathrm{d}x + \left(1 - F_{\mathcal{D}}^N(x_{\mathrm{th}})\right) \frac{\int_{x_{\mathrm{th}}}^d f_{\mathcal{D}}(x) x \mathrm{d}x}{1 - F_{\mathcal{D}}(x_{\mathrm{th}})} \tag{4.28}$$

$$\leq \int_0^d f_{\mathcal{D}}^N(x) x \mathrm{d}x + d\left(1 - F_{\mathcal{D}}^N(x_{\mathrm{th}})\right) \tag{4.29}$$

$$= Q(N) + d\left(1 - F_{\mathcal{D}}^N(x_{\mathrm{th}})\right) \tag{4.30}$$

where $\frac{f_{\mathcal{D}}(x)}{1-F_{\mathcal{D}}(x_{\mathrm{th}})}$ and $\frac{f_{\mathcal{D}}^N(x)}{F_{\mathcal{D}}^N(x_{\mathrm{th}})}$ are the normalized truncated PDFs of $\mathcal{D}_k^n$ and $\mathcal{D}_k^{n^*}$ satisfying $\frac{\int_{x_{\mathrm{th}}}^d f_{\mathcal{D}}(x)\mathrm{d}x}{1-F_{\mathcal{D}}(x_{\mathrm{th}})} = 1$ and $\frac{\int_0^{x_{\mathrm{th}}} f_{\mathcal{D}}^N(x)\mathrm{d}x}{F_{\mathcal{D}}^N(x_{\mathrm{th}})} = 1$. The first term in (4.27) represents the event where the selected user falls below the threshold and the second term denotes a scheduling outage. Equation (4.28) follows from the fact $0 \leq x_{\mathrm{th}} \leq d$. Equation (4.29) is obtained by taking the upper limit of the integration. Since the achievable DoF of transmitter k is $d - \lim_{P\to\infty} \frac{\mathbb{E}[R_{\mathrm{loss}}{}_k^{n^*}]}{\log_2 P}$, applying the upper bound derived in (4.30) to (4.16), the full DoF d is achieved if $N \propto P^{d^2}$ and the scheduling outage probability

$$\left(1 - F_{\mathcal{D}}^N(x_{\mathrm{th}})\right) \propto \frac{1}{P} \Leftrightarrow \left(1 - F_{\mathcal{D}}^N(x_{\mathrm{th}})\right) = \frac{\alpha}{P} \tag{4.31}$$

where α is a positive constant. Therefore, the average rate loss $\mathbb{E}[R_{\mathrm{loss}}{}_k^{n^*}]$ is upper bounded by a constant when $P \to \infty$. By taking the equality of (4.31) with $\alpha = 1$ and using the results obtained in (4.26) and (4.21), the threshold which achieves the full DoF d is given by

$$x_{\mathrm{th}} \approx \left(\frac{1 - P^{\frac{-1}{N}}}{c_{N_{\mathrm{R}},d}}\right)^{\frac{1}{d(N_{\mathrm{R}}-d)}}, \tag{4.32}$$

where the approximation becomes exact for $0 \leq x_{\mathrm{th}} \leq 1$.

4.4.2 Average Feedback Load

We are interested in characterizing the required feedback load to achieve the full DoF using the proposed threshold-based selective feedback for OIA. Let us define the average feedback load N_{fb} as the average number of feedback users per cell. The normalized feedback load n_{fb} is the ratio of the average feedback load N_{fb} to the total number of users N, which is equal to $n_{\mathrm{fb}} = F_{\mathcal{D}}(x_{\mathrm{th}})$. Invoking the result obtained from (4.26) to (4.31), the normalized feedback load achieving full DoF d is given by

$$n_{\text{fb}} = F_{\mathcal{D}}(x_{\text{th}}) = 1 - P^{\frac{-1}{N}} \tag{4.33}$$

where $N \propto P^{d^2}$. Therefore, the average feedback load N_{fb} can be calculated as

$$N_{\text{fb}} = n_{\text{fb}} N = N \left(1 - P^{\frac{-1}{N}}\right). \tag{4.34}$$

4.4.3 Other Threshold Choices for OIA

The choice of the threshold x_{th} can be made according to various criteria. The threshold which satisfies a given feedback ratio n_{fb} is given by

$$x_{\text{th}} \approx \left(\frac{n_{\text{fb}}}{c_{N_{\text{R}},d}}\right)^{\frac{1}{d(N_{\text{R}}-d)}}. \tag{4.35}$$

In case if the capacity of the feedback channel is limited, the threshold satisfying a given total feedback load N is given by

$$x_{\text{th}} \approx \left(\frac{N_{\text{fb}}}{N c_{N_{\text{R}},d}}\right)^{\frac{1}{d(N_{\text{R}}-d)}}. \tag{4.36}$$

For both (4.35) and (4.36), the approximation is exact if $0 \leq x_{\text{th}} \leq 1$.

4.4.4 Simulation results

In this section, we provide numerical results of OIA in terms of sum rate using the feedback approaches abbreviated as follows:

- OIA-F: OIA with full feedback [18]
- OIA-S: OIA with our new threshold-based selective feedback

Fig. 4.3 shows the achievable sum rate versus SNR of the above schemes with $N_{\text{R}} = N_{\text{T}} = 2$, $d = 1$ and the number of users $N = P^{d^2}$. The thresholds $x_{\text{th}} = \{0, 0.305, 0.206, 0.103, 0.045, 0.018, 0.007\}$ are adaptively chosen at different SNRs according to (4.32). We can see that OIA with selective feedback achieves almost the same performance as OIA with full feedback. Both of these two schemes achieve DoF $d = 1$ compared to the reference line. However, by using the adaptive threshold (4.32), we can reduce the feedback significantly, which can be seen in Fig. 4.4. One interesting observation is that the feedback load grows very slightly with the increase

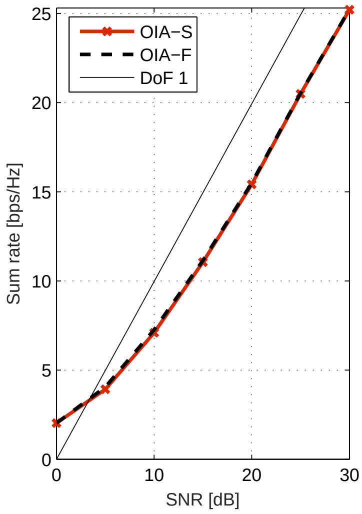

Figure 4.3: Achievable sum rate for $N_{\mathrm{R}} = N_{\mathrm{T}} = 2$, $d = 1$ and $N = P^{d^2}$.

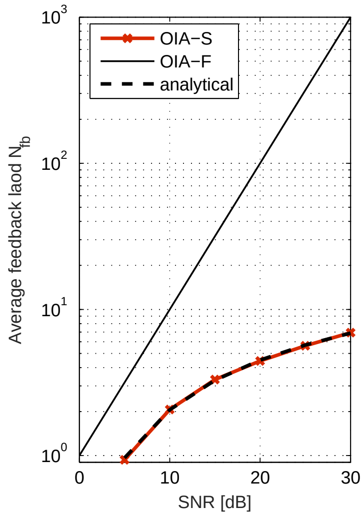

Figure 4.4: Average feedback load for $N_{\mathrm{R}} = N_{\mathrm{T}} = 2$, $d = 1$ and $N = P^{d^2}$.

of SNR. At SNR=30 dB, the average feedback load is reduced to less than 1% of the full feedback OIA. In addition, the analytical results from (4.34) perfectly matches to the simulation results.

Fig. 4.5 shows the achievable sum rate as a function of the normalized feedback load n_{fb} with $N_{\mathrm{R}} = N_{\mathrm{T}} = 2$, $d = 1$ and the number of users $N \in \{10, 30, 50, 70\}$. The corresponding thresholds are calculated using (4.35). We see that for $N \geq 30$, a 10% feedback load results in a negligible loss in sum rate.

In Fig. 4.6, the achievable sum rate is evaluated with $N_{\mathrm{R}} = N_{\mathrm{T}} = 4$, $d = 2$ and $N \in \{10, 50, 100\}$. For OIA with selective feedback, a feedback load of $n_{\mathrm{fb}} = 10\%$ is used. The corresponding threshold $x_{\mathrm{th}} = 0.669$ is obtained using (4.35). With a finite number of users, interference is inevitably leaked to the signal subspace. We can observed that the sum rate increases as the number of users increases. For $N \in \{50, 100\}$, OIA with 10% feedback load guarantees almost the same performance as OIA with full feedback.

4.5 One-Bit Feedback by Thresholding

In this section, we introduce the concept of 1-bit feedback for OIA. The achievability of DoF is proven for $d = 1$ first, where a closed-form solution exists. We generalize the result to all $d > 1$ based on asymptotic analysis.

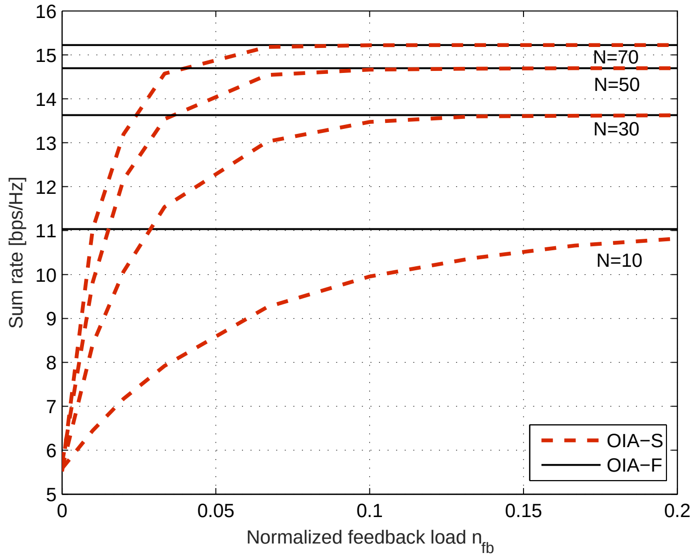

Figure 4.5: Achievable sum rate at SNR=20 dB for $N_{\mathrm{R}} = N_{\mathrm{T}} = 2$, $d = 1$ and $N \in \{10, 30, 50, 70\}$.

4.5.1 One-Bit Feedback by Thresholding

For conventional OIA, the user selected for transmission is the one with the smallest chordal distance measure. This requires that the transmitter collects the perfect real-valued chordal distance measures from all users. However, the feedback of real values require infinite bandwidth. The question of how to efficiently feedback the required CSI is still not solved for OIA. To address this problem, we propose a threshold-based 1-bit feedback strategy where each user compares the locally measured chordal distance to a predefined threshold x_{th} and reports 1-bit information to the transmitter about the comparison. In such a way, the transmitter can partition all the users into two groups and schedule a user from the favorable group for transmission. Therefore, we propose the following steps for OIA using 1-bit feedback:

- Each transmitter sends out a reference signal.
- Each user equipment measures the channel quality using the chordal distance measure.
- Each user compares the locally measured chordal distance to a threshold. In case the measured value is smaller than the threshold, a '1' will be fed back; otherwise a '0' will be fed back.

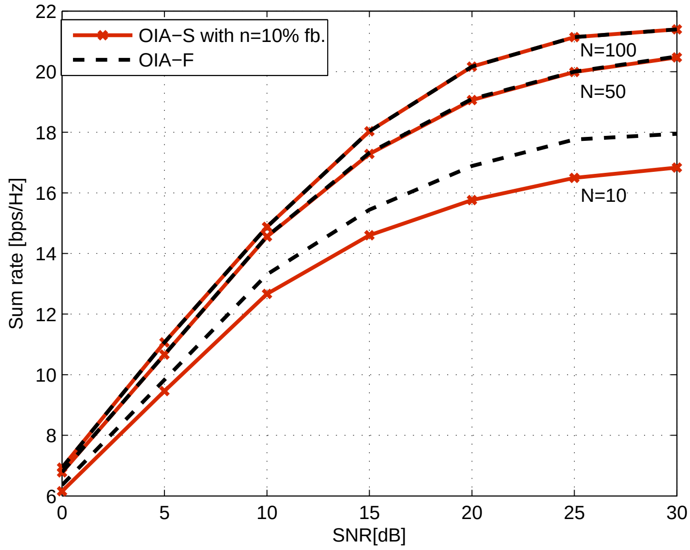

Figure 4.6: Achievable sum rate for $N_{\mathrm{R}} = N_{\mathrm{T}} = 4$, $d = 2$ and $N \in \{10, 50, 100\}$.

- The transmitter will randomly select a random user whose feedback value is '1' for transmission.

We define the PDFs of $\mathcal{D}_k^n$ as $f_{\mathcal{D}}(x)$, where $\int_0^x f_{\mathcal{D}}(x)\mathrm{d}x = F_{\mathcal{D}}(x)$. The expected metric value of the selected user $n^\dagger$ can be expressed as

$$\mathbb{E}[\mathcal{D}_k^{n^\dagger}] = (1 - P_{\mathrm{out}}) \int_0^{x_{\mathrm{th}}} \frac{f_{\mathcal{D}}(x)x}{F_{\mathcal{D}}(x_{\mathrm{th}})}\mathrm{d}x + P_{\mathrm{out}} \int_{x_{\mathrm{th}}}^{d} \frac{f_{\mathcal{D}}(x)x}{1 - F_{\mathcal{D}}(x_{\mathrm{th}})}\mathrm{d}x, \tag{4.37}$$

where $\frac{f_{\mathcal{D}}(x)}{F_{\mathcal{D}}(x_{\mathrm{th}})}$ and $\frac{f_{\mathcal{D}}(x)}{1-F_{\mathcal{D}}(x_{\mathrm{th}})}$ are the normalized truncated PDFs of $\mathcal{D}_k^n$ in the corresponding intervals $[0, x_{\mathrm{th}})$ and $[x_{\mathrm{th}}, d]$, satisfying

$$\int_0^{x_{\mathrm{th}}} \frac{f_{\mathcal{D}}(x)\mathrm{d}x}{F_{\mathcal{D}}(x_{\mathrm{th}})} = 1 \quad \text{and} \quad \int_{x_{\mathrm{th}}}^{d} \frac{f_{\mathcal{D}}(x)\mathrm{d}x}{1 - F_{\mathcal{D}}(x_{\mathrm{th}})} = 1. \tag{4.38}$$

The first term in (4.37) represents the event where at least one user falls below the threshold and reports '1' to the transmitter. The second term denotes a scheduling outage, where all the users exceed the threshold and report '0'.

4.5.2 Achievable DoF and User Scaling Law When $d = 1$

For a given N, P_{out} is uniquely determined by the choice of the threshold x_{th}. We intend to find the optimal x_{th}, such that (4.37) is minimized. The function is convex in the range of $[0,1]$. Thus, $\mathbb{E}[\mathcal{D}_k^{n^\dagger}]$ has an unique minimum within the interval $[0,1]$. To find the minimum value and the corresponding threshold, we need to solve the equation $\frac{\partial \mathbb{E}[\mathcal{D}_k^{n^\dagger}]}{\partial x_{\text{th}}} = 0$. For $d = 1$, according to (4.21) we have $F_{\mathcal{D}}(x) = x$ and $f_{\mathcal{D}}(x) = 1$ in the interval $[0,1]$. The expected metric value $\mathbb{E}[\mathcal{D}_k^{n^\dagger}]$ in (4.37) can be simplified as

$$\begin{aligned} D_k(x_{\text{th}}) &= \mathbb{E}[\mathcal{D}_k^{n^\dagger}] \\ &= (1 - P_{\text{out}}) \int_0^{x_{\text{th}}} \frac{x\mathrm{d}x}{x_{\text{th}}} + P_{\text{out}} \frac{\int_{x_{\text{th}}}^1 x\mathrm{d}x}{1 - x_{\text{th}}} \\ &= (1 - (1 - x_{\text{th}})^N) \frac{x_{\text{th}}}{2} + (1 - x_{\text{th}})^N (\frac{1 + x_{\text{th}}}{2}). \end{aligned} \tag{4.39}$$

The optimal x_{th} which minimizes $\mathbb{E}[\mathcal{D}_k^{n^\dagger}]$ can be found by solving $\frac{\partial D_k(x_{\text{th}})}{\partial x_{\text{th}}} = 0$, i.e. $-N(1 - x_{\text{th}})^{N-1} + 1 = 0$. Thus we have the optimal threshold

$$\hat{x}_{\text{th}} = 1 - (\frac{1}{N})^{\frac{1}{N-1}}. \tag{4.40}$$

Applying $\hat{x}_{\text{th}}$ to (4.39), the minimum of $D_k(x_{\text{th}})$ can be written as a function of N as

$$D_k(\hat{x}_{\text{th}}) = \frac{1}{2}\left(\frac{1}{N}\right)^{\frac{N}{N-1}} - \frac{1}{2}\left(\frac{1}{N}\right)^{\frac{1}{N-1}} + \frac{1}{2}. \tag{4.41}$$

This leads us to the following lemma, which will then be used for the proof of the achievable DoF.

Lemma 1. When the number of users N goes to infinity, i.e. $N \to \infty$, $D_k(\hat{x}_{\text{th}})$ is asymptotically equivalent to $\frac{\log N}{2N}$, such that

$$\lim_{K \to \infty} \frac{D_k(\hat{x}_{\text{th}})}{\frac{\log N}{2N}} = 1. \tag{4.42}$$

Proof. According to (4.41), the left hand side of (4.42) can be written as

$$\begin{aligned} &\lim_{N \to \infty} \frac{\left(\frac{1}{N}\right)^{\frac{N}{N-1}} - \left(\frac{1}{N}\right)^{\frac{1}{N-1}} + 1}{\frac{\log K}{K}} &(4.43)\\ &= \lim_{N \to \infty} \frac{\left(\frac{1}{N}\right) - \left(\frac{1}{N}\right)^{\frac{1}{N}} + 1}{\frac{\log N}{N}} &(4.44)\\ &= \lim_{M \to 0} \frac{M^M(\log M + 1) - 1}{\log M + 1} &(4.45)\\ &= \lim_{M \to 0} M^M - \lim_{M \to 0} \frac{1}{\log M + 1} &(4.46)\\ &= 1 \end{aligned}$$

where (4.45) is obtained by letting $M = 1/N$ and applying the L'Hôpital's rule. Thus, the proof is complete. □

Theorem 3. For $d = 1$, if the number of users is scaled as $N \propto P^{d'}$, 1-bit feedback per user is able to achieve a DoF $d' \in [0, 1]$ per transmitter if the threshold is optimally chosen according to (4.40).

Proof. The achievable DoF of transmitter k using OIA can be expressed as $1 - d_{\text{loss}}$. If $N \propto P^{d'}$, the DoF loss term can be written as

$$
\begin{aligned}
d_{\text{loss}} &= \lim_{P\to\infty} \frac{\mathbb{E}[R_{\text{loss}}{}_k^{n^\dagger}]}{\log_2 P} && (4.47)\\
&\leq \lim_{P\to\infty} \frac{\log_2\left(1 + PD_k\left(\hat{x}_{\text{th}}\right)\right)}{\log_2 P} && (4.48)\\
&= \lim_{P\to\infty} \frac{\log_2\left(PD_k\left(\hat{x}_{\text{th}}\right)\right)}{\log_2 P} && (4.49)\\
&= \lim_{P\to\infty} \frac{\log_2\left(P \cdot \frac{\log N}{2N}\right)}{\log_2 P} && (4.50)\\
&= (1 - d') + \lim_{P\to\infty} \frac{1}{\log P + O(1)} && (4.51)\\
&= (1 - d'). && (4.52)
\end{aligned}
$$

The inequality (4.48) is obtained by using the upper bound in (4.16) and invoking (4.41). Equality (4.50) is due to the asymptotic equivalence in Lemma 1. Equality (4.51) is obtained using the relationship $N \propto P^{d'}$ and the L'Hôpital's rule. Therefore, the DoF d' is obtained at each transmitter. □

Remark 3. Compared to conventional OIA in [18], the user scaling law achieving DoF d' remains the same. The second term in (4.51) does not exist for conventional OIA. However, it goes to 0 when $P \to \infty$, and thus does not change the DoF. Therefore, 1-bit feedback neither degrades the performance in terms of DoF nor requires more users to achieve the same DoF.

4.5.3 Achievable DoF and User Scaling Law When $d > 1$

Now we want to generalize the result to any d values. However, for $d > 1$, a closed-form solution does not exist. In this section, we will base our investigation on asymptotic analysis. To ease the notation, we drop the dependence of $c_{N_{\text{R}},d}$ on d and let

$N_{\mathrm{R}} = 2d$. First, we simplify (4.37) using the following upper bound

$$
\begin{aligned}
&\mathbb{E}[\mathcal{D}_k^{n^\dagger}] \\
&= (1 - P_{\mathrm{out}}) \int_0^{x_{\mathrm{th}}} \frac{f_{\mathcal{D}}(x)x}{F_{\mathcal{D}}(x_{\mathrm{th}})} \mathrm{d}x + P_{\mathrm{out}} \int_{x_{\mathrm{th}}}^{d} \frac{f_{\mathcal{D}}(x)x}{1 - F_{\mathcal{D}}(x_{\mathrm{th}})} \mathrm{d}x \\
&\leq (1 - P_{\mathrm{out}})\, x_{\mathrm{th}} + P_{\mathrm{out}} d && (4.53) \\
&= x_{\mathrm{th}} + (d - x_{\mathrm{th}})(1 - F_{\mathcal{D}}(x_{\mathrm{th}}))^N && (4.54) \\
&= x_{\mathrm{th}} + (d - x_{\mathrm{th}})(1 - c{x_{\mathrm{th}}}^{d^2})^N && (4.55)
\end{aligned}
$$

where (4.53) is obtained by taking the upper limit of the integration. To find the minimum value and the corresponding threshold, we need to solve the partial derivative of (4.55) with respect to x_{th}, i.e.

$$
1 - (1 - c{x_{\mathrm{th}}}^{d^2})^N - cNd^2(d - x_{\mathrm{th}}){x_{\mathrm{th}}}^{d^2-1}(1 - c{x_{\mathrm{th}}}^{d^2})^{N-1} = 0. \tag{4.56}
$$

where an explicit solution does not exist for $d > 1$ to the best of our knowledge.

Therefore, instead of an explicit solution, we will find an asymptotically close solution. We simplify equation (4.55) by letting $y = c{x_{\mathrm{th}}}^{d^2}$, i.e.

$$
\begin{aligned}
\mathbb{E}[\mathcal{D}_k^{n^\dagger}] &\leq x_{\mathrm{th}} + (d - x_{\mathrm{th}})(1 - c{x_{\mathrm{th}}}^{d^2})^N \\
&= \left(\frac{y}{c}\right)^{\frac{1}{d^2}} + \left(d - \left(\frac{y}{c}\right)^{\frac{1}{d^2}}\right)(1 - y)^N && (4.57) \\
&\leq (\frac{y}{c})^{\frac{1}{d^2}} + d \sum_{a=0}^{\infty} (-1)^a \binom{N}{a} y^a && (4.58)
\end{aligned}
$$

where (4.58) is obtained by neglecting $(\frac{y}{c})^{\frac{1}{d^2}}$ in the second term and applying the Maclaurin series expansion to the following binomial function

$$
\begin{aligned}
&(1 - y)^N \\
&= 1 - Ny + \frac{N(N-1)y^2}{2!} \cdots + (-1)^n \frac{N \cdots (N - a + 1)y^a}{a!} \\
&= \sum_{a=0}^{\infty} (-1)^a \binom{N}{a} y^a. && (4.59)
\end{aligned}
$$

To proceed our proof, we give the following lemma.

Lemma 2. When the number of users N goes to infinity, i.e. $N \to \infty$, the binomial coefficient

$$
\binom{N}{a} = \frac{N^a}{a!}\left(1 + O\left(\frac{1}{N}\right)\right). \tag{4.60}
$$

Proof. By definition of $\binom{N}{a}$, we have

$$\binom{N}{a} = \frac{N!}{a!(N-a)!} = \frac{(N-a+1)(N-a+2)\cdots N}{a!} \tag{4.61}$$

The numerator in (4.61) can be expanded as

$$(N-a+1)(N-a-1)...N = N^a + c_1(a)N^{a-1} + c_2(a)N^{a-2} + \cdots + c_a(a) \tag{4.62}$$

where $c_i(a)$ are polynomial functions dependent only on N. When $N \to \infty$, we can extract N^a to obtain

$$N^a(1 + \frac{c_1(a)}{N} + \frac{c_2(a)}{N^2} + \cdots + \frac{c_a(a)}{N^a}) = N^a\left(1 + O\left(\frac{1}{N}\right)\right)$$

and thus $\binom{N}{a} = \frac{N^a}{a!}\left(1 + O\left(\frac{1}{N}\right)\right)$. □

Therefore, when $N \to \infty$, (4.58) can be written as

$$\begin{aligned}
\mathbb{E}[\mathcal{D}_k^{n^\dagger}] &\le \left(\frac{y}{c}\right)^{\frac{1}{d^2}} + d\sum_{a=0}^{\infty}(-1)^n\binom{N}{a}y^a \\
&= \left(\frac{y}{c}\right)^{\frac{1}{d^2}} + d\left(1 + O\left(\frac{1}{N}\right)\right)\sum_{a=0}^{\infty}(-1)^a\frac{N^a y^a}{a!} && (4.63)\\
&= \left(\frac{y}{c}\right)^{\frac{1}{d^2}} + d\left(1 + O\left(\frac{1}{N}\right)\right)e^{-Ny} && (4.64)\\
&= \underbrace{\left(\frac{y}{c}\right)^{\frac{1}{d^2}} + de^{-Ny}}_{\tilde{D}_k(y)} && (4.65)
\end{aligned}$$

where (4.63) follows from lemma 2. Equality (4.64) is obtained by utilizing the Maclaurin series expansion of the exponential function

$$e^{-Ny} = 1 - Ny + \frac{N^2y^2}{2!} - \frac{N^3y^3}{3!} + \cdots + (-1)^n\frac{N^a y^a}{a!} = \sum_{a=0}^{\infty}(-1)^a\frac{N^a y^a}{a!}. \tag{4.66}$$

Equality (4.65) is obtained by neglecting $O\left(\frac{1}{N}\right)$ due to the fact $N \to \infty$. We define $\tilde{D}_k(y)$ as the upper bound obtained in (4.65). The y which minimizes $\tilde{D}_k(y)$ is the solution to

$$\frac{\partial \tilde{D}_k(y)}{\partial y} = \frac{1}{d^2}\left(\frac{y}{c}\right)^{\left(\frac{1}{d^2}-1\right)} - dNe^{-Ny} = 0. \tag{4.67}$$

For (4.67), the real solutions should exist in $(0, \infty)$, which can be found by numerical approximation. However, for general d (expect for $d = 1$), an explicit solution is still mathematically intractable. The solver can be written in the form of the Lambert W function [94], which is a set of functions satisfying $W(z)e^{W(z)} = z$. To this end, we first rewrite (4.67) as

$$\frac{N}{\alpha} y e^{\frac{N}{\alpha} y} = \frac{Nc\left(d^3 N\right)^{\frac{1}{\alpha}}}{\alpha} \tag{4.68}$$

where $\alpha = \frac{1}{d^2} - 1$. The possible real solutions to this equation are given by

$$\hat{y} = \frac{\alpha \cdot W_\zeta\left(\frac{Nc\left(d^3 N\right)^{\frac{1}{\alpha}}}{\alpha}\right)}{N}, \zeta \in \{0, -1\}, \tag{4.69}$$

where the function $W_0(\cdot)$ and $W_{-1}(\cdot)$ are two real branches of the Lambert W function defined in the intervals $[-\frac{1}{e}, \infty)$ and $[-\frac{1}{e}, 0)$, corresponding to the maximum and minimum value of $\tilde{D}_k(y)$. We are interested in the minimum of $\tilde{D}_k(y)$ when $\zeta = -1$. The Lambert W function $W_\zeta(z)$ is asymptotic to [94]

$$W_\zeta(z) = \log z + 2\pi i\zeta - \log\left(\log z + 2\pi i\zeta\right) + o(1). \tag{4.70}$$

Therefore, for $\zeta = -1$ and large $N \to \infty$, we arrive at an asymptomatic solution for $\hat{y}$, which is given by

$$\hat{y} = \frac{\alpha}{N}\left(\log\left(\frac{Nc\left(d^3N\right)^{\frac{1}{\alpha}}}{\alpha}\right) - 2\pi i - \log\left(\log\left(\frac{Nc\left(d^3N\right)^{\frac{1}{\alpha}}}{\alpha}\right) - 2\pi i\right) + o(1)\right) \tag{4.71}$$

$$= \frac{\alpha}{N}\left(\underbrace{\log\left(\frac{-Nc\left(d^3N\right)^{\frac{1}{\alpha}}}{\alpha}\right)}_{w(N)} - \log\log\left(\frac{-Nc\left(d^3N\right)^{\frac{1}{\alpha}}}{\alpha}\right) + o(1)\right) \tag{4.72}$$

$$= \frac{\alpha}{N}\left(w\left(N\right) - o\left(w\left(N\right)\right) + o(1)\right) \tag{4.73}$$

$$= \frac{1}{N}\left(\underbrace{(\alpha+1)}_{A}\log N + \underbrace{\log\left(d^3c^{\alpha}\right) - \alpha\log\left(-\alpha\right) - \alpha o\left(w(N)\right) + \alpha o(1)}_{B}\right) \tag{4.74}$$

$$= \frac{1}{N}\left(A\log N + B\right) \tag{4.75}$$

where $w(N) = \log\left(\frac{-Nc\left(d^3N\right)^{\frac{1}{\alpha}}}{\alpha}\right)$, $A = \alpha + 1$ and $B = \log\left(d^3c^{\alpha}\right) - \alpha\log\left(-\alpha\right) - \alpha o\left(w(N)\right) + \alpha o(1)$. Equality (4.72) is obtained due to natural logarithm function of a negative value $m < 0$ is $\log m = \log(-m) + 2\pi i$. Equality (4.73) follows from the fact $\lim_{N\to\infty} = \frac{\log(w(N))}{w(N)} = 0$. Therefore, the corresponding choice of a threshold that minimizes $\tilde{D}_k(y)$ can be calculated as

$$\begin{aligned}\hat{x}_{\text{th}} &= \left(\frac{\hat{y}}{c}\right)^{\frac{1}{d^2}} \\ &= \left(\frac{A\log N + B}{cN}\right)^{\frac{1}{d^2}}.\end{aligned} \tag{4.76}$$

Using this result, we arrive at the following lemma, which will be used for the calculation of the achievable DoF.

Lemma 3. If we choose the threshold $\hat{x}_{\text{th}}$ such that $\hat{y} = \frac{1}{N}\left(A\log N + B\right)$, the upper bound $\tilde{D}_k(\hat{y})$ in (4.65) is asymptotically equivalent to $\left(\frac{A\log N}{cN}\right)^{\frac{1}{d^2}}$ when the number of users $N \to \infty$, such that

$$\lim_{K\to\infty}\frac{\tilde{D}_k(\hat{y})}{\left(\frac{A\log N}{cN}\right)^{\frac{1}{d^2}}} = 1. \tag{4.77}$$

Proof. Plugging (4.75) into the left hand side of (4.77), we have

$$\lim_{K\to\infty} \frac{\left(\frac{\hat{y}}{c}\right)^{\frac{1}{d^2}} + de^{-N\hat{y}}}{\left(\frac{A\log N}{cN}\right)^{\frac{1}{d^2}}} \tag{4.78}$$

$$= \lim_{K\to\infty} \frac{\left(\frac{A\log N+B}{cN}\right)^{\frac{1}{d^2}}}{\left(\frac{A\log N}{cN}\right)^{\frac{1}{d^2}}} + \lim_{N\to\infty} \frac{de^{-B}N^{\frac{1}{d^2}-A}}{\left(\frac{A\log N}{c}\right)^{\frac{1}{d^2}}} \tag{4.79}$$

$$= 1.$$

The second term of (4.79) equals to zero due to $\frac{1}{d^2} - A = 0$, so the numerator is a constant and the denominator goes to infinity. Thus, the proof is complete. □

Theorem 4. If the number of users is scaled as $N \propto P^{dd'}$, the feedback of only 1-bit per user is able to achieve the DoF $d' \in [0, d]$ per transmitter if the threshold $\hat{x}_{\text{th}}$ is chosen such that

$$c\hat{x}_{\text{th}}^{d^2} = \frac{1}{N}\left(A\log N + B\right). \tag{4.80}$$

Proof. The proof is similar to the proof of Theorem 3. The achievable DoF of transmitter k using OIA can be expressed as $d - d_{\text{loss}}$. If $N \propto P^{dd'}$, the DoF loss term can be written as

$$d_{\text{loss}} = d \cdot \lim_{P\to\infty} \frac{\mathbb{E}[R_{\text{loss}}{}_k^{n^\dagger}]}{\log_2 P}$$

$$\leq d \cdot \lim_{P\to\infty} \frac{\log_2\left(1 + \frac{P}{d}\tilde{D}_k(\hat{y})\right)}{\log_2 P} \tag{4.81}$$

$$= d \cdot \lim_{P\to\infty} \frac{\log_2\left(1 + \frac{P}{d}\left(\frac{A\log N}{cN}\right)^{\frac{1}{d^2}}\right)}{\log_2 P} \tag{4.82}$$

$$= d \cdot \lim_{P\to\infty} \frac{\log_2\left(\frac{P}{dN^{\frac{1}{d^2}}}\right) + \frac{1}{d^2}\log_2\left(\frac{A\log N}{c}\right)}{\log_2 P} \tag{4.83}$$

$$= (d - d') + \lim_{P\to\infty} \frac{1}{\log P + O(1)} \tag{4.84}$$

$$= (d - d'). \tag{4.85}$$

The inequality (4.81) is obtained by using the upper bound of (4.65). Equality (4.82) follows from the asymptotic equivalence proved in Lemma 3. Equality (4.84) is obtained using the relationship $N \propto P^{dd'}$ and the L'Hôpital's rule. Therefore, DoF d' can be achieved at each transmitter. □

Remark 4. The achieved DoF is independent of the specific value of B. Therefore, theorem 4 is valid for all $B \in \mathbb{R}$. For $d = 1$, the optimal threshold obtained in (4.40) is a special case of the above result $\hat{x}_{\mathrm{th}} = \hat{y} = \frac{1}{N}(A \log N + B)$ when $A = 1$. The asymptotic equivalence can be shown as follows

$$\lim_{N\to\infty} \frac{\frac{1}{N}(\log N + B)}{1 - \left(\frac{1}{N}\right)^{\frac{1}{N-1}}} = \lim_{M\to 0} \frac{-M \log M}{1 - M^M} \tag{4.86}$$

$$= \lim_{M\to 0} \frac{1}{M^M} \tag{4.87}$$

$$= 1$$

where $M = \frac{1}{N}$ replaces N for simplicity. Equality (4.87) follows from the L'Hôpital's rule.

Theorem 5. When the transmit power is a finite value and the number of users tends to infinity i.e. $P = O(1)$ and $N \to \infty$, OIA with 1-bit feedback and OIA with perfect real-valued feedback achieve the same rate.

Proof. When $P = O(1)$ and $N \to \infty$, the achievable rate of OIA with perfect real-valued feedback becomes the ergodic capacity of the $d \times d$ point-to-point MIMO system without interference [18]. To complete our proof, we just need to show that OIA with 1-bit feedback achieves the same ergodic capacity of the $d \times d$ point-to-point MIMO system without interference. Therefore, we proof as follows.

When $N \to \infty$, the rate loss in (4.16) can be written as

$$\mathbb{E}[R_{\mathrm{loss}_k}^{n^\dagger}] \le d \cdot \log_2 \left(1 + \frac{P}{d} \cdot \tilde{D}_k(y)\right) \tag{4.88}$$

using the upper bound obtained in (4.65). If we choose the threshold $\hat{x}_{\mathrm{th}}$ such that $\hat{y} = \frac{1}{N}(A \log N + B)$, we have

$$\lim_{N\to\infty} \tilde{D}_k(\hat{y}) = \lim_{N\to\infty} \left(\frac{A \log N}{cN}\right)^{\frac{1}{d^2}} \tag{4.89}$$

$$= \left(\lim_{N\to\infty} \frac{A}{cN}\right)^{\frac{1}{d^2}} \tag{4.90}$$

$$= 0$$

where (4.89) follows from lemma 3 and (4.90) is due to L'Hôpital's rule. Correspondingly, the rate loss term $\mathbb{E}[R_{\mathrm{loss}_k}^{n^\dagger}]$ goes to zero due to finite P. Therefore, when the number of users $N \to \infty$, we can see from (4.4) that OIA with 1-bit feedback achieves the interference-free rate at the selected user, i.e.

$$\mathbb{E}[R_k^{n^\dagger}] = \mathbb{E}\left[\log_2\det\left(\mathbf{I} + \underbrace{\mathbf{U}_k^{n^\dagger \mathrm{H}} \mathbf{H}_{k,k}^{n^\dagger}}_{\bar{\mathbf{H}}_{k,k}^{n^\dagger}} \underbrace{\mathbf{H}_{k,k}^{n^\dagger \mathrm{H}} \mathbf{U}_k^{n^\dagger}}_{\bar{\mathbf{H}}_{k,k}^{n^\dagger \mathrm{H}}}\right)\right] \tag{4.91}$$

where $\bar{\mathbf{H}}_{k,k}^{n^\dagger} = \mathbf{U}_k^{n^\dagger \mathrm{H}} \mathbf{H}_{k,k}^{n^\dagger}$ is a $d \times d$ matrix. Every element of $\bar{\mathbf{H}}_{k,k}^{n^\dagger}$ is an i.i.d. symmetric complex Gaussian random variable with zero mean and unit variance. This is due to the fact that the $N_\mathrm{R} \times d$ truncated unitary matrix $\mathbf{U}_k^{n^\dagger}$ is independent on $\mathbf{H}_{k,k}^{n^\dagger}$. Therefore, the rate achieved in (4.91) becomes the ergodic capacity of the $d \times d$ point-to-point MIMO system. This also completes our proof. □

4.5.4 Simulations Results

In this section, we provide numerical results of the sum rate and the threshold choices of OIA using 1-bit feedback.

Fig. 4.7 shows the achievable sum rate versus SNR of OIA with perfect real-valued feedback and OIA with 1-bit feedback, for $N_\mathrm{R} = 2$, $d = 1$ and the number of users $N = \lceil P \rceil$. We include also the sum rate achieved by closed-form IA in a 3-user 2×2 MIMO interference channel. The threshold of our feedback scheme is calculated according to (4.40). We can see that OIA with 1-bit feedback achieves a slightly lower rate than OIA with perfect feedback. At 30 dB SNR, it can achieve 90% of the sum rate obtained by perfect feedback OIA. Importantly, OIA with 1-bit feedback is able to capture the slope and achieve the DoF $d = 1$ (see the reference line in Fig. 4.7).

The feedback mechanism can be designed in a way where any user whose distance measure is above the prescribed threshold will stay silent, and only eligible users will attempt to feedback [95]. In such a mechanism, since only the eligible users feed back information, the feedback must consist of user identity and be performed on a shared random access channel, e.g., using a contention-based approach [95]. It should be noted that any feedback information cannot be decoded when more than two users collide simultaneously using the same feedback resource. Therefore, the number of users that compete for the same feedback resource will have an impact on the successful transmission of the feedback information. We can establish the average number of eligible users as follows

$$N_\mathrm{bits} = N F_\mathcal{D}\left(x_\mathrm{th}\right). \tag{4.92}$$

Fig. 4.8 also shows the number of eligible users per cell when the total number of users $N = \lceil P \rceil$. It can be seen that the average number of eligible users is almost a

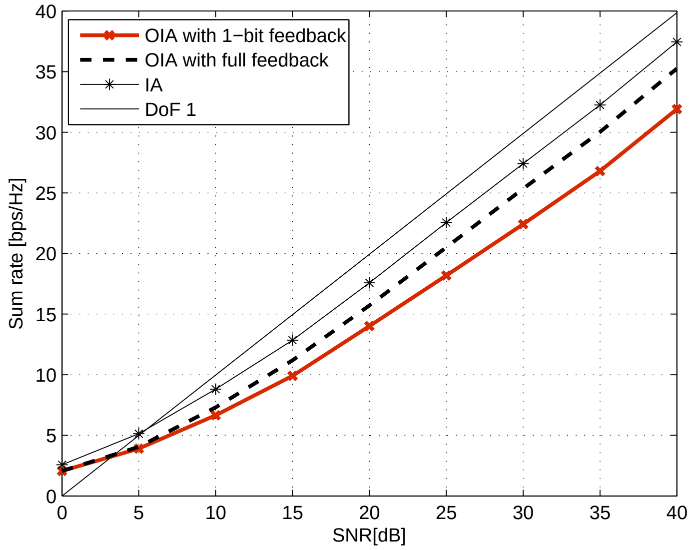

Figure 4.7: Achievable sum rate for $N_{\mathrm{R}} = 2$, $d = 1$. The number of users $N = \lceil P \rceil$ for OIA.

linear function with SNR (in dB) and the average number of eligible users at 30 dB is less than 1% of the total number of users. Therefore, the small number of eligible users may ease the design of a contention-based feedback protocol.

Fig. 4.9 compares the threshold as a function of the number of users N for $N_{\mathrm{R}} = 4$, $d = 2$. The thresholds are obtained by numerical minimization of (4.55), (4.69) with $\zeta = -1$ and the asymptotic expression $\frac{A \log N}{N}$ as mentioned in *Remark* 4. The thresholds obtained by the numerical approach and by (4.69) are very close, even for a small number of users N. The asymptotic threshold $\frac{A \log N}{N}$ is smaller than the others since we neglect B in (4.75). However, B has no impact on the achieved DoF as explained in *Remark* 4. It can be seen that these thresholds are getting closer to each other as N increases. These results validate the calculation of the thresholds.

Fig. 4.10 presents the sum rate versus SNR of OIA with perfect feedback and OIA with 1-bit feedback, for $N_{\mathrm{R}} = 4$, $d = 2$ and the number of users $N \in \{10, 50, 100\}$. The number of users does not scale with SNR, thus the sum rates saturate as SNR increases. With the increase of number of users, a higher rate is achieved. Importantly, 1-bit feedback promises about 90% of the rate achieved by OIA with perfect feedback.

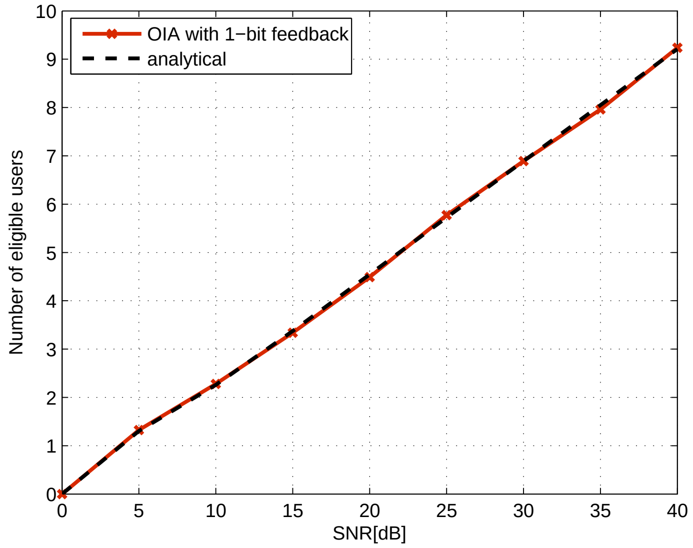

Figure 4.8: The average number of eligible users for $N_{\mathrm{R}} = 2$, $d = 1$ and $N = \lceil P \rceil$.

4.6 Comparison of OIA AND IA with Limited Feedback

OIA achieves interference alignment by proper user selection. With the help of our proposed 1-bit quantizer, each user feeds back just 1 bit. Therefore, the relationship between the number of users and the amount of feedback can be established. On the other hand, IA requires CSI feedback at the transmitters to align the interference signals. The CSI is usually obtained by channel quantization on the Grassmannian manifold, where the index of the selected codeword is fed back to the transmitters. Due to the fact that the capacity of the feedback channel is usually very limited, it would be interesting to have a comparison of OIA and IA using the same amount of feedback. The work in [96] partially addressed this issue and compared the performance OIA and limited feedback IA. However, a comparison under the same amount of feedback has not been done since no limited feedback scheme was proposed by prior works for OIA to the best of our knowledge. In this section, we will present the comparison in terms of complexity and achievable rate.

We quantify and compare the computational complexity of OIA and IA in terms of number of floating point operations (FLOPs). We will pay particular attention to the quantization process. One FLOP is one floating point operation, which corresponds to a real addition, multiplication, or division [97]. A complex addition and multiplication require 2 FLOPs and 6 FLOPs, respectively. For a complex-valued

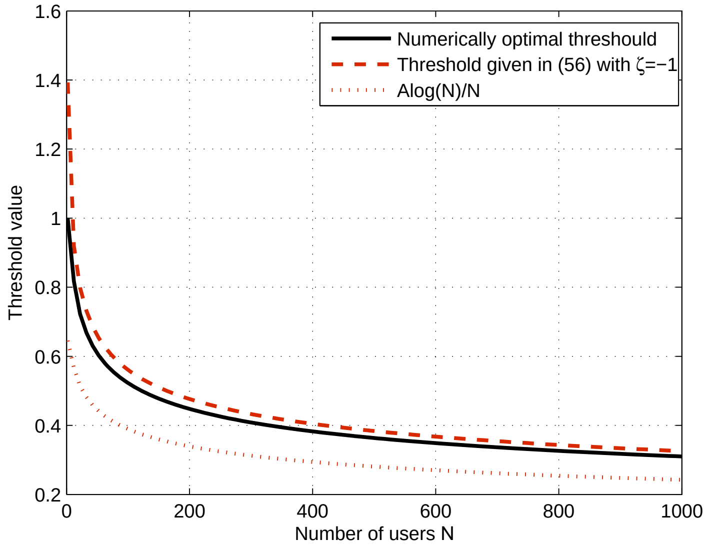

Figure 4.9: Comparison of the threshold obtained by numerical minimization of (4.55), (4.69) and the asymptotic solution $\frac{A \log N}{N}$ for $N_{\mathrm{R}} = 4, d = 2$.

matrix $\mathbf{A} \in \mathbb{C}^{m \times n}$ $(m \geq n)$, the FLOP counts, denoted by Ξ, of some basic matrix operations are given as follows.

- Frobenius norm of $\|\mathbf{A}\|_{\mathrm{F}}$: $\Xi_{\mathrm{F}}(m, n) = 4mn$
- Gram-Schmidt orthogonalization (GSO) of $\mathbf{A}$: $\Xi_{\mathrm{GSO}}(m, n) = 8n^2m - 2mn$
- Matrix multiplication of $\mathbf{A}\mathbf{A}^{\mathrm{H}}$: $\Xi_{\otimes}(m, n) = 8n^2m - 2mn$

For OIA, each user needs to calculate the chordal distance between two $N_{\mathrm{R}} \times d$ interference channels. According to (4.8), the calculation of the chordal distance requires two GSOs to calculate the orthonormal bases of the two interference channels, two matrix multiplications of the truncated unitary matrices, a matrix addition of two truncated unitary matrices and a Frobenius norm operation. We ignore the scalar operations. Therefore, the total FLOPs per cell are counted as

$$\begin{aligned} &\Xi_{\mathrm{OIA-1bit}} \\ &= N_{\mathrm{bits}}(2\Xi_{\mathrm{GSO}}(N_{\mathrm{R}}, d) + 2\Xi_{\otimes}(N_{\mathrm{R}}, d) + 2N_{\mathrm{R}}d + \Xi_{\mathrm{F}}(N_{\mathrm{R}}, d)) \\ &= N_{\mathrm{bits}}(32N_{\mathrm{R}}d^2 - 2N_{\mathrm{R}}d). \end{aligned} \tag{4.93}$$

where $N_{\mathrm{bits}} = N$ is the number of feedback bits since each user feeds back 1 bit.

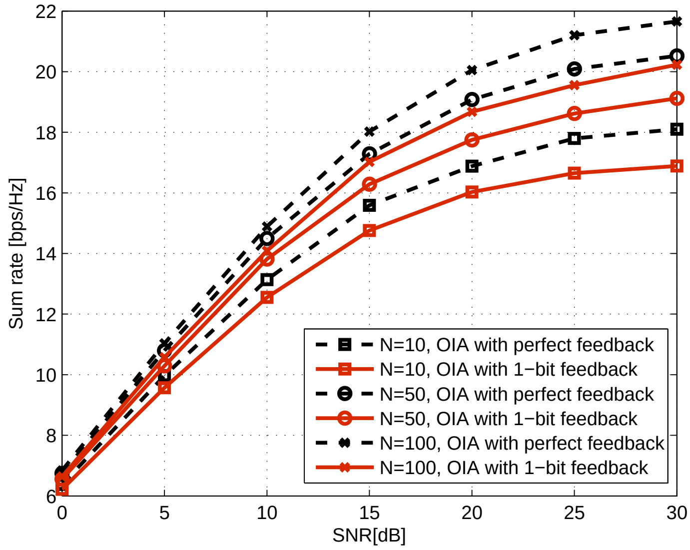

Figure 4.10: Achievable sum rate for $N_{\mathrm{R}} = 4$, $d = 2$. The number of users $N \in \{10, 50, 100\}$ (for the curves from bottom up).

For IA with limited feedback, the squared distance is used for the selection of the quantized channel matrix (see Section 2.4.2). Thus, $2^{N_{\mathrm{bits}}}$ squared distance calculations will be performed in order to find the codeword. The squared distance calculates twice the chordal distance between two $N_{\mathrm{R}}N_{\mathrm{T}} \times 1$ vectors. Therefore, the total FLOP counts are given by

$$\Xi_{\mathrm{IA-joint}} = 2^{N_{\mathrm{bits}}}(64N_{\mathrm{R}}N_{\mathrm{T}} - 4N_{\mathrm{R}}N_{\mathrm{T}}). \tag{4.94}$$

Since the joint quantization over the composite Grassmannian manifold yields a high complexity for decoding, then the quantizations of $\bar{\mathbf{h}}_{k,\ell}$ (defined in Section 2.4.2) over individual Grassmannian manifold $\mathcal{G}_{N_{\mathrm{R}}N_{\mathrm{T}},1}(\mathbb{C})$ could be used to reduce the complexity at the expense of lower quantization resolution. Assuming equal division of the total N_{bits} quantization bits, the total FLOP counts of individual quantization are given by

$$\Xi_{\mathrm{IA-indv}} = 2^{\frac{N_{\mathrm{bits}}}{2}}(64N_{\mathrm{R}}N_{\mathrm{T}} - 4N_{\mathrm{R}}N_{\mathrm{T}}). \tag{4.95}$$

The computational complexity of OIA and IA versus the number of feedback bits is given in Fig. 4.11. The codebook for IA with joint quantization contains $2^{N_{\mathrm{bits}}}$ codewords, which results in an exponentially increased FLOP counts. Individual quantization reduces the exponent to $\frac{N_{\mathrm{bits}}}{2}$. On the contrary, the complexity of OIA increases linearly with N_{bits}.

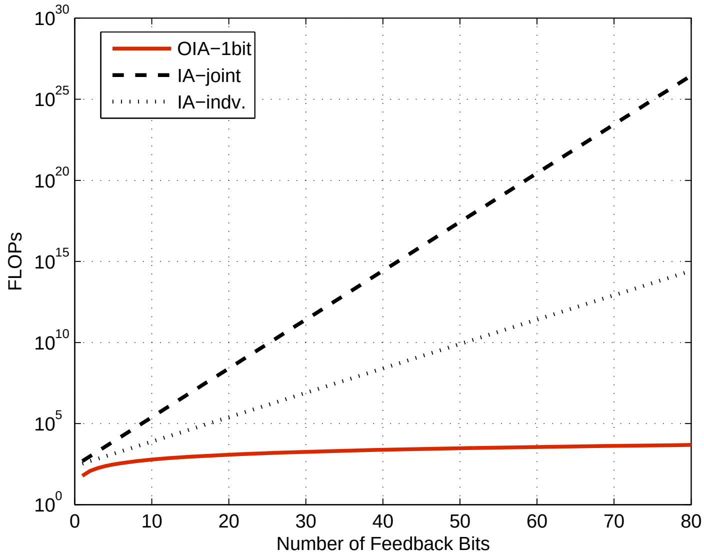

Figure 4.11: Feedback Complexity per cell of OIA and IA for $N_{\mathrm{R}} = 2$, $d = 1$ ($N_{\mathrm{T}} = 2$ for IA). The FLOP counts of OIA sum over all N users in a cell.

Fig. 4.12 presents the sum rate of OIA with 1-bit feedback and IA with individual quantization. To satisfy the feasibility condition, we choose $N_{\mathrm{T}} = 2$ for IA. The codewords for IA are generated through random vector quantization (RVQ). In order to enable the performance analysis with exponentially growing codebook, we replace the RVQ process by a statistical model of the quantization error using random perturbations [57, Sec. VI.B], which has shown to be a good approximation of the quantization error using RVQ. It can be observed that OIA outperforms IA when the amount of feedback is lower than 30 bits and the rate difference increases with SNR. This is due to the fact that the IA algorithm is highly sensitive to the imperfection of CSI, thus leading to a significant rate loss. At 20 dB SNR with 10 feedback bits per cell, it can be observed that OIA compared to IA increases the sum rate by 100% while reducing the computational complexity by more than one order of magnitude. When the number of feedback bits is larger than 30, IA starts to outperform taking advantage of the accurate CSI provided by the exponentially increased codebook size. However, the performance improvement of IA also comes with an exponentially increased computational complexity and storage, which poses a strong practical limit. From an implementation point of view, OIA with 1-bit feedback provides a better performance in the favorable operation region and enjoys a much lower complexity.

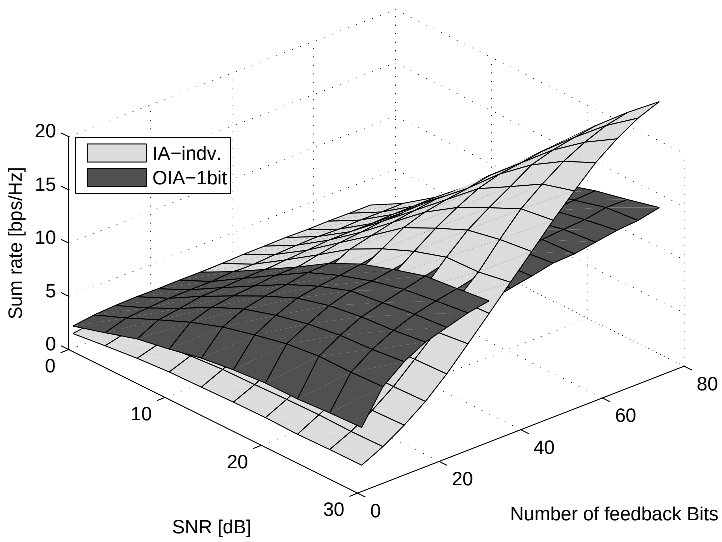

Figure 4.12: Sum rate for $N_{\mathrm{R}} = 2$, $d = 1$ at varying SNRs and the numbers of feedback bits per cell.

Part II

Channel Modeling and Performance Analysis for Cooperative Vehicular Communications

5 Vehicular Channel Modeling using GSCM

The on-board safety systems in today's vehicles mostly rely on sensors, which use visible light or radar for detection. Therefore, these systems are limited in detection range and proximity coverage. Vehicular communication systems based on radio technology promise to increase coverage of location and behavior awareness. The idea is that all vehicles exchange information, e.g., position and speed, with other vehicles periodically via cooperative awareness message (CAM). This might enable new safety-related applications, e.g. cross-traffic assistance and traffic condition warnings, that warn drivers about dangerous situations before they become visible. Among all safety critical applications, the cross-traffic assistance in urban road intersections is one of the most challenging use-cases due to the obstruction of the line of sight (LOS) by surrounding buildings.

In this chapter, we aim at evaluating the communication performance between vehicles at road intersections. There exist a number of studies on traffic safety at road intersections [98–102]. A non-line of sight (NLOS) path-loss model for urban intersections is proposed in [99], and validated in [100]. The measured performance of IEEE 802.11p at intersections is studied in [101] and [102]. However, the measured results are only available at particular positions and speeds. In this chapter, we aim at building up a controlled environment, such that the influences due to different factors, e.g. speed, position and channel estimation techniques, can be decoupled. For this purpose, we first derive a geometry-based stochastic channel model (GSCM) for road intersections by extending the existing highway channel model [3]. Using the proposed GSCM for intersections, we evaluate the communication performance in terms of frame error rate (FER) at various transmitter (TX)/receiver (RX) locations and velocities with three different types of channel estimators. The influence of each factor is analyzed. In order to overcome the low signal-to-noise ratio (SNR) due to NLOS, we propose to deploy a relay at the intersection to enhance the reliability of communications and present the performance evaluation with the aid of a decode-and-forward (DF) relay. We show that a relay at the road intersection can strongly improve the SNR.

5.1 Geometry Based Stochastic Model for Road Intersections

In order to obtain realistic simulation results, we need a channel model that resembles the true propagation conditions. As shown by vehicular radio channel measurements at 5 GHz, the channel impulse response of vehicular channels is mainly composed of: LOS, deterministic scattering, and diffuse scattering. The LOS component contains a strong power if there exists a direct connection between the TX and the RX. The power may drop due to shadowing effects and obstruction of interacting objects. In urban intersection scenarios, diffuse scattering also has a significant contribution to the channel gain. Moreover, the statistical properties of the vehicular channel change over time and therefore the channel is *non-stationary* [70]. For this reason, the commonly used tapped delay line channel model [20] is not suitable for vehicular communications.

To obtain realistic simulation results, we need a non-stationary channel model that resembles the true propagation conditions. Because of that, we use a non-stationary GSCM for road intersections and parameterize it from vehicular measurements [99], [103]. As shown in Fig. 5.1, we generate a typical road crossing scenario, which consists of a moving TX, a moving RX, some mobile and static discrete scatterers (MD and SD) and diffuse scatterers (D) at the two sides of the road. The MD scatterers represent other cars moving on the road, while the SD scatterers represent traffic signs and parked cars. The diffuse scattering wall models buildings, foliage and other objects along the road.

The function that maps the subcarrier index $q \in \{0, \dots, Q-1\}$ into the discrete frequency index is defined as $\varphi(q) = ((q + Q/2 \mod Q) - Q/2)$. The time-variant channel frequency response is generated as

$$
\begin{aligned}
h[m,q] =& \alpha^{(\mathrm{LOS})}(mt_\mathrm{s})\gamma^{(\mathrm{LOS})}(mt_\mathrm{s})\exp[-j2\pi\Delta f\varphi(q)\tau^{(\mathrm{LOS})}(mt_\mathrm{s})]+ \\
& \sum_{\ell=0}^{N_\mathrm{SD}-1} \alpha_\ell^{(\mathrm{SD})}(mt_\mathrm{s})\gamma_\ell^{(\mathrm{SD})}(mt_\mathrm{s})\exp[-j2\pi\Delta f\varphi(q)\tau_\ell^{(\mathrm{SD})}(mt_\mathrm{s})]+ \\
& \sum_{\ell=0}^{N_\mathrm{MD}-1} \alpha_\ell^{(\mathrm{MD})}(mt_\mathrm{s})\gamma_\ell^{(\mathrm{MD})}(mt_\mathrm{s})\exp[-j2\pi\Delta f\varphi(q)\tau_\ell^{(\mathrm{MD})}(mt_\mathrm{s})]+ \\
& \sum_{\ell=0}^{N_\mathrm{D}-1} \alpha_\ell^{(\mathrm{D})}(mt_\mathrm{s})\gamma_\ell^{(\mathrm{D})}(mt_\mathrm{s})\exp[-j2\pi\Delta f\varphi(q)\tau_\ell^{(\mathrm{D})}(mt_\mathrm{s})]
\end{aligned}
\tag{5.1}
$$

where $\gamma_\ell^{(\cdot)}$ denote the complex-valued attenuation coefficients of different paths, which takes into account the effects of path loss, antenna radiation patterns and

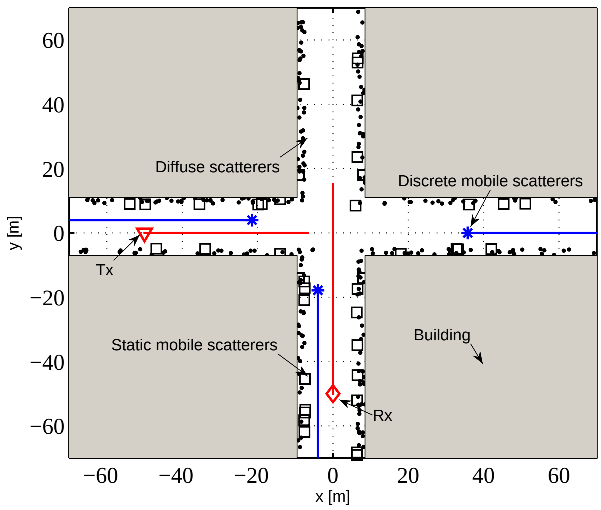

Figure 5.1: Scatterers distribution of the proposed channel model.

large-scale fading, $\tau_\ell^{(\cdot)}$ denote the delays of the paths, and $N_{(\cdot)}$ are the numbers of SD, MD and D scatterers, respectively. The existence of different paths is represented by $\alpha_\ell^{(\cdot)}$, which equals to 0 if the path is blocked by the buildings, and to 1 otherwise.

5.1.1 Validation of the Proposed Model

In order to parametrize and validate the model, we need real-world radio channel measurements. For that, we use the measurements collected in a V2V measurement campaign carried out in an urban crossing environment in Lund city, Sweden [103], shown in Fig. 5.2. The measurements in [103] are collected using a center frequency of 5.6 GHz and a bandwidth of 240 MHz. Therefore, we first need to tune our GSCM to these RF parameters and then proceed with the parametrization and validation of the scattering coefficients. Once the GSCM parameters are set and validated, we re-tune the center frequency and the bandwidth to the ones defined in the 802.11p standard for link-level simulations.

As shown in Fig. 5.2, the investigated intersection consists of two streets, each having a width of 17 m. The distance to the wall on the right side is 6 m. The TX and RX are traveling towards the intersection from 50 m away with a speed of 20 km/h and 30 km/h, respectively. The time duration of each run is 8 s. In Tab. 5.1 we list the modifications of the parameters relative to [3, Tab. 1].

We use two metrics to validate this parametrization: the path-loss and the root

Table 5.1: Modifications to the parameters relative to [3, Tab. 1]

Parameter[1]	LOS	MD	SD	D
G_0[dB]	-5	$-89 + 24n$	$-89 + 24n$	50
n	1.8	$\mathcal{U}[3.5, 5.5]$	$\mathcal{U}[3.5, 5.5]$	5.4
χ[m^{-1}]	-	0.01	0.3	1
W_{DI}[m]	-	-	-	2

[1] The detailed definition of the parameters can be found in [3].

mean square (RMS) delay spread. First, we compare in Fig. 5.3 the normalized path-gain of our simulated channel to the measurement based path-loss model for road intersections derived in [99] using the same data. For simulated channels, we show 20 independent simulation runs. The small scale fading has been removed by averaging the data over the stationary region using the local scattering function estimator [70], whereas the large-scale fading is still preserved, which results in the fluctuations around the curve of the path-loss model. By comparing to the pathloss model, we observe that the distance-dependent decay of the path gain in the NLOS region is greater for intersection scenarios than for highway scenarios [3]. Thus, we modify the distribution of the pathloss exponents to $\mathcal{U}[2, 5.5]$ for discrete scatterers in order to get a better fit.

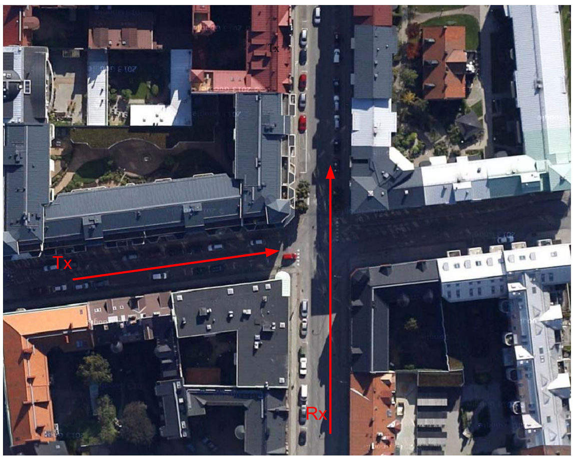

Figure 5.2: Top view of the investigated intersection (N55°42′38″, E13°11′14″) in the city of Lund with the trajectories of TX and RX respectively.

Subsequently, we validate the model using the RMS delay spread. The delay spread has a strong impact on the RX performance [104]. However, in most channel models,

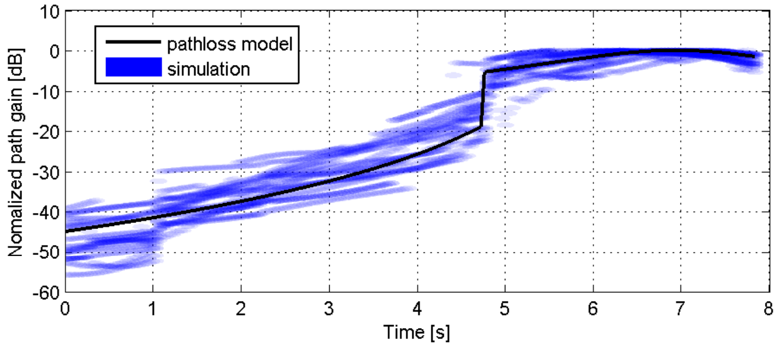

Figure 5.3: Comparison of the normalized path-loss of the measurement based pathloss model and the simulated channel.

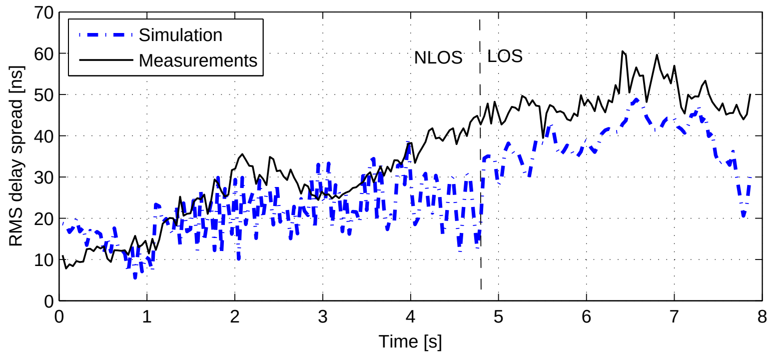

Figure 5.4: Comparison of the RMS delay spread of the measured channel and the simulated channel.

it is assumed to be constant. Non-stationary vehicular channels result in a time-varying delay spread [70]. Thus, we calculate the RMS delay spread, and compare it with the result obtained from channel measurements [103] performed in the city of Lund, Sweden. The selected intersection with the trajectories of the TX and the RX is shown in Fig. 5.2. In Fig. 5.4, it can be observed that the delay spread of the simulated channel fits well with the measurements in the NLOS region and is slightly smaller than the measurements in the LOS region. This is due to the richness of multipath components present near the intersection. In order to maintain a low computational complexity in the GSCM, we only include first-order reflection paths. Nevertheless, the results obtained from simulation and measurements are close enough to consider the model valid.

5.2 Relaying for IEEE 802.11p at Road Intersection

In this section we give a brief overview of the 802.11p standard, and describe the used relaying protocol, channel estimation techniques, and the non-stationary vehicular channel model.

5.2.1 System Description

We implemented a standard compliant IEEE 802.11p physical layer orthogonal frequency division multiplexing (OFDM) transmission chain [104]. The transmission is frame based with frame length M using Q subcarriers. The sampling rate is R_c. A minimum mean square error (MMSE) filter is used as the equalization method. Furthermore, due to the large carrier spacing $\Delta f = R_\mathrm{c}/N$ defined for 802.11p, the inter-carrier interference is small enough to be neglected for the processing at the RX side [71]. Accordingly, the received signal at subcarrier q and time instant m can be written as

$$y[m,q] = h[m,q]x[m,q] + z[m,q], \tag{5.2}$$

where $x[m,q]$ is the transmitted symbol, and $h[m,q]$ denotes the channel at time index m and subcarrier q. Additive complex symmetric Gaussian noise at the receiver is denoted by $z[m,q] \sim \mathcal{CN}(0,\sigma^2)$.

5.2.2 Channel Estimation Techniques

The frame structure of IEEE 802.11p is shown in Fig. 5.5. All 52 subcarriers of the first two OFDM symbols are dedicated to pilots (block pilots). Afterwards, only 4 subcarriers contain pilots throughout the whole frame duration. They are known as comb pilot subcarriers, with subcarrier indices $\mathcal{I}_\mathrm{c} = \{6, 20, 33, 47\}$. In the simulation of this paper, we consider the following three channel estimators.

- Block-type least square (BLS) channel estimator [105]: An estimate of the channel is calculated from the block pilots. This estimation technique is currently used for most commercial off-the-shelf receivers. Let us define the vectors containing the block pilot symbols as

$$\mathbf{x}_{\mathrm{b1}} = \left[x\left[0,0\right], \ldots, x\left[0,Q-1\right]\right]^\mathrm{T}, \tag{5.3}$$

$$\mathbf{x}_{\mathrm{b2}} = \left[x\left[1,1\right], \ldots, x\left[1,Q-1\right]\right]^\mathrm{T}, \tag{5.4}$$

and the concatenated vector of the received signal at block pilot positions as

$$\begin{aligned}\mathbf{y}_\mathrm{b} =& [y\left[0,0\right], \ldots, y\left[0,Q-1\right], \\ & y\left[1,0\right], \ldots, y\left[1,Q-1\right]]^\mathrm{T}.\end{aligned} \tag{5.5}$$

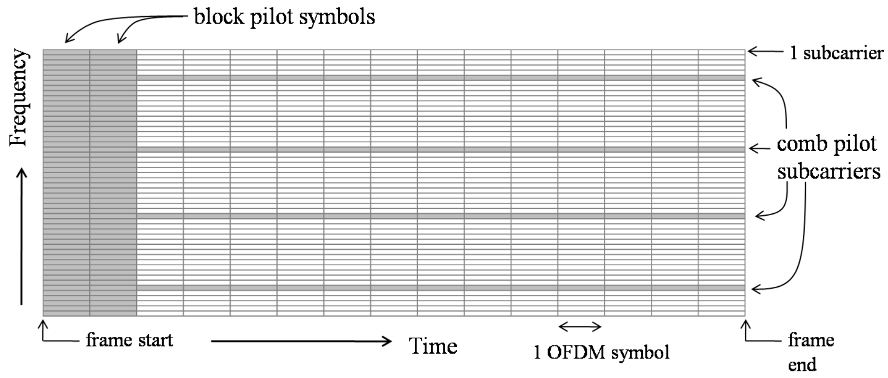

Figure 5.5: Frame structure of IEEE 802.11p.

The channel estimates are obtained as

$$\hat{\mathbf{h}} = (\mathbf{X}_{\mathrm{b}}^{\mathrm{H}}\mathbf{X}_{\mathrm{b}})^{-1}\mathbf{X}_{\mathrm{b}}^{\mathrm{H}}\mathbf{y}_{\mathrm{b}}, \tag{5.6}$$

where $\mathbf{X}_{\mathrm{b}} = [\mathrm{diag}(\mathbf{x}_{\mathrm{b1}}), \mathrm{diag}(\mathbf{x}_{\mathrm{b2}})]^{\mathrm{T}}$. The estimated channel coefficients are then used for the whole frame assuming a block fading channel.

- Block-comb-type MMSE (BC-MMSE) channel estimator [104]: An initial estimate of the channel is calculated from the comb pilots using the least square estimation. Subsequently, a linear MMSE filtering is performed in the time domain. The channel coefficients at comb pilot positions are defined as

$$\mathbf{h}_{\mathrm{c}i} = \left[x\left[0, \mathcal{I}_{\mathrm{c}}(i)\right], \ldots, x\left[M-1, \mathcal{I}_{\mathrm{c}}(i)\right]\right]^{\mathrm{T}}. \tag{5.7}$$

The MMSE estimate of the channel matrix is obtained as

$$\hat{\mathbf{H}} = \hat{\mathbf{R}}\mathbf{X}_{\mathrm{b}}^{\mathrm{H}}(\mathbf{X}_{\mathrm{b}}\hat{\mathbf{R}}\mathbf{X}_{\mathrm{b}}^{\mathrm{H}} + \sigma^2\mathbf{I})^{-1}\mathbf{Y}, \tag{5.8}$$

where $\mathbf{Y}$ is the matrix containing the received symbols at pilot positions. The channel time correlation matrix is estimated as

$$\hat{\mathbf{R}} = \frac{1}{4}\sum_{i=1}^{4}\hat{\mathbf{h}}_{\mathrm{c}i}\hat{\mathbf{h}}_{\mathrm{c}i}^{\mathrm{H}} \tag{5.9}$$

where $\hat{\mathbf{h}}_{\mathrm{c}i}$ is the least square estimate of $\mathbf{h}_{\mathrm{c}i}$.

- Iterative channel estimator based on discrete prolate spheroidal sequences (DPSs) in the time and frequency domain [71] [67] (referred to as iterative DPS channel estimator in the rest of the paper): The channel estimation is performed using a reduced-rank MMSE equalizer. The output of the equalizer is used as input to a BCJR decoder [106] after de-mapping and de-interleaving. The soft-output information from the BCJR decoder is used iteratively to obtain a better channel estimate.

5.2.3 Relaying Techniques

Placing a relay node at the intersection may enhance the reliability of communications. We confine ourselves to the DF protocol. From a practical implementation point of view, we consider only half duplex relays, meaning that the relay is not able to transmit and receive simultaneously. In the relaying context, TX and RX are referred to as source and destination, respectively. We consider a system with a moving source, a static relay and a moving destination. The relay is static at the intersection in which the exchange of information can be safety critical. The moving source and destination travel at velocities v_{s} and v_{d}, respectively. In this paper, we consider a time-division duplex (TDD) relaying strategy, where the data transmission consists of two phases with equal time duration. During the *first* phase, the source broadcasts the modulated signal towards the relay and the destination. The received signals at the relay and the destination are

$$y_{\mathrm{SR}}[m,q] = h_{\mathrm{SR}}[m,q]x[m,q] + z_{\mathrm{SR}}[m,q] \tag{5.10}$$

$$y_{\mathrm{SD}}[m,q] = h_{\mathrm{SD}}[m,q]x[m,q] + z_{\mathrm{SD}}[m,q] \tag{5.11}$$

where $h_{\mathrm{SR}}[m,q]$ and $h_{\mathrm{SD}}[m,q]$ denote the channels from source to relay (SR) and source to destination (SD) at time index m and subcarrier q, respectively. Additive complex symmetric Gaussian noise at the relay and destination is denoted as $z_{\mathrm{SR}}[m,q] \sim \mathcal{CN}(0,\sigma^2)$ and $z_{\mathrm{SD}}[m,q] \sim \mathcal{CN}(0,\sigma^2)$.

Then, the detected symbols $\hat{x}[m,q]$ at the relay are re-encoded and transmitted to the destination in the *second* phase. The received signal at the destination is

$$y_{\mathrm{RD}}[m,q] = h_{\mathrm{RD}}[m,q]\hat{x}[m,q] + z_{\mathrm{RD}}[m,q], \tag{5.12}$$

where $h_{\mathrm{RD}}[m,q]$ denotes the channel from relay to destination (RD) at time index m and subcarrier q. Additive complex symmetric Gaussian noise at the destination is denoted by $z_{\mathrm{RD}}[m,q] \sim \mathcal{CN}(0,\sigma^2)$.

At the destination, the signal received from the source during the first phase, and the signal received from the relay during the second phase, are combined using maximum ratio combining (MRC) [107]. Defining $\mathbf{y} = [y_{\mathrm{RD}}, y_{\mathrm{SD}}]^{\mathrm{T}}$ and $\mathbf{z} = [z_{\mathrm{RD}}, z_{\mathrm{SD}}]^{\mathrm{T}}$, the combined signal at the destination is

$$r[m,q] = \mathbf{u}^{\mathrm{H}}[m,q]\mathbf{y}[m,q]. \tag{5.13}$$

Table 5.2: Parameters for transmission

Parameter	Value
Transmit power [dBm]	20
Antenna gain [dB]	0
System loss [dB]	5
Data rate [Mbps]	6 (QPSK)
Frame length [Bytes], M	200
Bandwidth [MHz], T_c	10
Noise power [dBm], σ^2	-104

The combining weights are calculated as

$$\mathbf{u}[m,q] = \frac{\left[\hat{h}_{\mathrm{RD}}\left[m,q\right], \hat{h}_{\mathrm{SD}}\left[m,q\right]\right]^{\mathrm{T}}}{\left\|\left[\hat{h}_{\mathrm{RD}}\left[m,q\right], \hat{h}_{\mathrm{SD}}\left[m,q\right]\right]\right\|}, \tag{5.14}$$

where $\hat{h}_{\mathrm{SD}}$ and $\hat{h}_{\mathrm{RD}}$ are the estimates of h_{SD} and h_{RD}.

5.3 Simulation Results

Using the channel model parameterized in Section. 5.1, we re-tune the center frequency and bandwidth according to the 802.11p system parameters. The simulation is performed at varying TX/RX positions and velocities. For each different combination, 100 frames are simulated. We choose the 802.11p coding and modulation scheme achieving 6 Mbps, which is one of the most robust transmission schemes. It employs quadrature phase shift keying (QPSK) modulation and a convolutional code with constraint length 7 at a coding rate of 1/2. Tab. 5.2 lists the detailed parameters of the simulation. The communication performance in terms of FER is presented in this section.

5.3.1 Performance without Relaying

In this section, we present the result of direct transmission without relaying. Fig. 5.6 shows the FER result using the different channel estimators at varying TX and RX positions with different velocities. For the investigated scenario, the LOS is only available at the lower left corner when both vehicles are 10 m away from the intersection. As expected, the FER is strongly distance dependent. For BLS, when both cars are far away from the intersection (> 50 m), almost no frame can be successfully delivered due to the low SNR (power-limited scenario). It is noteworthy

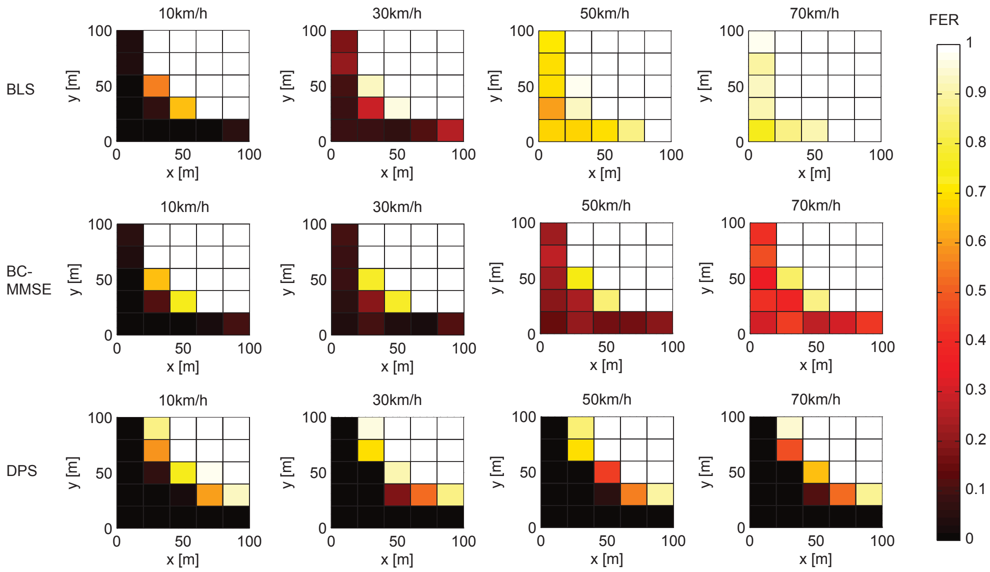

Figure 5.6: FER results without relaying using BLS, BC-MMSE and DPS estimators, at different TX and RX positions ($\{10, 30, 50, 70, 90\}$m to the center).

that if one vehicle is close to the intersection, e.g., < 10 m, a high enough SNR can be guaranteed regardless of the position of the other vehicle. Thus, the FER is almost independent of the position of the other vehicle. In this region, the FER increases with the velocities of the vehicles (velocity-limited scenario). This is due to the fact that the channel estimates are acquired only from the block pilots and used for the whole frame. However, the channel changes after the transmission of pilots which leads to an increased FER due to the use of outdated channel estimates.

The increase of FER due to high mobility is relieved using BC-MMSE channel estimator. The estimated time-correlation matrix provides a good estimate of the time evolution for channels with low delay spread. This improves the performance of a block pilot based channel estimator.

To further combat the degradation caused by high mobility, a more advanced signal processing algorithm at the RX has to be used. In Fig. 5.6, we show the FER results using the iterative DPS channel estimator with 5 iterations. It can be seen that the DPS channel estimator is robust to higher velocities. Compared to the BLS estimator, the FER is improved, which gives an extended possible communication region. As indicated in [108], a brake warning should be given at approximately 3 s to a potential collision. If the vehicles travel at 70 km/h, the communication between vehicles has to be established at a distance of around 60 m, which is still very challenging for the current setup.

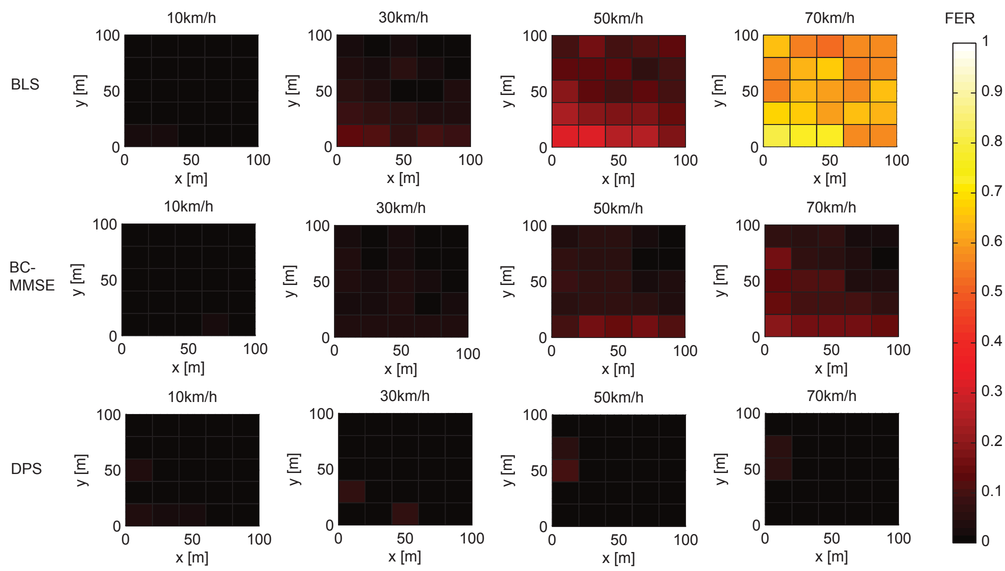

Figure 5.7: FER results with relaying using BLS, BC-MMSE and DPS estimators, at different TX and RX positions ($\{10, 30, 50, 70, 90\}$m to the center).

5.3.2 Performance with a Relay at the Intersection Center

In order to further enhance the communication performance, we place a fixed DF relay at the center of the intersection (at the origin in Fig. 5.1) and assume LOS between the relay and the two vehicles. The transmission parameters of the relay are given in Tab. 5.2. MRC is used at the RX to combine the signals received from the TX and relay. Fig. 5.7 shows the FER with relaying using different channel estimators. It can be seen that the entire region becomes almost distance-independent because the relay guarantees a high SNR for the SR link and the RD link. In this region, almost all frames are successfully received at a speed of 10km/h, while for the vehicle velocity of 70 km/h the error rate increases to around 70% using the BLS estimator. Therefore, in the high SNR regime with high mobility of the TX and the RX, the use of the BLS estimator limits the performance. The BC-MMSE estimator provides better performance by accounting for the time variability of the channel. The improvement is considerable compared to BLS estimation, especially if all sub-channels fade similarly (e.g., a channel with strong LOS component and low delay spread). We can observe slightly higher FER when a vehicle is near the intersection. This is because more multipath components are enabled near the intersection, which degrades the performance due to the increase of delay- and Doppler-spreads. If the iterative DPS estimator is used together with a relay in the intersection center, almost error-free transmission can be achieved even at 70km/h.

6 Vehicular Channel Modeling using a Cluster Based Approach

A geometry-based stochastic channel model (GSCM) is investigated in Chapter 5, where the scatterers causing the multipath components (MPCs) are randomly placed according to a spatial distribution. However, the complexity of a GSCM is high due to the summation of a large number of complex exponentials.

In this chapter, we propose a cluster based vehicular channel model resulting in a much lower computational complexity. The reduction of complexity comes in two-fold: 1) We model only the relevant MPCs above a certain power level. The MPCs with weak power contribution will be masked by the noise, thus they can neither be exploited by the receiver (RX) nor have an impact on the RX performance. 2) Moreover, we further reduce the complexity by clustering the MPCs exhibiting similar properties.

In Section 6.1, we first present a joint cluster identification-and-tracking approach based on the power spectral density in delay and Doppler. The algorithm is applied to vehicular channel measurement data, which is described in Section 6.2. We characterize the cluster lifetime, delay and Doppler spreads based on vehicular channel measurements data and present the corresponding results for line of sight (LOS) obstruction scenario in Section 6.3. Finally, in Section 6.4, we develop a cluster-based vehicular channel model with low computational complexity suitable for a real-time implementation.

6.1 Cluster Identification-and-Tracking Approach

As indicated in [104], the delay and Doppler spreads have a strong impact on the RX performance, which makes channel modeling in these two domains more important. Therefore, we perform the clustering algorithm using a delay-Doppler power spectrum estimate in form of the local scattering function (LSF) [70]. MPCs having similar delay and Doppler shift will form a cluster. In order to develop an accurate cluster based channel model, the knowledge of cluster parameters, including lifetime, delay and Doppler spreads, is of great importance. The vehicular environment changes rapidly due to high velocities of the transmitter (TX) and RX. This also results in fast changing cluster parameters.

In order to consistently characterize the evolution of cluster parameters over time, we introduce our cluster identification and tracking algorithm in this section. We firstly calculate the LSF from measurement data in Section 6.1.1. In Section 6.1.2, we distinguish relevant MPCs based on the defined thresholds. The density-based spatial clustering of applications with noise (DBSCAN) clustering algorithm is introduced for identification in Section 6.1.3. In Section 6.1.4, we introduce the cluster tracking algorithm based on the distance between the clusters' centroids.

6.1.1 LSF Estimator

The vehicular propagation conditions measured by the time-variant frequency response $g(t, f)$ change rapidly due to the high velocities of the TX and RX. Thus, the observed sampled fading process $g[m, q] = g(mt_s, qB/N)$ is non-stationary, where t_s is the sampling interval in time, B is the channel bandwidth, Q denotes the number of samples in the frequency domain, m is the discrete time index and q is the frequency index, respectively.

Due to the finite rate of the environment changes, the non-stationarity can be overcome by approximating the fading process to be locally wide-sense stationary for a region with finite extent in time and frequency [109]. The local stationarity region is defined as having $M \times N$ samples in time and frequency, respectively. For each stationarity region we are now able to calculate the LSF [70, 110], see Fig. 6.1 (a) and (c).

The total number of snapshots and frequency bins within one measurement run are denoted by S and Q, respectively. Therefore, the time index of each stationarity region is $k_t \in \{0, \cdots, \lfloor S/M - 1 \rfloor\}$, and the frequency index of each stationarity region is $k_f \in \{0, \cdots, \lfloor Q/N - 1 \rfloor\}$. k_t and k_f correspond to the center of each stationarity region. The relative time index within each stationarity region is $m' \in \{-M/2, \ldots, M/2 - 1\}$. The relationship between the relative and absolute time index is given by $m = k_t M + m'$. Similarly, the relative frequency index within each stationarity region is $q' \in \{-N/2, \ldots, N/2 - 1\}$. Its relationship to the absolute frequency index is given by $q = k_f N + q'$.

An estimate of the discrete LSF is defined as $\hat{C}[k_t, k_f; n, p]$ [70], where $n \in \{0, \cdots, N - 1\}$ is the delay index, and $p \in \{-M/2, \cdots, M/2 - 1\}$ is the Doppler index. In our work, we are interested in $\hat{C}[k_t; n, p]$, where $k_f = 0$ because of $Q = N$. The LSF $\hat{C}[k_t; n, p]$ is a time-varying representation of the delay-Doppler spectral density. In order to consistently characterize the evolution of cluster parameters over

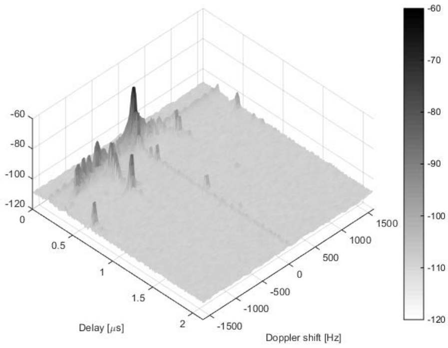

(a) Local scattering function at $k_{t,0}$

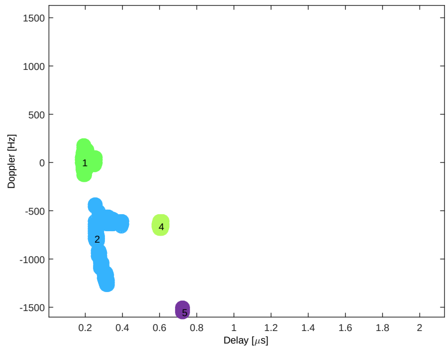

(b) Cluster identification $k_{t,0}$

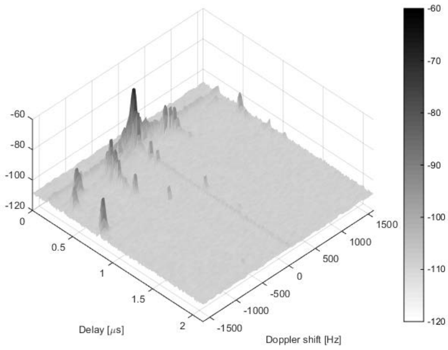

(c) Local scattering function at $k_{t,1}$

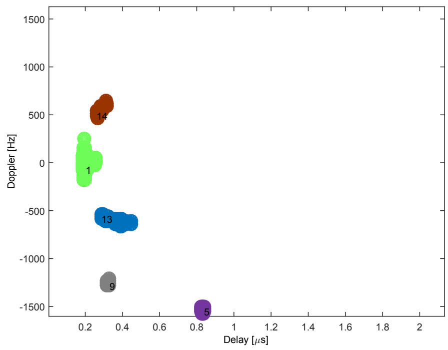

(d) Cluster identification $k_{t,1}$

Figure 6.1: Local scattering function and identified clusters at two different time instants $k_{t,0}$ and $k_{t,1}$

time, a cluster identification and tracking algorithm is needed.

6.1.2 Data Preprocessing

We are only interested in relevant MPCs above a certain power level. In the first step, we identify these MPCs in the LSF, employing the power threshold criterion [28], where two power thresholds are used. A MPC exists if both of the following two criteria are satisfied: (1) the power of the MPC is γ dB above the noise floor, and (2) the power of the MPC is not more than κ dB below the highest detected peak. In this work, we choose $\gamma = 10$ and $\kappa = 25$. The MPCs which do not satisfy the above criteria are set to zero.

6.1.3 Cluster Identification

In order to identify the clusters formed by the relevant MPCs, the DBSCAN algorithm [111] is used, which is a density-based clustering algorithm to discover clusters of arbitrary shape. The key idea of the DBSCAN algorithm is that for each point of a cluster, the neighborhood of a given radius *Eps* for each point ℓ in one cluster has to contain at least a minimum number of points *minPts* [111]. DBSCAN does not require one to specify the number of clusters in the data a priori, as opposed to the KPowerMeans [112]. DBSCAN requires only two input parameters, i.e. neighborhood radius *eps* and the minimum number of objects in a neighborhood *minPts*. The user can determine an appropriate value for it. The DBSCAN algorithm finds clusters with the following steps.

- It starts with an arbitrary starting point and finds all the neighbor points within distance *eps* of the starting point. A cluster will be formed if the number of neighbors is greater than or equal to *minPts*. The starting point and its neighbors are included in this cluster and the starting point is marked as visited.

- The algorithm then repeats the evaluation process for all the neighbors recursively. If the number of neighbors is less than *minPts*, the point is marked as noise.

- If a cluster is fully expanded (all reachable points are visited) then the algorithm proceeds with the remaining unvisited points in the dataset.

In this work, we use *minPts*=2 and *eps*=8.

6.1.4 Cluster Tracking Approach

The purpose of tracking is to capture the evolution of the cluster centroid movement and the time-variant cluster parameters. The algorithm is based on the multipath component distance (MCD) [25] measure of the cluster centroids. At time index k_t, $I[k_t]$ cluster centroids $\boldsymbol{\mu}_i[k_t] = [\mu_i^\tau[k_t], \mu_i^\nu[k_t]]^\mathrm{T}$ are detected, where $i \in \{0, \ldots, I[k_t]-1\}$. Let us consider $L[k_t]$ MPCs at time k_t. Every single MPC l is associated with power $P_l[k_t]$ and parameter vector $\mathbf{x}_l[k_t] = [\tau_l[k_t], \nu_l[k_t]]^\mathrm{T}$ containing the delay and Doppler, where $l \in [0, \ldots, L-1]$. Denoting the set of MPCs indices belonging to cluster i at time instant k_t by $L_i[k_t]$, the centroid of cluster i for stationarity region

k_t is calculated as

$$\boldsymbol{\mu}_i[k_t] = [\mu_i^\tau[k_t], \mu_i^\nu[k_t]]^{\mathrm{T}} \tag{6.1}$$
$$= \frac{1}{\sum_{l \in L_i[k_t]} P_l[k_t]} \begin{bmatrix} \sum_{l \in L_i[k_t]} P_l[k_t]\tau_l[k_t] \\ \sum_{l \in L_i[k_t]} P_l[k_t]\nu_l[k_t] \end{bmatrix}. \tag{6.2}$$

The current stationarity region is denoted by k_t and the previous one by $k_t - 1$. The subsequent sets of new $I[k_t]$ and old $I[k_t-1]$ cluster centroids $\boldsymbol{\mu}_{i_\text{new}}[k_t]$ and $\boldsymbol{\mu}_{i_\text{old}}[k_t-1]$, are considered, where $i_\text{new} \in \{0, \cdots, I[k_t] - 1\}$ and $i_\text{old} \in \{0, \cdots, I[k_t - 1] - 1\}$ are the cluster centroids' indices at k_t and $k_t - 1$, respectively. The MCD between the centroids $\boldsymbol{\mu}_{i_\text{new}}[k_t]$ and $\boldsymbol{\mu}_{i_\text{old}}[k_t - 1]$ is defined as [25]

$$\begin{aligned} d_{i_\text{new} i_\text{old}} &= \mathrm{MCD}(\boldsymbol{\mu}_{i_\text{new}}[k_t], \boldsymbol{\mu}_{i_\text{old}}[k_t - 1]) \\ &= \sqrt{|\mu^\tau_{i_\text{new}}[k_t] - \mu^\tau_{i_\text{old}}[k_t - 1]|^2 + |\mu^\nu_{i_\text{new}}[k_t] - \mu^\nu_{i_\text{old}}[k_t - 1]|^2} \end{aligned} \tag{6.3}$$

It can be seen that the MCD combines parameters that come in different units. The tracking algorithm proceeds as follows:

1. The MCD between any old (at time $k_t - 1$) and any new centroids (at time k_t) is calculated.

2. If the distance between a new centroid and its closest old centroid is larger than a predefined threshold, the new centroid is regarded as a newly detected centroid.

3. For each old centroid, the number of new centroids within the threshold c is checked:
   - If $c = 1$, the old centroid is moved.
   - If $c > 1$, the old centroid splits. The closest new one is regarded as old moved centroid. All others are treated as new centroids.

Fig. 6.1 shows the local scattering function and the identified clusters of an exemplary vehicular channel measurement in the delay-Doppler domain at two different time instants. Each cluster is color-coded according to the cluster ID given by the tracking algorithm. At time instant $k_{t,0}$, four clusters are detected. Cluster 1 corresponds to the LOS component, which exists in both time instants. Cluster 5 stemming from the vehicle in the opposite direction, appears also in both time instants. However the position of cluster 5 is changed due to the movements of the vehicles. Cluster 2 disappears and splits into several clusters at $k_{t,1}$.

6.2 Measurement Data

The measurements used in the present work were collected in the DRIVEWAY'09 measurement campaign [103] conducted in Lund, Sweden. The channel impulse response is measured with a time resolution of $t_s = 307.2\,\mu$s. The total time interval is around $T = 10\,$s. Therefore, there are $S = 32000$ snapshots in total. The carrier frequency is $f_c = 5.6\,$GHz with a bandwidth of $B = 240\,$MHz and $Q = 769$ frequency bins. Both TX and RX car are equipped with a linear array with four circular polarized patch antennas perpendicular to the driving direction. The antennas cover the four main propagation directions due to their main lobes [113]. In order to achieve a 360° coverage in the azimuth plane, we consider to combine the antenna radiation pattern.

We select two scenarios to analyze: (i) A truck obstructing LOS scenario, where the TX and RX drive in the same direction on a highway at around 75 km/h. The TX drives in front. There is one truck in between TX and RX on the same lane and a car drives by on the left lane. In addition, there is a truck in the front of the TX. A 2-D top view of this scenario is shown in Fig. 6.2(a). (ii) A LOS scenario shown in Fig. 6.2(b), where the TX and RX also drive in the same direction on a highway at around 90 km/h. One truck is driving on the left lane, while the other truck is in front of TX. For both scenarios, there are some traffic signs along the highway. Meanwhile, some vehicles drive in the opposite direction on the other lane of the highway.

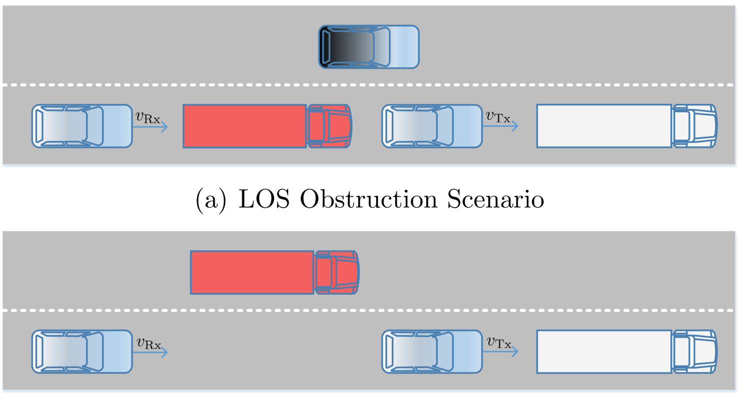

(a) LOS Obstruction Scenario

(b) LOS Scenario

Figure 6.2: 2-D top view of the measurements scenarios.

6.3 Simulation Results

We characterize the cluster lifetime, delay and Doppler spreads, which are defined as follows:

Cluster Lifetime

We can observe that the unique cluster ID C_{ID} is assigned to a new cluster, while the moved cluster inherits the same C_{ID} from its predecessor. Based on this, we are able to analyze the cluster lifetime, which indicates how many stationarity regions the cluster exists.

Cluster Spread

Denoting the set of MPCs indices belonging to cluster i at time k_t by $L_i[k_t]$, the joint cluster spread is given by

$$\mathbf{C}_i[k_t] = \frac{\sum_{l \in L_i[k_t]} P_l[k_t]\big(\mathbf{x}_l[k_t] - \boldsymbol{\mu}_i[k_t]\big)\big(\mathbf{x}_l[k_t] - \boldsymbol{\mu}_i[k_t]\big)^{\mathrm{T}}}{\sum_{l \in L_i[k_t]} P_l[k_t]}. \tag{6.4}$$

The 2×2 covariance matrix $\mathbf{C}_i[k_t]$ is symmetric where its main diagonal entries represent the root mean square (RMS) cluster spread in the delay and Doppler domain and off-diagonal entries represent the respective correlation between these spreads. The noise associated with MPCs are greatly filtered out by averaging over each individual covariance matrix.

For cluster i, we extract the RMS values of delay spread $S_i^{\tau}[k_t]$ and Doppler spread $S_i^{\nu}[k_t]$ from the $\mathbf{C}_i[k_t]$, where

$$S_i^{\tau}[k_t] = \sqrt{\mathbf{C}_{i[1,1]}[k_t]} \text{ and } S_i^{\nu}[k_t] = \sqrt{\mathbf{C}_{i[2,2]}[k_t]}. \tag{6.5}$$

In this section, The result and fitting of the empirical distributions will be demonstrated for the LOS obstruction scenario. Then, we perform the same analysis for the more measurement data and provide the results in Appendix 6.5.

6.3.1 Analysis of Cluster Lifetime

We calculate the LSF from measurement data firstly, where $S = 32000$ snapshots are divided in stationarity regions of $M = 128$ samples each. The stationarity regions are indexed by $k_t \in \{0, \ldots, 249\}$ for our case. The relevant MPCs are detected and the identification-and-tracking approach is applied.

In order to analyze the time-variant cluster spreads, we plot in Fig. 6.3 the movement of cluster centroids during the entire 10 s measurement run. We append the

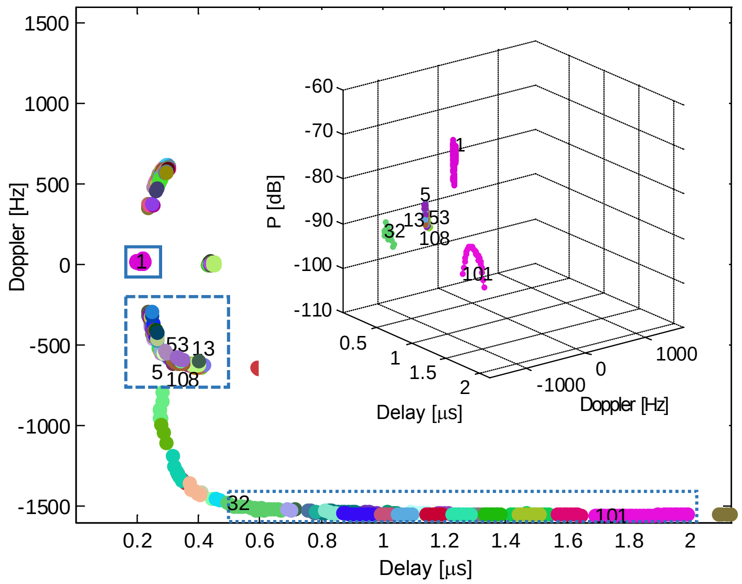

Figure 6.3: Movement of cluster centroids in a 10s measurement run. The centroids with the same color are from the same cluster.

IDs to the clusters which exist for more than 15 stationarity regions (0.59 s). A close-up 3-D view of these clusters is also included in Fig. 6.3. According to the geometrical information of measurements, we divide the clusters into three categories: (i) The detected cluster $C_{\mathrm{ID}} = 1$, related to the obstructed LOS component, remains throughout the entire measurement run and contributes the highest gain. Its Doppler shift is around 0 Hz. (ii) For the clusters $C_{\mathrm{ID}} \in \{5, 13, 53, 108\}$, the delay and Doppler shift values change slowly during their lifetimes. In addition, due to the negative Doppler shifts, we consider that these clusters come from the contribution of traffic signs and other static objects. (iii) For the clusters $C_{\mathrm{ID}} \in \{32, 101\}$, it can be seen that their Doppler shifts are almost constant, while their delay values are changing considerably during their cluster lifetimes. These clusters are from the contribution of big trucks in the opposite lane behind the TX and RX vehicles.

For the LOS obstruction scenario, there are 132 clusters detected over the total time duration. Fig. 6.4(a) shows the number of detected clusters per stationarity region. More clusters are detected during the second half of the measurement. The tracked cluster lifetimes are shown in Fig. 6.4(b), where the length of the horizontal lines indicate the lifetime of the relevant cluster. It can be observed that many clusters exist only for one stationarity region, which can not be tracked. We mark the clusters who exist more than 15 stationarity regions, equivalent to 0.59 s, in Fig. 6.4(b). In total, there are 7 marked clusters. Without considering the longest

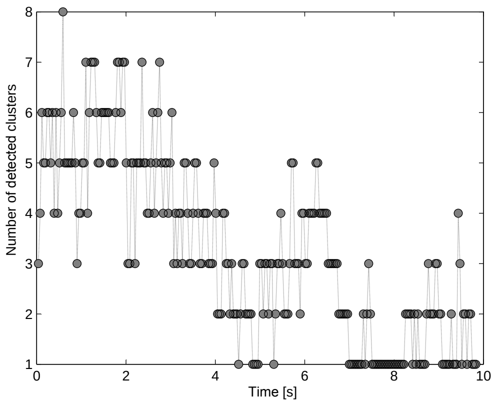

(a) Number of clusters

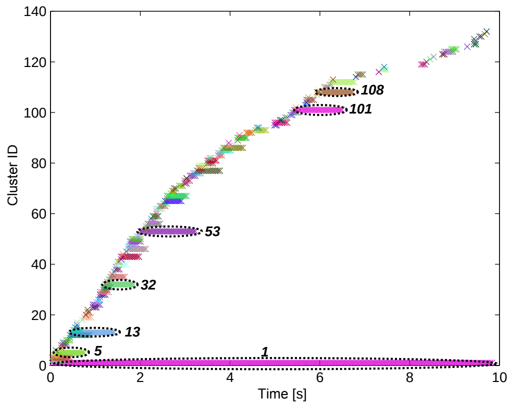

(b) Cluster lifetimes

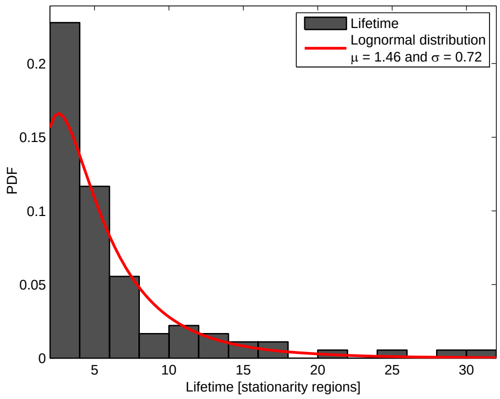

(c) Distribution

Figure 6.4: Number of clusters per stationarity region, cluster lifetimes and its log-normal distribution for the LOS obstruction scenario.

and shortest lifetimes, the distribution of the probability density of cluster lifetimes obeys a lognormal distribution with a mean $\mu = 1.46$ and a standard deviation $\sigma = 0.72$, shown in Fig. 6.4(c).

The characterization results of the cluster lifetime for highway scenario with LOS is provided in Appendix 6.5.1.

6.3.2 Analysis of Cluster Joint Spread

We have 12 measurement runs performed in the highway scenario with obstructed LOS. In this section we will demonstrate the results and fitting of the empirical distributions for one measurement. Then, we perform the same analysis for the whole data set and provide the fitting parameters in Appendix 6.5.2.

In Fig. 6.5, we plot the delay and Doppler spreads of clusters $C_{\text{ID}} \in \{1, 101\}$ in

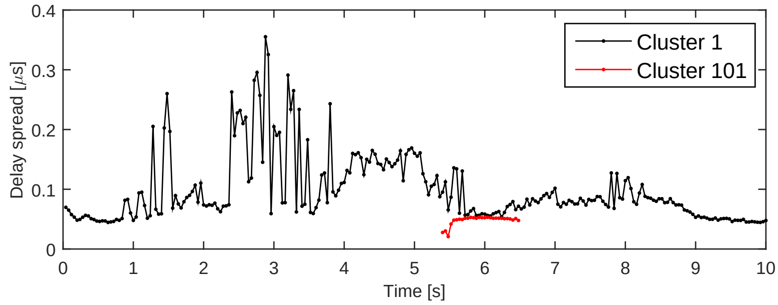

(a) Delay spread

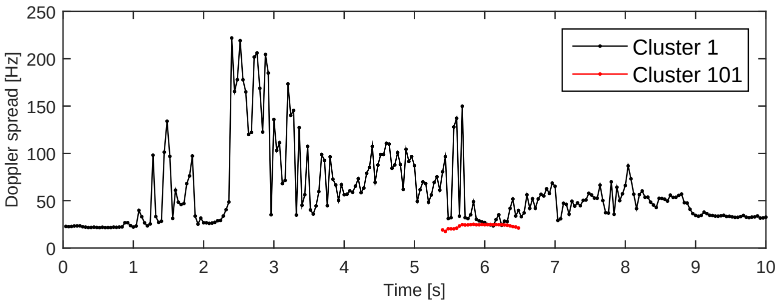

(b) Doppler spread

Figure 6.5: Delay and Doppler spread of cluster 1 and culster 101 in their corresponding lifetime

their corresponding lifetime. Cluster 1 exists throughout the entire measurement run, while Cluster 101, stemming from the vehicle in the opposite direction, appears only from 5.5 s to 6.5 s. We can observe that the spread of cluster 1 changes rapidly in the time interval from 1 s to 6 s. This is due to the richness of MPCs that appear around the origin. From 1 s to 6 s, two big trucks traveling in the opposite direction are right in between the TX and RX. The MPCs due to the contribution of these scatterers locate very close to the position of the LOS component. The clustering algorithm will not separate them, thus resulting in a large delay and Doppler spreads of the merged cluster. On the other hand, the spreads of cluster 101 are relatively low due to the small size of the cluster and remain almost unchanged over the lifetime.

The cluster corresponding to LOS exhibits different characteristics from the other clusters. Hence, we will analyze the distribution of cluster 1 (the cluster corresponding to the LOS component) and the rest of clusters separately to obtain a better fit. We employ lognormal distribution for the fitting, which gives a reasonable fit. For the delay spread of cluster 1, a mean of 2.52 and standard deviation of 0.43 gives a good fit. For the Doppler spread, a lognormal with a mean of 3.82 and a standard deviation of 0.52 fits the empirical result. The distributions of delay and Doppler

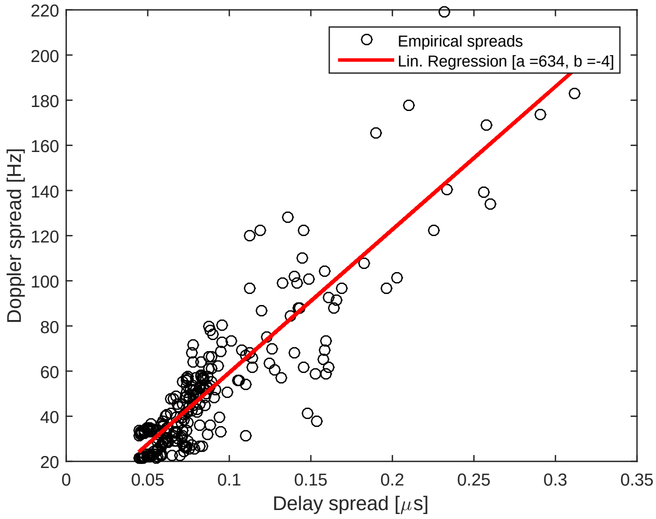

Figure 6.6: Scatter plot of the delay spread versus Doppler spread for cluster 1 (corresponding to the LOS component) with a least-squares linear regression line.

spreads of the other clusters (except for cluster 1) follows lognormal distributions with mean values 3.34 and 3.05, and standard deviation 1.9 and 1.74, respectively. In general, these clusters have smaller spreads compared to cluster 1.

In order to find the relationship between delay spread and Doppler spread, Fig. 6.6 and 6.7 show the scatter plots of the delay spread versus Doppler spread for LOS cluster and the other clusters, respectively. We can observe that delay and Doppler spreads are correlated for the cluster associated with LOS. This indicates that the extension of the LOS cluster occurs in both domains simultaneously for the investigated measurement. Moreover, a least-squares linear regression line is superimposed on the scatter plot, which satisfies $S^{\nu} = aS^{\tau} + b$ with $a = 634$ and $b = -4$. For the rest of the clusters, the delay and Doppler spreads concentrate more on small values, which can be seen in Fig. 6.7. Moreover, we observe a similar correlation as in Fig. 6.6.

6.4 Simplified cluster-based vehicular channel model

Vehicular communication channels are characterized by a time- and frequency-selective non-stationary fading process. We have analyzed the clustering of MPCs in the delay-Doppler domain using the LSF of channel measurement data. A general characterization of cluster parameters has been presented in Section 6.3. In

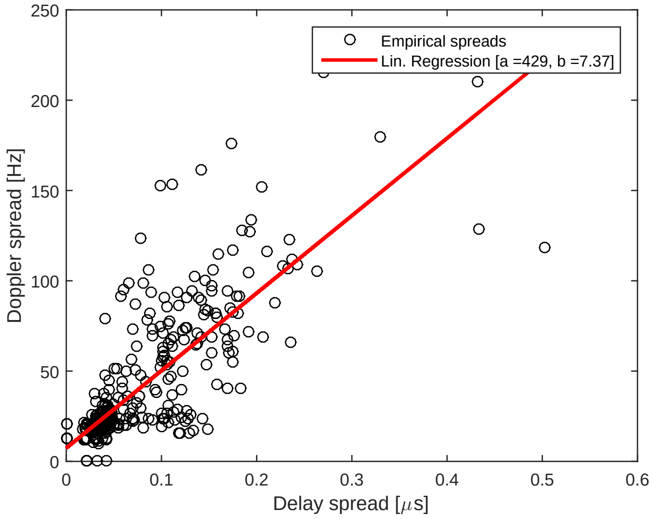

Figure 6.7: Scatter plot of the delay spread versus Doppler spread for other clusters with a least-square linear regression line.

this section, we will devise a simplified cluster-based vehicular channel model by dividing the cluster locations in the delay-Doppler plane into different characteristic regions. The time-variant cluster parameters, including cluster birth rate, relationship between delay and Doppler shift, and the distribution of the lifetime and of the cluster gain in each region, are characterized. For low complexity emulation, the cluster parameters are randomly drawn from this pre-computed distributions. Our model is validated with measurement data using the cumulative distribution function (CDF) of the RMS delay spread and Doppler spread. A close match of our numeric model with measurement results is demonstrated. In this section, we use the LOS obstruction scenario as shown in Fig. 6.2(a).

6.4.1 Non-Stationary Cluster Model

We represent the sampled time-variant frequency response as superposition of clusters for the stationarity region k_t

$$g[m,q] = g[k_t M + m', q] = g_{\mathrm{TX}}[q] g_{\mathrm{Rx}}[q] \cdot \sum_{i=0}^{I[k_t]-1} \alpha_i[k_t] \mathrm{e}^{-\mathrm{j}2\pi\theta_i[k_t]q} \mathrm{e}^{\mathrm{j}2\pi\eta_i[k_t]m'} , \qquad (6.6)$$

where i is the cluster index, $I[k_t]$ denotes the number of clusters, $\theta_i[k_t] = \mu_i^\tau[k_t]B/N$ is the normalized delay of the centroid of the i-th cluster for the stationarity region

Table 6.1: Conditional probability

	Newly Born Clusters			
J	0	1	2	3
1	0.750	0.212	0.019	0.019
2	0.667	0.289	0.044	0
3	0.696	0.130	0.174	0
4	0.500	0.389	0.111	0
5	0.425	0.375	0.125	0.075
6	0.421	0.474	0.105	0
7	0.500	0.500	0	0
8	1	0	0	0

k_t, $\alpha_i[k_t]$ is the average amplitude, and $\eta_i[k_t] = \mu_i^\nu[k_t]t_s$ is the normalized Doppler shift.

For comparison purposes, we employ a bandwidth $B = 240\,\text{MHz}$ and $Q = 769$ frequency bins in accordance to the bandwidth and number of frequency samples of the measurement.

6.4.2 Cluster Parameters

For the cluster model (6.6) we need to obtain the cluster parameters $I[k_t]$, α, μ^τ, and μ^ν for each stationarity region k_t from the associated LSF. We do not model the number of clusters $I[k_t]$ directly. The birth-death process of a cluster is represented by the birth rate $J[k_t]$ and the lifetime of the cluster.

6.4.2.1 Birth Rate Evaluation

Firstly, the birth rate $J[k_t]$ represents the number of newly born clusters for time k_t. In order to model the trend of the number of clusters more accurately, we evaluate the birth rate $J[k_t]$ of the the newly born clusters at k_t based on the number of clusters $I[k_t - 1]$. With $I[k_t - 1]$, we can obtain the conditional probabilities of having different number of new clusters at stationary region k_t. In Tab.6.1, the conditional probabilities are shown. The obtained conditional probabilities will be used to generate the number of clusters at each stationary time region in the proposed model.

6.4.2.2 Relationship Between Delay and Doppler Shift

Considering two vehicles moving on a highway with constant speeds, two vehicles can be placed on the x-axis as shown in Fig. 6.8, where the origin of the coordinate system is placed halfway between vehicles.

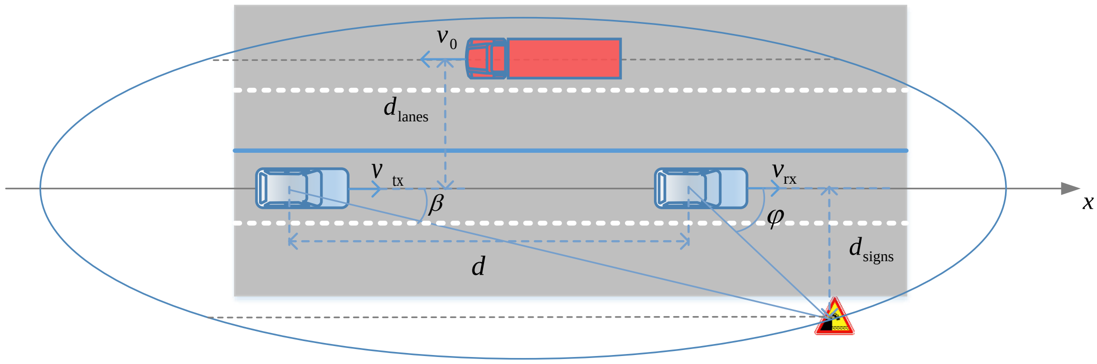

Figure 6.8: Setup of the environment. TX and RX are moving on a highway. An ellipse with the two vehicles as its foci represents locations of scatterers causing the same delay.

Due to the movement of the both vehicles, their positions are changing with time. The position $\boldsymbol{z}(t) = [x(t), y(t)]^{\mathrm{T}}$ of both vehicles can be expressed as

$$\boldsymbol{z}_{\mathrm{Tx}}(t) = \boldsymbol{z}_{\mathrm{t0}} + \boldsymbol{v}_{\mathrm{Tx}} t \tag{6.7}$$

$$\boldsymbol{z}_{\mathrm{Rx}}(t) = \boldsymbol{z}_{\mathrm{r0}} + \boldsymbol{v}_{\mathrm{Rx}} t \tag{6.8}$$

where $\boldsymbol{z}_{\mathrm{t0}} = [-d/2, 0]^{\mathrm{T}}$ and $\boldsymbol{z}_{\mathrm{r0}} = [d/2, 0]^{\mathrm{T}}$ are the initial positions of the TX and RX vehicles, $\boldsymbol{v}_{\mathrm{TX}}$ and $\boldsymbol{v}_{\mathrm{RX}}$ are the corresponding velocity vectors. The distance $d_{\mathrm{SC}}(\boldsymbol{z}, t)$ is the distance where the transmitted signal travels between the moving TX and RX over a scatterer located at $\boldsymbol{z}$. Depending on the geometrical description, $d_{\mathrm{SC}}(\boldsymbol{z}, t)$ can be expressed as

$$d_{\mathrm{SC}}(\boldsymbol{z}, t) = d_{\mathrm{t}}(\boldsymbol{z}, t) + d_{\mathrm{r}}(\boldsymbol{z}, t) \tag{6.9}$$

where $d_{\mathrm{t}}(\boldsymbol{z}, t)$ is the distance between TX and the scatterer and $d_{\mathrm{r}}(\boldsymbol{z}, t)$ is the distance between RX and the scatterer, respectively. Therefore, the transmitted signal experiences a delay

$$\tau_{\mathrm{SC}}(\boldsymbol{z}, t) = d_{\mathrm{SC}}(\boldsymbol{z}, t)/c_0\,, \tag{6.10}$$

where c_0 is the speed of light. In Fig.6.8, an ellipse with two vehicles in its foci represents locations of scatterers causing the same delay. In addition, the transmitted

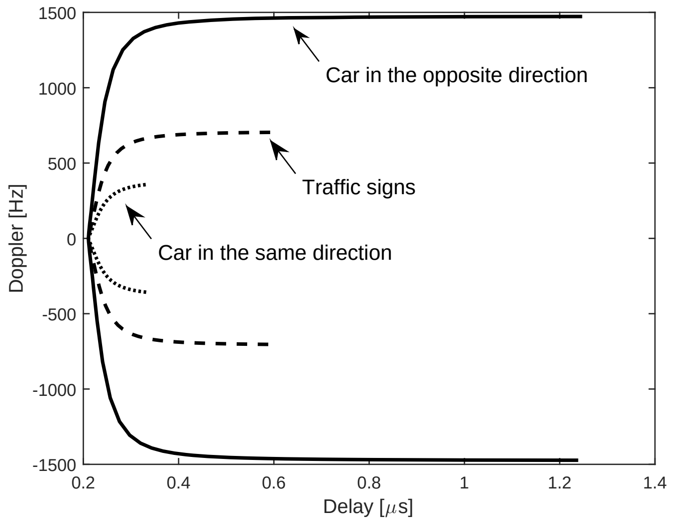

Figure 6.9: Exemplary relationship between delay and Doppler shift.

signal also experiences a Doppler shift due to the movement of vehicles, which can be obtained by

$$\nu_{\mathrm{SC}}(\beta(t), t) = (||\boldsymbol{v}_{\mathrm{Tx}}|| \cos(\beta(t)) + ||\boldsymbol{v}_{\mathrm{Rx}}|| \cos(\varphi(t)))\, f_c/c_0 \tag{6.11}$$

where β is the angle between the velocity vector $\boldsymbol{v}_{\mathrm{TX}}$ and the line connecting the TX and the scatterer, φ is the angle between the velocity vector $\boldsymbol{v}_{\mathrm{RX}}$ and the line connecting the RX and the scatterer, and f_{C} is the center frequency. Thus, the delay and Doppler shift has a certain relationship, which depends on the positions and velocities of the TX and RX, and the location of the scatterer. In Fig. 6.9, we give an example of the relationship between the delay and Doppler shift. The contributions of different scatterers lie on different 'U' shapes on the delay Doppler plane. We can use this concept to obtain the delay and Doppler shift values of the cluster in our proposed model. The premise is that the velocities of TX and RX, and the location of the cluster are known.

6.4.2.3 Region Division

Based on the relationship between delay and Doppler shift, we can divide the cluster locations into four regions as shown in Fig. 6.10. In Tab. 6.2, we obtain the probabilities of clusters located in different regions according to the number of detected clusters in each region. These probabilities can help to decide the cluster locations in the proposed channel model.

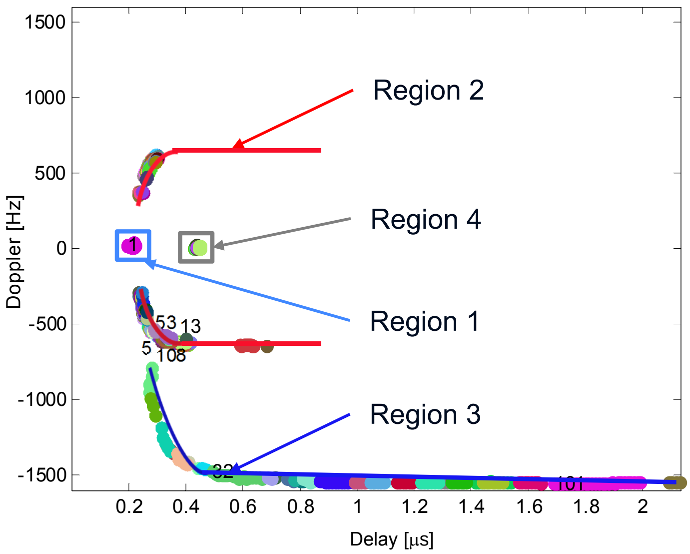

Figure 6.10: Cluster locations division.

Table 6.2: Cluster probability for the different regions

Region	1	2	3	4
Probability	-	0.69	0.24	0.07

We place a LOS cluster in the proposed model due to the fact that the cluster related to the LOS component in 'Region 1' exists throughout the whole measurement run. Therefore, in Tab. 6.2, we do not calculate the probability of the cluster located in 'Region 1'.

6.4.2.4 Distributions of Lifetime and Gain in Different Regions

After dividing the cluster locations into four regions, we analyze the distributions of cluster lifetime and gain in each region. Since the LOS cluster appears throughout the whole measurement, we only need to evaluate the distribution of the cluster gain for 'Region 1'. We found that the distribution of cluster lifetime obeys a log-normal distribution, and the distribution of cluster gain obeys a generalized extreme value distribution for the other three regions. The detailed parameters are given in Tab. 6.3.

Table 6.3: Distribution parameters for cluster lifetime and gain

	lifetime (log normal)		gain (gen. extreme value)		
Region	μ	σ	k	σ	μ
1	-	-	-0.35	2.60e-5	10.2e-5
2	0.81	0.85	0.56	2.24e-6	2.88e-5
3	1.55	0.82	0.25	6.23e-6	3.40e-5
4	1.14	1.07	0.1	8.06e-7	2.75e-5

6.4.3 Implementation of the Non-Stationary Cluster Model

To be able to incorporate our model in a practical environment, we make the following assumptions. We consider two vehicles on a highway moving parallel to each other with constant velocities v_{TX} and v_{RX}. The vehicles on the opposite direction travel at the same speed of v_0. To simplify the problem, we assume a distance of $d_{\mathrm{lanes}} = 10\,\mathrm{m}$ between the two lanes according to the environment, and a distance $d = 60\,\mathrm{m}$ between the TX and the RX. We assume the traffic signs are also $d_{\mathrm{signs}} = 10\,\mathrm{m}$ away next to the lane of the TX and the RX.

6.4.3.1 LOS Cluster

We observed that the LOS exists throughout the whole measurement run. Therefore, we assume a permanently existing LOS cluster in the delay-Doppler plane. The delay is given by the distance between the TX and RX vehicles. The power of the LOS cluster for each k_t is randomly drawn from the fitted power distribution.

6.4.3.2 Other Clusters

The rest of the clusters are generated according to the Fig. 6.11. For each stationary time region k_t, we draw a random number of newly born clusters $J[k_t]$ according to the conditional probabilities obtained in Tab. 6.1. For each newly born cluster, it will be associated with four key parameters, i.e., delay μ^{τ}, Doppler μ^{ν}, lifetime and amplitude α following the next steps:

1. We allocate each new cluster to a region according to probabilities in Tab. 6.2.
2. The lifetime of the cluster is drawn from the corresponding fitted distributions obtained in Tab. 6.3.
3. The gain of the cluster is drawn from the corresponding power distribution in Tab. 6.3.

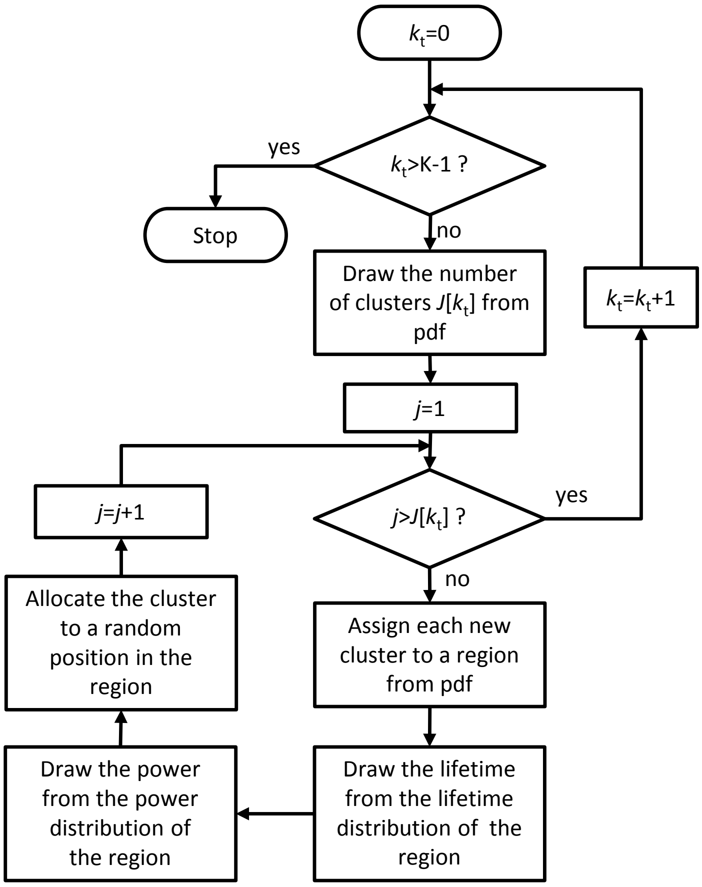

Figure 6.11: Flow Diagram of the Model.

4. We place the new cluster in a random position in the region. The relationship between delay and Doppler follows from (6.10) and (6.11).

5. If the lifetime of a new cluster is longer than one stationarity region, the geometrical position and the movement of the cluster in the delay-Doppler plane is updated using (6.7)-(6.11).

The same process is repeated for all $J[k_t]$ new clusters for every stationary region k_t. The parameters obtained for each cluster are inserted in (6.6) to generate the channel impulse response.

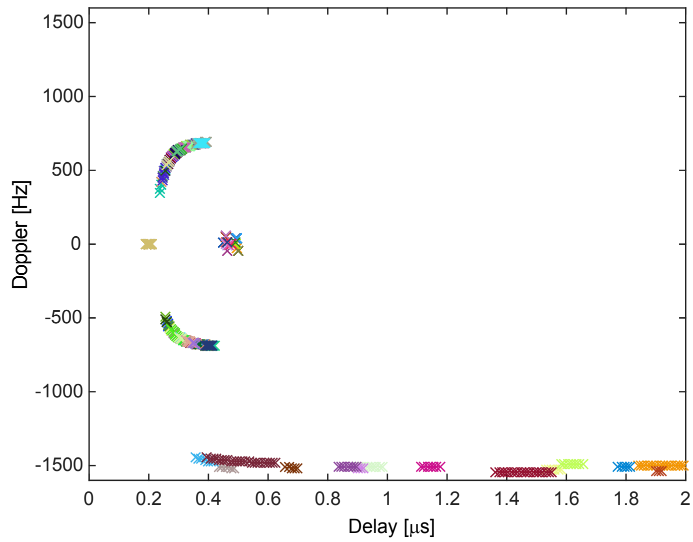

Figure 6.12: Cluster locations on a 2D plot in Delay-Doppler domain.

6.4.4 Simulation Results

In order to resemble the true environment, we assign the following velocities $v_{\mathrm{TX}} = 65\,\mathrm{km/h}$, $v_{\mathrm{RX}} = 65\,\mathrm{km/h}$, $v_0 = 70\,\mathrm{km/h}$. To evaluate the accuracy of our proposed channel model, we compare the simulation results with the measurements data based on the following statistical parameters.

We would like to confirm whether the generated cluster locations in the proposed channel model agrees with the clusters obtained by the measurements data. In Fig. 6.12, we plot the cluster locations in delay-Doppler domain in LOS obstruction and LOS scenarios. Comparing with the results obtained by the measurements data, it can be seen that the cluster locations in the simulation and measurements data can be matched with each other very well.

We compare the CDFs of the RMS delay and Doppler spread based on the proposed model and the measurements data in Fig. 6.13. The CDFs match quite well with the measurements.

6.4.5 Discussion

The proposed cluster-based vehicular channel model incorporates the ideas from both the tapped delay model and GSCM. In this section, we summarize the main properties of the proposed cluster based modeling approach in comparison with the tapped delay line model and GSCM.

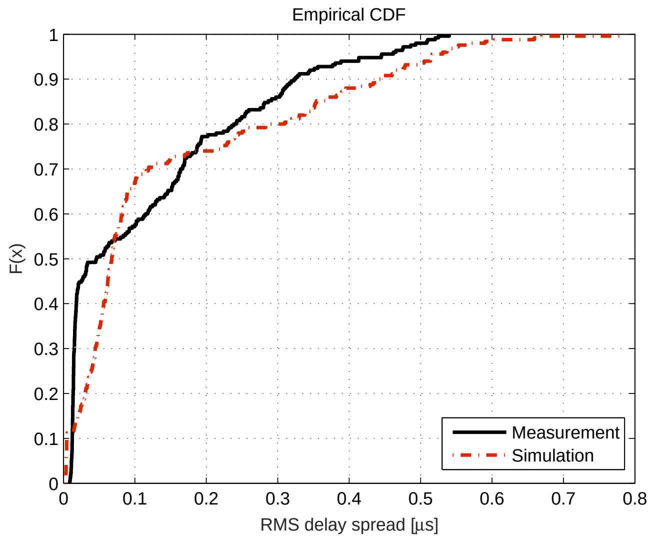

Figure 6.13: RMS delay spread CDF.

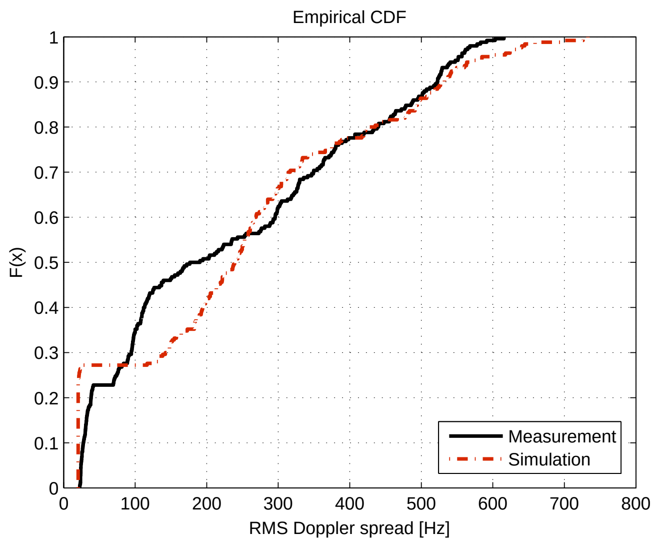

Figure 6.14: RMS Doppler spread CDF.

As discussed earlier, due to the mobility of the TX and RX in vehicle-to-vehicle (V2V) environments, the radio channel variants over time. This variation applies not only to the channel impulse response (CIR), but also to the statistics. Since statistical models, e.g. the tapped delay line model, usually have the advantage of low computational effort, they are widely used for V2V environments. Although many statical models are proposed and adopted for V2V communications, most of the models do not consider time-variant fading statistics, e.g. delay, Doppler and power. The parameters of a statistical model stay fixed over different stationarity regions, which makes it insufficient to model the dynamic change of the environment. The proposed cluster based model introduces non-stationarity by having dynamically changing channel parameters, such as delay and Doppler. The number of clusters is modeled by a birth/death process of the cluster.

The GSCM is accurate and generates the CIR for different environments by using different parameter sets. However, the computational complexity is high since a large number of scatters are required to reproduce the contribution of diffuse components. Compared to GSCM, the proposed cluster based model considers only the significant MPCs and group the MPCs with the same properties, and thus yields a lower complexity. The assumed geometric information comes into play when we calculate the evolution of a cluster's delay and Doppler over different stationarity regions. Therefore, the proposed model is non-stationary and maintains a relatively low complexity.

6.5 Appendix: More Results

This appendix provides results of the cluster lifetime for highway scenario with LOS in Section 6.5.1. In Section 6.5.2, Fitting parameters for cluster spreads are collected for 12 different measurement runs in LOS obstruction scenario.

6.5.1 Cluster Lifetime for LOS Scenario

For the LOS scenario, there are 47 clusters detected over the total time interval. During the whole measurement, 2 or 3 coexisting clusters are more often detected, as shown in Fig. 6.15(a). Although less clusters are detected compared to the LOS obstruction scenario in Fig. 6.4, there are 13 clusters that remain for more than 15 stationarity regions in Fig. 6.15(b). Eliminating the longest and shortest lifetimes, the distribution of cluster lifetimes, shown in Fig. 6.15(c), also obeys a lognormal distribution with its mean $\mu = 2.04$ and standard deviation $\sigma = 1.05$.

The cluster centroids tracking for the LOS scenario is shown in Fig. 6.16. As for the LOS obstruction scenario, we select the clusters who exist more than 15 stationarity regions as well. Moreover, we can also observe three categories of clusters: (i) The cluster 1 is corresponding to the LOS component. Comparing the close-up 3-D view of the relevant clusters in Fig. 6.3 to Fig. 6.16, it can be seen that the contributed gain by cluster $C_{\mathrm{ID}} = 1$ in the LOS scenario is higher than the one in the LOS obstruction scenario. (ii) For the clusters $C_{\mathrm{ID}} \in \{2, 3, 9, 12, 13, 24, 32, 39, 42, 44, 46\}$, their Doppler shifts are around 0 Hz, which means that the clusters have the same speed as the RX vehicle or the direction of the propagation path is orthogonal to the driving direction of the TX and RX vehicles. Meanwhile, their delays are almost constant during their existing time, respectively. It indicates that the propagation path length stays the same for each cluster. Thus, we think these clusters come from the vehicles driving on the left lane in the same direction and the road signs where the RX passing by at $t = 8$s. (iii) For the cluster $C_{\mathrm{ID}} = 27$, its delays are approximately constant, while its Doppler shifts become larger during its lifetime. It mostly comes from a big moving vehicle driving on the left lane, whose speed is increasing.

6.5.2 Cluster Spreads for Obstructed LOS Scenario

We performed the same analysis as in Section 6.3.2 for the whole set of measurements. Tab. 6.4 presents 1) the mean value and the standard deviation for log-normal distribution, and 2) the parameters a and b for the linear regression line. These parameters are provided for delay and Doppler spreads for cluster 1 and the

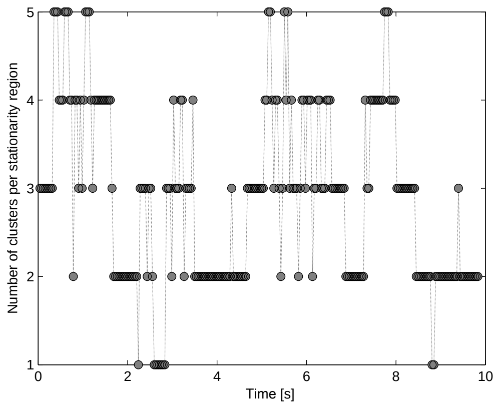

(a) Number of clusters

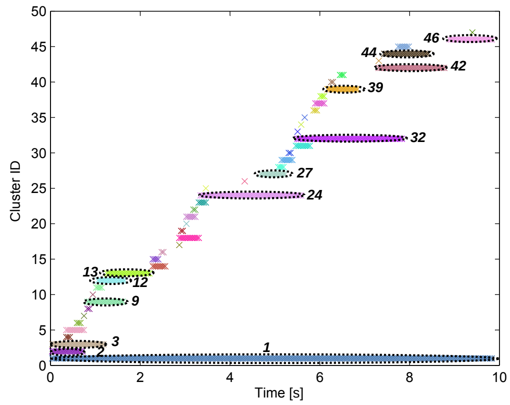

(b) Cluster lifetimes

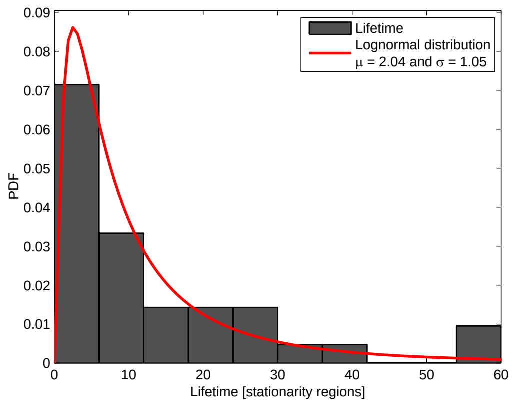

(c) Distribution

Figure 6.15: Number of clusters per stationarity region, cluster lifetimes and its lognormal distribution for the LOS scenario.

other clusters respectively. It is noteworthy that the relationship between delay and Doppler spreads vary significantly for different measurements. For measurements 5 and 9 where one strong LOS component exists, we may also have negative values for a occasionally, which suggests that the increase of the delay spread may result in a decrease of the Doppler spread.

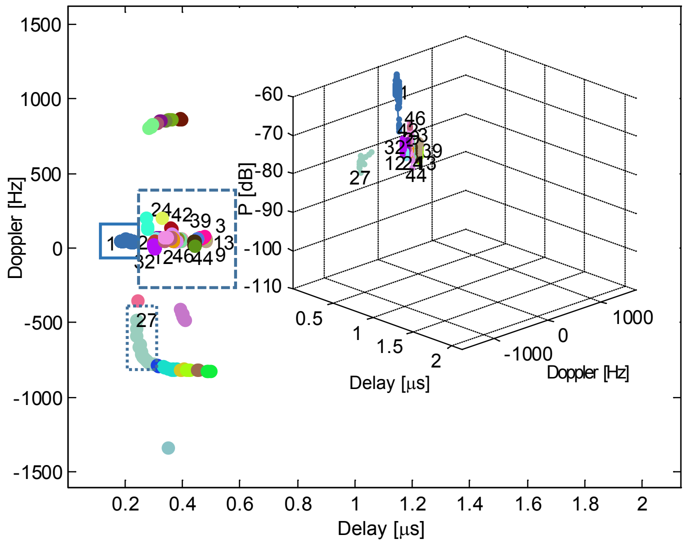

Figure 6.16: Cluster centroids tracking for the LOS obstruction scenario, where the clusters who exist more than 15 stationarity regions are marked. A 3-D view of the relevant clusters is also included.

Table 6.4: Fitting parameters for all 12 measurement runs

Parameters	Cluster 1						Other clusters					
	Delay		Doppler		Delay/Doppler		Delay		Doppler		Delay/Doppler	
	mean	std	mean	std	a	b	mean	std	mean	std	a	b
Meas1	-2.51	0.43	3.82	0.52	633.52	-4.00	-3.34	1.90	3.05	1.74	429	7.37
Meas2	-2.15	0.30	3.50	0.27	199.05	10.65	-3.32	1.78	3.05	0.70	132	16.2
Meas3	-2.42	0.46	3.66	0.83	1085.62	-47.17	-3.36	1.87	3.09	1.34	426	7.48
Meas4	-2.99	0.28	3.29	0.17	32.85	25.50	-3.78	2.07	2.94	0.73	231	12.6
Meas5	-2.78	0.22	3.25	0.14	-51.57	29.29	-4.09	2.34	2.90	0.36	649	1.4
Meas6	-3.19	0.16	3.06	0.08	143.91	15.42	-3.31	0.17	3.07	0.18	377	8.08
Meas7	-2.55	0.41	3.66	0.39	480.16	1.36	-3.64	1.94	2.82	2.16	712	1.78
Meas8	-2.71	0.32	3.41	0.30	299.74	10.93	-3.52	1.86	3.08	1.12	665	0.525
Meas9	-3.02	0.19	3.27	0.14	-19.40	27.45	-3.87	2.18	2.90	0.70	207	12.5
Meas10	-3.01	0.22	3.34	0.12	86.53	24.00	-2.93	0.86	3.30	0.98	192	19.2
Meas11	-3.10	0.17	3.33	0.13	34.28	26.64	-3.47	0.87	2.93	0.87	131	15.8
Meas12	-2.66	0.23	3.25	0.13	111.80	18.00	-3.36	1.67	3.04	0.24	80.9	17.8

7 Conclusions

7.1 Summary

In this thesis, we devised, assessed and analyzed interference management techniques for interference channels. We devised non-stationary vehicular channel modeling approaches and evaluated the communication performance.

In the first part of the thesis, we revisited the background and basics of interference alignment (IA) in K-user interference channels. We gave an overview of different interference management schemes for K-user interference channels.

Global channel state information (CSI) is required by IA to reduce the interference signal dimensions and thus achieve the optimal degrees of freedom (DoF). Hence, we proposed a channel estimation feedback and prediction framework for single-input single-output (SISO) IA in time-variant channels. The algorithm enables reduced-rank channel prediction and is efficient to choose the subspace dimension associated with a higher rate by trading off prediction error and quantization error. We have characterized the scaling of the required number of bits in order to decouple the rate loss due to channel quantization from the transmit power.

To relief the global CSI feedback burden, we investigated opportunistic interference alignment (OIA) algorithms, exploiting channel randomness and multiuser diversity by user selection. We proposed threshold-based feedback schemes for OIA algorithms, which reduce the amount of feedback. We investigated different choices of threshold, user scaling law and the achievability of DoF for real-valued feedback and 1-bit feedback, respectively. For OIA with real-valued feedback, we characterized the threshold and the corresponding feedback load to achieve the optimal DoF. For OIA with 1-bit feedback, we provided an optimal choice of the 1-bit quantizer to achieve the DoF $d = 1$. For DoF $d > 1$, we derived an asymptotic threshold choice by solving an upper bound for the rate loss.

In the second part of the thesis, we focused our attention on channel modeling and performance analysis for vehicular communications. We developed a geometry-based stochastic channel model (GSCM) for road intersections.

We evaluated the communication performance in terms of frame error rate (FER) at various transmitter (TX)/receiver (RX) locations and velocities with three different types of channel estimators. In order to overcome the low signal to noise ratio (SNR) due to non-line of sight (NLOS), we deployed a relay at the intersection to enhance the reliability of communications.

In order to reduce the complexity of the GSCM, we developed a cluster-based vehicular channel model with low computational complexity suitable for a real-time implementation. We presented a joint cluster identification-and-tracking approach based on the power spectral density in delay and Doppler. We characterized the cluster parameters, e.g. lifetime, delay and Doppler spreads based on vehicular channel measurements. We devised a simplified cluster-based vehicular channel model by dividing the cluster locations in the delay-Doppler plane into different characteristic regions.

7.2 Key Findings

In this section, I will list the main results of the thesis.

CSI Feedback for IA

We observed that the accuracy of CSI significantly influences the performance of interference management techniques. In time-variant channels, we showed that the channel evolution can be described by only a few subspace coefficients. For IA, we showed that the subspace coefficients can be quantized and fed back using vector quantization, which greatly reduces the redundancy of the codebook by exploiting the rotational invariance. We introduced a whitening process to match the second order statistics of the subspace vector to the quantization codebook. We derived an upper bound of the rate loss due to the channel prediction- and quantization-error. The upper bound is accurate and used to facilitate an adaptive subspace dimension switching algorithm. We demonstrated the tradeoff between quantization error and prediction error. This tradeoff can be efficiently captured by our proposed subspace dimension switching algorithm. Simulation results suggested that a higher subspace dimension is preferred for high SNR regime with an adequate number of feedback bits. By adaptively choosing the dimension, a rate gain over the non-predictive strategy can be obtained.

Threshold-Based CSI Feedback for OIA

Using threshold-based real-valued feedback, both theoretical analysis and simulation results showed that the amount of feedback can be dramatically reduced by more than one magnitude, while preserving the essential DoF promised by conventional OIA with full feedback.

To further answer to question of how to transfer the feedback information to the TXs, we considered finite-rate feedback and proved that 1-bit feedback per user is sufficient to achieve the optimal DoF if the one-bit quantizer is chosen judiciously. Importantly, the required user scaling law remains the same as for OIA with perfect real-valued feedback.

We found that the threshold that achieves the optimal DoF is not unique. We provided a generalized expression for the threshold achieving DoF d. We showed the equivalence between the asymptotic threshold and the optimal threshold for DoF $d = 1$. We showed that the threshold-based 1-bit feedback captures most of the capacity provided by a system with real-valued feedback.

We compared OIA and IA with the same amount of feedback and presented the comparison in terms of complexity and achievable rate. We found that OIA has a much simpler quantizer and provides a higher sum rate in the practical operation region of a cellular communication system. For instance, at 20dB SNR with 10 bits feedback per cell for both, OIA and IA, we demonstrated that OIA reduces the complexity by more than one order of magnitude while increasing the sum rate by a factor of 2. Therefore, we concluded that when there are adequate number of users in each cell, OIA provides a passive interference alignment capability with lower complexity for quantization.

Evaluation of Vehicular Communication Performance at Road Intersection Using a GSCM

We implemented a vehicular non-stationary channel model for road intersections using the concept of a GSCM. We parameterized and verified the proposed GSCM by comparing it with a measurement based path-loss model and real-world vehicle-to-vehicle (V2V) channel measurements. We showed link level simulation results for IEEE 802.11p at road intersections with varying TX/RX locations using different channel estimation techniques. We demonstrated that a relay at the intersection greatly extends the reliable communication region. Furthermore, we found that the velocity of the TX and the RX has a strong impact on the achieved FER if the block-type least square channel estimator is used. For velocities higher than 50 km/h, a block-comb-type estimator or an advanced iterative DPS channel estimator ensures a low FER and a large distance range in safety critical crossing scenarios.

Characterization of Time-Varying Cluster Parameters for the Vehicular Channel

We evaluated the time-varying cluster lifetime based on vehicular channel measurements. We found that the cluster corresponding to the line of sight (LOS) component stays throughout the entire measurement run and contributes the highest gain. Without considering the longest and shortest lifetimes, we found that the probability density of cluster lifetime obeys a lognormal distribution.

By analyzing the time-variant spreads of clusters, we found that the cluster associated with LOS component usually consists of multipath components (MPCs) coming from several different scatterers, thus resulting in more dynamically changing spreads. Other clusters, stemming from a single scatterer, stay more stable in the delay-Doppler domain.

For the purpose of low complexity emulation, we devised a simplified cluster-based vehicular channel model by dividing the cluster locations into different characteristic regions based on the relationship between delay and Doppler shift. The cluster parameters are randomly drawn from pre-computed distributions obtained from measurements. We validated our model with measurement data in terms of the RMS delay spread and Doppler spread. A close match between our numeric model and measurement results was demonstrated.

A Acronyms

AWGN	additive white Gaussian noise
CAM	cooperative awareness message
CDF	cumulative distribution function
CIR	channel impulse response
CSI	channel state information
CSIT	channel state information at the transmitter
DBSCAN	density-based spatial clustering of applications with noise
DF	decode-and-forward
DoF	degrees of freedom
DPS	discrete prolate spheroidal
FDD	frequency-division duplex
FDMA	frequency division multiple access
FER	frame error rate
GSCM	geometry-based stochastic channel model
IA	interference alignment
IoT	internet of things
LOS	line of sight
LSF	local scattering function
MC	Monte-Carlo

MCD multipath component distance

MIMO multiple-input multiple-output

ML maximum-likelihood

MMSE minimum mean square error

MPC multipath component

MRC maximum ratio combining

NLOS non-line of sight

OFDM orthogonal frequency division multiplexing

OIA opportunistic interference alignment

PDF probability density function

QPSK quadrature phase shift keying

RMS root mean square

RVQ random vector quantization

RX receiver

SIMO single-input multiple-output

SISO single-input single-output

SNR signal-to-noise ratio

TDD time-division duplex

TDMA time division multiple access

TX transmitter

V2I vehicle-to-infrastructure

V2V vehicle-to-vehicle

WSSUS wide sense stationary uncorrelated scattering

B Notation

The following notation is used throughout this dissertation:

Symbol	Description
a	scalar
$\|a\|$	magnitude of a scalar
$\mathbf{a}$	vector (lowercase boldface)
$\mathbf{A}$	matrix (uppercase boldface)
$\mathbf{I}_N$	$N \times N$ identity matrix
$\mathbf{0}_{\mathbf{M}\times\mathbf{N}}$	$M \times N$ all zero matrix
$\mathbb{E}[\cdot]$	expectation operator taken over the variable x
$(\cdot)^*$	complex conjugate operator
$(\cdot)^{\mathrm{T}}$	transpose operator
$(\cdot)^{\mathrm{H}}$	Hermitian transpose operator (transpose + complex conjugate)
$\mathrm{tr}(\cdot)$	trace of a matrix
$\det(\cdot)$	determinant of a matrix
$\lceil\cdot\rceil$	ceiling operation
$\\|\cdot\\|$	Euclidean norm
$\\|\cdot\\|_{\mathrm{F}}$	Frobenius norm
$\sim$	distributed as
$\mathbb{R}$	set of real numbers
$\mathbb{C}$	set of complex numbers
$\mathcal{N}(a, \sigma^2)$	Gaussian distribution of mean a and variance σ^2
$\mathcal{CN}(a, \sigma^2)$	complex Gaussian distribution of mean a and variance σ^2
$\Pr(A)$	probability of an event A
$[\mathbf{A}]_{(k:l,m:n)}$	a submatrix of $\mathbf{A}$ containing the elements of rows $k-l$ and columns $m-n$
$\mathrm{diag}(\mathbf{a})$	diagonal matrix with the main diagonal $\mathbf{a}$
$\mathrm{Re}(a)$	the real part of $a \in \mathbb{C}$
$\mathrm{null}(\mathbf{A})$	null space of $\mathbf{A}$
$\mathrm{span}(\mathbf{A})$	space spanned by the columns of $\mathbf{A}$

$\mathbf{D}_N$	$N \times N$ DFT matrix, where $[\mathbf{D}_N]_{i,j} = \frac{1}{\sqrt{N}} e^{-j2\pi(i-1)(j-1)/N}$, $\forall i, j \in \{1, \ldots, N\}$.
log	natural logarithm function
$\Gamma(\cdot)$	Gamma function
$\mathbf{A} \prec \mathbf{B}$	the column space of $\mathbf{A}$ is a subset of the column space of $\mathbf{B}$
$g(N) = O(f(N))$	$\lim_{N \to \infty} \lvert g(N)/f(N) \rvert$ is bounded
$g(N) = o(f(N))$	$\lim_{N \to \infty} \lvert g(N)/f(N) \rvert = 0$

Table B.1: Definition of the employed mathematical notation.

Bibliography

[1] Ericsson, “Ericsson traffic exploration tool,” 2016. [Online]. Available: https://www.ericsson.com/TET.

[2] ——, “Ericsson Mobility Report,” Tech. Rep. June, 2016. [Online]. Available: https://www.ericsson.com/res/docs/2016/ericsson-mobility-report-2016.pdf.

[3] J. Karedal, F. Tufvesson, N. Czink, A. Paier, C. Dumard, T. Zemen, C. F. Mecklenbräuker, and A. Molisch, “A geometry-based stochastic MIMO model for vehicle-to-vehicle communications,” *IEEE Trans. Wirel. Commun.*, vol. 8, no. 7, pp. 3646–3657, Jul. 2009.

[4] Wooseok Nam, Dongwoon Bai, Jungwon Lee, and Inyup Kang, “Advanced interference management for 5G cellular networks,” *IEEE Commun. Mag.*, vol. 52, no. 5, pp. 52–60, May 2014.

[5] H. Weingarten, Y. Steinberg, and S. Shamai, “The capacity region of the Gaussian multiple-input multiple-output broadcast channel,” *IEEE Trans. Inf. Theory*, vol. 52, no. 9, pp. 3936–3964, Sept. 2006.

[6] B. Suard, G. Xu, H. Liu, and T. Kailath, “Uplink channel capacity of space-division-multiple-access schemes,” *IEEE Trans. Inf. Theory*, vol. 44, no. 4, pp. 1468–1476, Jul. 1998.

[7] A. Carleial, “Interference channels,” *IEEE Trans. Inf. Theory*, vol. 24, no. 1, pp. 60–70, Jan. 1978.

[8] T. Han and K. Kobayashi, “A new achievable rate region for the interference channel,” *IEEE Trans. Inf. Theory*, vol. 27, no. 1, pp. 49–60, Jan. 1981.

[9] R. Etkin, D. Tse, and H. Wang, “Gaussian interference channel capacity to within one bit,” *IEEE Trans. Inf. Theory*, vol. 54, no. 12, pp. 5534–5562, Nov. 2008.

[10] M. H. M. Costa, “Writing on dirty paper,” *IEEE Trans. Inf. Theory*, vol. 29, no. 3, pp. 439–441, May 1983.

[11] V. Cadambe and S. Jafar, "Interference alignment and degrees of freedom of the K-user interference channel," *IEEE Trans. Inf. Theory*, vol. 54, no. 8, pp. 3425–3441, Aug. 2008.

[12] A. Høst-Madsen and A. Nosratinia, "The multiplexing gain of wireless networks," in *IEEE Int. Symp. Inf. Theory*, 2005, pp. 2065–2069.

[13] H. J. Yang, W.-y. Shin, B. C. Jung, and A. Paulraj, "Opportunistic interference alignment for MIMO interfering multiple-access channels," *IEEE Trans. Wirel. Commun.*, vol. 12, no. 5, pp. 2180–2192, May 2013.

[14] B. C. Jung, D. Park, and W. Shin, "Opportunistic interference mitigation achieves optimal degrees-of-freedom in wireless multi-cell uplink networks," *IEEE Trans. Commun.*, vol. 60, no. 7, pp. 1935–1944, Jul. 2012.

[15] T. Gou, T. Koike-Akino, and P. Orlik, "Improved and opportunistic interference alignment schemes for multi-cell interference channels," in *IEEE Veh. Technol. Conf.*, May 2012.

[16] J. H. Lee, W. Choi, and B. D. Rao, "Multiuser diversity in interfering broadcast channels: achievable degrees of freedom and user scaling law," *IEEE Trans. Wirel. Commun.*, vol. 12, no. 11, pp. 5837–5849, Nov. 2013.

[17] H. J. Yang, W.-y. Shin, B. C. Jung, C. Suh, and A. Paulraj, "Opportunistic downlink interference alignment," in *Proc. IEEE Int. Symp. Inf. Theory*, 2014, pp. 1588–1592.

[18] J. H. Lee and W. Choi, "On the achievable DoF and user scaling law of opportunistic interference alignment in 3-transmitter MIMO interference channels," *IEEE Trans. Wirel. Commun.*, vol. 12, no. 6, pp. 2743–2753, Jun. 2013.

[19] Andreas F. Molisch, *Wireless Communications*, 2nd ed. Wiley Publishing, 2011.

[20] G. Acosta-Marum and M. Ingram, "Six time- and frequency- selective empirical channel models for vehicular wireless LANs," *IEEE Veh. Technol. Mag.*, vol. 2, no. 4, pp. 4–11, Dec. 2007.

[21] P. Bello, "Characterization of randomly time-variant linear channels," *IEEE Trans. Commun.*, vol. 11, no. 4, pp. 360–393, Dec. 1963.

[22] "IEEE 802.11p: part 11: wireless LAN medium access control (MAC) and physical layer (PHY) specifications: amendment 6: wireless access in vehicular environments," Tech. Rep., 2010.

[23] L. Bernadó, "Non-stationarity in vehicular wireless channels," Ph.D. dissertation, 2012.

[24] N. Czink, X. Yin, H. OZcelik, M. Herdin, E. Bonek, and B. Fleury, "Cluster characteristics in a MIMO indoor propagation environment," *IEEE Trans. Wirel. Commun.*, vol. 6, no. 4, pp. 1465–1475, Apr. 2007.

[25] N. Czink, T. Zemen, J.-P. Nuutinen, J. Ylitalo, and E. Bonek, "A time-variant MIMO channel model directly parametrised from measurements," *EURASIP J. Wirel. Commun. Netw.*, no. 3, pp. 1–16, 2009.

[26] C. Chen and M. Jensen, "A stochastic model of the time-variant MIMO channel based on experimental observations," *IEEE Trans. Veh. Technol.*, vol. 58, no. 6, pp. 2618–2625, 2009.

[27] Y. Oda and T. Taga, "Clustering of local scattered multipath components in urban mobile environments," in *IEEE 55th Veh. Technol. Conf. VTC Spring*, vol. 1, 2002, pp. 11–15.

[28] L. Bernadó, A. Roma, N. Czink, A. Paier, and T. Zemen, "Cluster-based scatterer identification and characterization in vehicular channels," in *11th Eur. Wirel. Conf.*, 2011, pp. 168–173.

[29] Z. Xu and T. Zemen, "Grassmannian delay-tolerant limited feedback for interference alignment," in *Asilomar Conf. Signals, Syst. Comput.*, Nov. 2013, pp. 230–235.

[30] ——, "Time-variant channel prediction for interference alignment with limited feedback," in *2014 IEEE Int. Conf. Commun. Work.*, Jun. 2014, pp. 653–658.

[31] Z. Xu, L. Bernadó, M. Gan, M. Hofer, T. Abbas, V. Shivaldova, K. Mahler, D. Smely, and T. Zemen, "Relaying for IEEE 802.11p at road intersection using a vehicular non-stationary channel model," in *IEEE 6th Int. Symp. Wirel. Veh. Commun.*, no. 1, Sept. 2014.

[32] Z. Xu, M. Gan, and T. Zemen, "Threshold-based selective feedback for opportunistic interference alignment," in *IEEE Wirel. Commun. Netw. Conf.*, 2015, pp. 276–280.

[33] ——, "Opportunistic interference alignment with 1-bit feedback in 3-cell interference channels," in *IEEE 26th Annu. Int. Symp. Pers. Indoor, Mob. Radio Commun.*, Hongkong, China, Aug. 2015, pp. 143–147.

[34] Z. Xu, M. Gan, C. F. Mecklenbräuker, and T. Zemen, "Cluster spreads for time-variant vehicular channels," in *9th Eur. Conf. Antennas Propag.*, Lisbon, Portugal, 2015.

[35] M. Gan, Z. Xu, C. F. Mecklenbräuker, and T. Zemen, "Cluster lifetime characterization for vehicular communication channels," in *9th Eur. Conf. Antennas Propag.*, Lisbon, Portugal, 2015.

[36] Z. Xu, M. Gan, and T. Zemen, "Cluster-based non-stationary vehicular channel model," in *Eur. Conf. Antennas Propag.*, Davos, Switzerland, Apr. 2016.

[37] B. Nazer, M. Gastpar, S. A. Jafar, and S. Vishwanath, "Ergodic interference alignment," *IEEE Trans. Inf. Theory*, vol. 58, no. 10, pp. 6355–6371, Oct. 2012.

[38] J. Thukral and H. Bolcskei, "Interference alignment with limited feedback," in *IEEE Int. Symp. Inf. Theory*, Jun. 2009, pp. 1759–1763.

[39] B. Da and R. Zhang, "Exploiting interference alignment in multi-cell cooperative OFDMA resource allocation," *IEEE Glob. Telecommun. Conf.*, pp. 8–12, 2011.

[40] M. A. Maddah-Ali, A. S. Motahari, and A. K. Khandani, "Communication over MIMO X channels: Interference alignment, decomposition, and performance analysis," *IEEE Trans. Inf. Theory*, vol. 54, no. 8, pp. 3457–3470, 2008.

[41] K. Gomadam, V. R. Cadambe, and S. A. Jafar, "A distributed numerical approach to interference alignment and applications to wireless interference networks," *IEEE Trans. Inf. Theory*, vol. 57, no. 6, pp. 3309–3322, Jun. 2011.

[42] A. S. Motahari, S. Oveis-Gharan, M. A. Maddah-Ali, and A. K. Khandani, "Real interference alignment: Exploiting the potential of single antenna systems," *IEEE Trans. Inf. Theory*, vol. 60, no. 8, pp. 4799–4810, 2014.

[43] Sang Won Choi, S. Jafar, and Sae-Young Chung, "On the beamforming design for efficient interference alignment," *IEEE Commun. Lett.*, vol. 13, no. 11, pp. 847–849, Nov. 2009.

[44] D. Kim and M. Torlak, "Optimization of interference alignment beamforming vectors," *IEEE J. Sel. Areas Commun.*, vol. 28, no. 9, pp. 1425–1434, Dec. 2010.

[45] C. M. Yetis, T. Gou, S. A. Jafar, and A. H. Kayran, "On feasibility of interference alignment in MIMO interference networks," *IEEE Trans. Signal Process.*, vol. 58, no. 9, pp. 4771–4782, 2010.

[46] R. Tresch, M. Guillaud, and E. Riegler, "On the achievability of interference alignment in the K-user constant MIMO interference channel," in *IEEE/SP 15th Work. Stat. Signal Process.*, no. 1, Aug. 2009, pp. 277–280.

[47] S. W. Peters and R. W. Heath, "Cooperative Algorithms for {MIMO} Interference Channels," *IEEE Trans. Veh. Technol.*, vol. 60, no. 1, pp. 206–218, Jan 2011.

[48] Q. Shi, M. Razaviyayn, Z. Q. Luo, and C. He, "An iteratively weighted MMSE approach to distributed sum-utility maximization for a MIMO interfering broadcast channel," *IEEE Trans. Signal Process.*, vol. 59, no. 9, pp. 4331–4340, 2011.

[49] E. Telatar, "Capacity of multi-antenna Gaussian channels," *Eur. Trans. Telecommun.*, vol. 10, no. 6, pp. 585–595, 1999.

[50] D. Love, R. Heath, V. N. Lau, D. Gesbert, B. Rao, and M. Andrews, "An overview of limited feedback in wireless communication systems," *IEEE J. Sel. Areas Commun.*, vol. 26, no. 8, pp. 1341–1365, Oct. 2008.

[51] R. Tresch and M. Guillaud, "Cellular interference alignment with imperfect channel knowledge," in *IEEE Int. Conf. Commun. Work.*, Jun. 2009.

[52] B. Xie, Y. Li, H. Minn, and A. Nosratinia, "Adaptive interference alignment with CSI uncertainty," *IEEE Trans. Commun.*, vol. 61, no. 2, pp. 792–801, Feb. 2013.

[53] S. M. Razavi and T. Ratnarajah, "Performance analysis of interference alignment under CSI mismatch," *IEEE Trans. Veh. Technol.*, vol. 63, no. 9, pp. 4740–4748, Nov. 2014.

[54] P. Aquilina and T. Ratnarajah, "Performance Analysis of IA Techniques in the MIMO IBC With Imperfect CSI," *IEEE Trans. Commun.*, vol. 63, no. 4, pp. 1259–1270, Apr. 2015.

[55] R. Krishnamachari and M. Varanasi, "Interference alignment under limited feedback for MIMO interference channels," *IEEE Trans. Signal Process.*, vol. 61, no. 15, pp. 3908–3917, Jul. 2013.

[56] J.-s. Kim, S.-h. Moon, S.-R. Lee, and I. Lee, "A new channel quantization strategy for MIMO interference alignment with limited feedback," *IEEE Trans. Wirel. Commun.*, vol. 11, no. 1, pp. 358–366, Jan 2012.

[57] M. Rezaee and M. Guillaud, "Interference alignment with quantized Grassmannian feedback in the \$K\$-user constant MIMO interference channel," *IEEE Trans. Wirel. Commun.*, vol. 15, no. 2, pp. 1456–1468, Feb. 2016.

[58] O. El Ayach and R. W. Heath, "Grassmannian differential limited feedback for interference alignment," *IEEE Trans. Signal Process.*, vol. 60, no. 12, pp. 6481–6494, Dec. 2012.

[59] Z. Xu, M. Gan, and T. Zemen, "On the degrees of freedom for opportunistic interference alignment with 1-bit feedback: The 3 cell case." [Online]. Available: http://arxiv.org/abs/1501.04312.

[60] N. Jindal, "MIMO broadcast channels with finite-rate feedback," *IEEE Trans. Inf. Theory*, vol. 52, no. 11, pp. 5045–5060, Nov. 2006.

[61] O. E. Ayach and R. W. Heath, "Interference alignment with analog channel state feedback," *IEEE Trans. Wirel. Commun.*, vol. 11, no. 2, pp. 626–636, Feb. 2012.

[62] G. Caire, N. Jindal, M. Kobayashi, and N. Ravindran, "Multiuser MIMO achievable rates with downlink training and channel state feedback," *IEEE Trans. Inf. Theory*, vol. 56, no. 6, pp. 2845–2866, 2010.

[63] W. Santipach and M. L. Honig, "Optimization of training and feedback overhead for beamforming over block fading channels," *IEEE Trans. Inf. Theory*, vol. 56, no. 12, pp. 6103–6115, Dec. 2010.

[64] O. El Ayach, A. Lozano, and R. W. Heath, "On the overhead of interference alignment: training, feedback, and cooperation," *IEEE Trans. Wirel. Commun.*, vol. 11, no. 11, pp. 4192–4203, Nov. 2012.

[65] R. K. Mungara, G. George, and A. Lozano, "Overhead and spectral efficiency of pilot-Assisted interference alignment in time-selective fading channels," *IEEE Trans. Wirel. Commun.*, vol. 13, no. 9, pp. 4884–4895, Sept. 2014.

[66] T. Zemen, C. Mecklenbräuker, F. Kaltenberger, and B. Fleury, "Minimum-energy band-limited predictor with dynamic subspace selection for time-variant flat-fading channels," *IEEE Trans. Signal Process.*, vol. 55, no. 9, pp. 4534–4548, Sept. 2007.

[67] T. Zemen and A. F. Molisch, "Adaptive reduced-rank estimation of nonstationary time-variant channels using subspace selection," *IEEE Trans. Veh. Technol.*, vol. 61, no. 9, pp. 4042–4056, Nov. 2012.

[68] S. M. Kay, *Fundamentals of Statistical Signal Processing: Estimation Theory.* Prentice-Hall, Inc., 1993.

[69] F. Dietrich and W. Utschick, "Pilot-assisted channel estimation based on second-order statistics," *IEEE Trans. Signal Process.*, vol. 53, no. 3, pp. 1178–1193, Mar. 2005.

[70] L. Bernadó, T. Zemen, F. Tufvesson, A. F. Molisch, and C. F. Mecklenbräuker, "Delay and Doppler spreads of nonstationary vehicular channels for safety-relevant scenarios," *IEEE Trans. Veh. Technol.*, vol. 63, no. 1, pp. 82–93, Jan 2014.

[71] T. Zemen, L. Bernadó, N. Czink, and A. F. Molisch, "Iterative time-variant channel estimation for 802.11p using generalized discrete prolate spheroidal sequences," *IEEE Trans. Veh. Technol.*, vol. 61, no. 3, pp. 1222–1233, Mar. 2012.

[72] M. Hofer, Z. Xu, and T. Zemen, "On the Optimum Number of Hypotheses for Adaptive Reduced-Rank Subspace Selection," in *IEEE 82nd Veh. Technol. Conf.*, Boston, Sept. 2015.

[73] D. J. Thompson, "Spectrum estimation and harmonic analysis," *Proc. IEEE*, vol. 70, pp. 1055–1096, 1982.

[74] D. Slepian, "Prolate spheroidal wave functions, Fourier analysis, and uncertainty—{V}: the discrete case," *Bell Syst. Tech. J.*, vol. 57, no. 5, pp. 1371–1430, 1978.

[75] H. Minn and V. Bhargava, "An investigation into time-domain approach for OFDM channel estimation," *IEEE Trans. Broadcast.*, vol. 46, no. 4, pp. 240–248, Dec. 2000.

[76] F. Wan, W. P. Zhu, and M. N. S. Swamy, "Semi-blind most significant tap detection for sparse channel estimation of OFDM systems," *IEEE Trans. Circuits Syst. I-Regular Pap.*, vol. 57, no. 3, pp. 703–713, 2010.

[77] D. Schafhuber, G. Matz, and F. Hlawatsch, "Adaptive Wiener filters for time-varying channel estimation in wireless OFDM systems," in *IEEE Int. Conf. Acoust. Speech, Signal Process.*, vol. 4, 2003, pp. 688–691.

[78] D. Love, R. Heath, and T. Strohmer, "Grassmannian beamforming for multiple-input multiple-output wireless systems," *IEEE Trans. Inf. Theory*, vol. 49, no. 10, pp. 2735–2747, Oct. 2003.

[79] K. K. Mukkavilli, A. Sabharwal, E. Erkip, and B. Aazhang, "On beamforming with finite rate feedback in multiple-antenna systems," *IEEE Trans. Inf. Theory*, vol. 49, no. 10, pp. 2562–2579, 2003.

[80] W. Dai, Y. E. Liu, and B. Rider, "Quantization bounds on Grassmann manifolds and applications to MIMO communications," *IEEE Trans. Inf. Theory*, vol. 54, no. 3, pp. 1108–1123, Mar. 2008.

[81] C. Au-yeung and D. Love, "On the performance of random vector quantization limited feedback beamforming in a MISO system," *IEEE Trans. Wirel. Commun.*, vol. 6, no. 2, pp. 458–462, Feb. 2007.

[82] P. Xia and G. B. Giannakis, "Design and analysis of transmit-beamforming based on limited-rate feedback," *IEEE Trans. Signal Process.*, vol. 54, no. 5, pp. 1853–1863, May 2006.

[83] D. Love and R. Heath, "Limited feedback diversity techniques for correlated channels," *IEEE Trans. Veh. Technol.*, vol. 55, no. 2, pp. 718–722, Mar. 2006.

[84] V. Raghavan and V. V. Veeravalli, "Ensemble properties of RVQ-based limited-feedback beamforming codebooks," *IEEE Trans. Inf. Theory*, vol. 59, no. 12, pp. 8224–8249, Dec. 2013.

[85] Y. Fadlallah, K. Amis, A. Aïssa-El-Bey, and R. Pyndiah, "Interference alignment for a multi-user SISO interference channel," *EURASIP J. Wirel. Commun. Netw.*, vol. 2014, no. 1, p. 79, 2014.

[86] R. H. Clarke, "A statistical theory of mobile-radio reception," *Bell Syst. Tech. J.*, p. 957, 1968.

[87] 3rd Generation Partnership Project (3GPP), "Technical Specification Group Radio Access Network; Evolved Universal Terrestrial Radio Access (E-UTRA); Physical Channels and Modulation (Release 10)."

[88] M. Rezaee and M. Guillaud, "Limited feedback for interference alignment in the K-user MIMO Interference Channel," *IEEE Inf. Theory Work.*, pp. 667–671, Sept. 2012.

[89] Lizhong Zheng and D. Tse, "Communication on the Grassmann manifold: a geometric approach to the noncoherent multiple-antenna channel," *IEEE Trans. Inf. Theory*, vol. 48, no. 2, pp. 359–383, 2002.

[90] D. Love and R. Heath, "Limited feedback unitary precoding for spatial multiplexing systems," *IEEE Trans. Inf. Theory*, vol. 51, no. 8, pp. 2967–2976, Aug. 2005.

[91] D. Gesbert and M. Alouini, "How much feedback is multi-user diversity really worth?" in *Proc. IEEE Int. Conf. Commun.*, 2004, pp. 234–238.

[92] M. Sharif and B. Hassibi, "On the capacity of MIMO broadcast channels with partial side information," *IEEE Trans. Inf. Theory*, vol. 51, no. 2, pp. 506–522, Feb. 2005.

[93] S. Sanayei and A. Nosratinia, "Opportunistic downlink transmission with limited feedback," *IEEE Trans. Inf. Theory*, vol. 53, no. 11, pp. 4363–4372, Nov. 2007.

[94] R. M. Corless, G. H. Gonnet, D. E. G. Hare, D. J. Jeffrey, and D. E. Knuth, "On the LambertW function," *Adv. Comput. Math.*, vol. 5, no. 1, pp. 329–359, Dec. 1996.

[95] T. Tang and R. W. Heath, "Opportunistic feedback for downlink multiuser diversity," *IEEE Commun. Lett.*, vol. 9, no. 10, pp. 948–950, 2005.

[96] J. Leithon, C. Yuen, H. a. Suraweera, and H. Gao, "A new opportunistic interference alignment scheme and performance comparison of MIMO interference alignment with limited feedback," in *IEEE Globecom Work.*, Dec. 2012, pp. 1123–1127.

[97] G. H. Golub and C. F. V. Loan, *Matrix Computations*, 3rd ed. Baltimore: The John Hopkins University Press, 1996.

[98] K. Mahler, P. Paschalidis, M. Wisotzki, A. Kortke, and W. Keusgen, "Evaluation of Vehicular Communication Performance at Street Intersections," in *IEEE 80th Veh. Technol. Conf.* IEEE, Sept. 2014.

[99] T. Mangel, O. Klemp, and H. Hartenstein, "A validated 5.9 GHz non-line-of-sight path-loss and fading model for inter-vehicle communication," in *11th Int. Conf. ITS Telecommun.*, Aug. 2011, pp. 75–80.

[100] T. Abbas, A. Thiel, T. Zemen, C. F. Mecklenbräuker, and F. Tufvesson, "Validation of a non-line-of-sight path-loss model for V2V communications at street intersections," in *13th Int. Conf. ITS Telecommun.*, Nov. 2013, pp. 198–203.

[101] M. Schack, J. Nuckelt, R. Geise, L. Thiele, and T. Kurner, "Comparison of path loss measurements and predictions at urban crossroads for C2C communications," in *5th Eur. Conf. Antennas Propag.*, Rome, 2011, pp. 2896–2900.

[102] H. Schumacher, H. Tchouankem, J. Nuckelt, T. Kürner, T. Zinchenko, A. Leschke, and L. Wolf, "Vehicle-to-vehicle IEEE 802.11p performance measurements at urban intersections," in *IEEE Int. Conf. Commun.*, Jun. 2012, pp. 7131–7135.

[103] A. Paier, L. Bernadó, J. Karedal, O. Klemp, and A. Kwoczek, "Overview of vehicle-to-vehicle radio channel measurements for collision avoidance applications," in *IEEE 71st Veh. Technol. Conf.*, 2010.

[104] L. Bernadó, N. Czink, T. Zemen, and P. Belanovic, "Physical layer simulation results for IEEE 802.11p using vehicular non-stationary channel model," in *IEEE Int. Conf. Commun. Work.*, May 2010.

[105] J. van de Beek, O. Edfors, M. Sandell, S. Wilson, and P. Borjesson, "On channel estimation in OFDM systems," in *IEEE 45th Veh. Technol. Conf. Countdown to Wirel. Twenty-First Century*, vol. 2, no. 1, 1995, pp. 815–819.

[106] L. Bahl, J. Cocke, F. Jelinek, and J. Raviv, "Optimal decoding of linear codes for minimizing symbol error rate," *IEEE Trans. Inf. Theory*, vol. 20, no. 2, pp. 284–287, Mar. 1974.

[107] D. Brennan, "Linear diversity combining techniques," *Proc. IEEE*, vol. 91, no. 2, pp. 331–356, Feb. 2003.

[108] C. Grover, I. Knight, and F. Okoro, "Automated emergency brake systems: Technical requirements, costs and benefits," Tech. Rep., 2013.

[109] L. Bernadó, T. Zemen, F. Tufvesson, A. F. Molisch, and C. F. Mecklenbräuker, "The (in-) validity of the WSSUS assumption in vehicular radio channels," *IEEE Int. Symp. Pers. Indoor Mob. Radio Commun. PIMRC*, pp. 1757–1762, Sept. 2012.

[110] G. Matz, "On non-WSSUS wireless fading channels," *IEEE Trans. Wirel. Commun.*, vol. 4, no. 5, pp. 2465–2478, Sept. 2005.

[111] M. Ester, H.-p. Kriegel, X. Xu, and D. Miinchen, "A density-based algorithm for discovering clusters in large spatial databases with noise," 1996.

[112] N. Czink, "The random-cluster model - A stochastic MIMO channel model for broadband communication systems of the 3rd generation and beyond," Ph.D. dissertation, 2007.

[113] A. Thiel, O. Klemp, A. Paiera, L. Bernadó, J. Karedal, and A. Kwoczek, "In-situ vehicular antenna integration and design aspects for vehicle-to-vehicle communications," *Eur. Conf. Antennas Propag.*, Apr. 2010.